Visualization of Mechanisms of Antimicrobial Peptide Action on Live *E. coli* Cells

By

Heejun Choi

A dissertation submitted in partial fulfillment of

the requirements of the degree of

Doctor of Philosophy

(Chemistry)

At the

University of Wisconsin-Madison

2015

Date of Final Oral Examination: 8/26/2015

The dissertation is approved by the following members of the Final Oral Committee:

James C. Weisshaar, Professor, Chemistry

Samuel H. Gellman, Professor, Chemistry

Douglas B. Weibel, Professor, Biochemistry

M. Thomas Record, Professor, Biochemistry

Jade Wang, Professor, Microbiology

To my parents, my brother, and my dog Gomi

TABLE OF CONTENTS

Acknowledgements

Getting a Ph.D. is a journey through an endless tunnel. I was guided by many genuinely intelligent *and* nice people (a difficult combination!) to reach the end of this tunnel. Without them, I would have not survived in this bitter winter of Wisconsin and the field of science. This section is dedicated to acknowledge people who have been there for me during my endless journey to Ph.D.

First and foremost, I thank my family. My family has been always supportive of my decision to become a scientist. Without this encouragement and moral support, I would not be able to continue, especially with many storms that have passed by. I especially thank my father and mother, who has sacrificed all their lives to support me and my brother to succeed in the United States. I also want to thank my brother for always kind and quietly encouraging. My dog, Gomi, has always been my cheerleader. He always makes my day happy.

I would also like to thank former and current Weisshaar group members. I thank Dr. Kem Sochacki, Dr. Ben Bratton, and Dr. Izzy smith for the initial guide for my project. I am grateful to have Dr. Somenath Bakshi as my senior from whom I can always learn. Zhilin Yang and Sonisilpa Mohapatra have been my wonderful juniors and friends. Somehow I adopted Zhilin as my younger sister. I specially thank Sonisilpa for teaching me that taking a deep breath always helps. Those two made my two years of Madison more enjoyable. I would like to thank Meghan Turner, my brightest and only undergraduate student who survived from me! That is already a big accomplishment. I also would thank Mainak Mustafi for following my teaching. I also thank

past and current group members: Rangarajan N., Wenting Li, Anurag Agrawal, Nikolai Radzinski, Dr. Kenneth Barns, Trillian Gregg, and Dr. Renee Dalrymple.

My research involved many biological and physical techniques. I would not be able to finish all this work without the help of others. Current and past members of Gourse lab and Landick lab helped tremendously on biology. I would like to thank Tamas Gaal, Amy Banta, Patricia Sanchez Vazquez, Jared Winkelmen for helping me understand the molecular biological techniques. I would like to thank Weibel lab for helping me construct microfluidics. I especially would like to thank Dr. Piercen Oliver and John Crooks for helping with the initial design and construction. I would also like to thank Thiago Santos for helping me get KEIO collection strains whenever I need them. I would also like to thank Prof. Patricia Kiley and Prof. James Imlay for helping me understand the reactive oxygen species. It was a tremendous help to get opinions from the experts in the field. I was blessed to have collaborators such as Prof. Runhui Liu, Dr. Saswata Chakraborty, and Prof. Zvika Hayouka. I thank Grischa Chen for helping me with learning how to grow macrophages. I would like to thank CompHelp people, especially Kyle Beth, Kyle Kufalk, and William Sixel for helping me whenever I have computer disasters. I also like to thank Al Silver, Paul McGuire and Desiree Bates for helping me whenever CompHelp people are not available and letting me use the gpuff. I also thank Rob McClain for giving me electronics help and thank Kendall Schneider for machine shop help. I thank Sue Martin-Zernicke, Kristi Hemmings, April Leslie, and Kat Myhre for making our lives easier.

Without supports from my friends, I would not believe I could continue my research in the United States. I would especially like to thank Dr. Erin Rockwell, Dr. Caitlin Cossaboom, Dr. Kelsey Altholz-LaVigne, Peter LaVigne, Dr. Katie Dowdy, and Michael Dutzer. They are there for me when I was having difficult time. They are amazing to be around. Yusuke Okuno has

been a supportive friend who taught me what dedication and kindness without expression mean. Angela Varela always brightened my day. I could endure the pain of writing thesis thanks to Gary Riggins and Andrea Attenberger.

I also need to thank many TV shows and movies that helped me get through many nights of Wisconsin, which include Futurama, Game of Thrones, Doctor Who, and many others. I should especially thank amazing drinks that made my night through writing this thesis less painful.

I was blessed with my thesis committee Prof. Samuel Gellman, Prof. Thomas Record, Prof. Douglas Weibel, Prof. Jade Wang. Unlike many people in chemistry department, I have interacted with and collaborated with each of them. They are very inspiring scientists. I thank especially for coming together on short notice and review my thesis work.

Lastly, I am eternally grateful to my advisor, Prof. James Weisshaar. Without his encouragement and support, I would not be able to explore many new ideas and learned many new techniques. His patience allowed me to “explode” in many directions, but it was a great experience for me to come up with many crazy ideas and test their feasibility.

If you are not acknowledged in this page, please contact me.

Abstract

Antimicrobial peptides are a part of the innate defense system that provides first line of defense against pathogens. They are generally short in length (15-50 aa) and are composed of cationic and hydrophobic residues. My thesis primarily focuses on understanding the mechanisms of antimicrobial peptide action on live *E. coli* cells using single-cell, time-lapse microscopy with high spatiotemporal resolution. We found that CM15, Melittin, and LL-37 showed increased antimicrobial activities toward *E. coli* cells growing aerobically as compared to anaerobically growing *E. coli*. I have developed single-cell, real-time reactive oxygen species (ROS) assays using a combination of CellROX green (monitors O_2^- and ·OH) and APEX2/Amplex red (H_2O_2). We observed that the accumulation of antimicrobial peptides in the periplasm cause the formation of ROS. We also investigated the effects of the growth medium on antimicrobial nylon-3 copolymer activity using minimum inhibitory concentration (MIC) assays. Finally, we found dual mechanisms by which an antimicrobial random nylon-3 copolymer inhibits the growth of *E. coli* cells. At lower concentration, osmotic shock dictates the growth inhibition. At higher concentration, oxidative stress dominates.

Chapter 1

Introduction to Antimicrobial Peptides

Introduction

Eukaryotic organisms are constantly challenged by the invasion of microorganisms. Throughout many generations of evolutionary selection, host organisms have developed multiple ways to clear pathogens from their system. The increased defense against microorganisms also exerted selection pressure to develop resistance to the host defense system. Until the discovery of penicillin in 1920s, infections caused by pathogens were one of the leading causes of death.[1] The further development and improvement of antibiotics in the past century saved millions of lives, seemingly ending the war between the host and pathogens. Unfortunately, the overuse of antibiotics led to the development of superbugs that are resistant to most commercially available antibiotics.[2] These organisms are commonly called as ESKAPE pathogens, which stand for *Enterococcus faecium, Staphylococcus aureus, Klebsiella pneumoniae, Acinetobacter baumannii, Pseudomonas aeruginosa,* and *Enterobacter* species.[3]

With the emergence of these superbugs, new classes of antibiotics to which ESKAPE organisms have not yet developed resistance are in dire need. Most commercially available antibiotics such as penicillin or vancomycin are derivatives of natural products, usually non-ribosomally synthesized as secondary metabolites.[4] They are generally allosteric inhibitors that specifically inhibit functions of essential proteins, ultimately causing cell death. However, in order to decelerate the development of resistance, these allosteric drugs need to target a new class of proteins. The search process for inhibitors is time-consuming and costly.[5] Fortunately, we may be able to learn from the evolutionary battle between host and pathogens. Out of many strategies that the host uses for its defense against microoganisms, my thesis will focus on the action of antimicrobial peptides on live *Escherichia coli* cells.

Antimicrobial peptides (AMPs) are ribosomally synthesized peptides with relatively small size (~12-50 AA).[6] AMPs are an ancient element of the immune system and are ubiquitous in nature, ranging in their existence from plants to insects to mammals.[7] They are a part of the innate immune system, participating in the first line of defense against pathogens.[8] These peptides have a broad spectrum of activity against gram positive and negative bacteria, including drug resistant bacteria. The existence of AMPs was postulated in the late 19th century based on bacterial cell death after phagocytosis. The lack of adequate methods to isolate and characterize these peptides delayed their discovery until the late 1970s.[9] Their development can lead to a new class of antibiotics of potential therapeutic use.

Despite their potential as a new class of antibiotics, there is poor understanding of the mechanism of AMP actions on live cells, which has slowed the development of AMPs into clinically useful drugs.[10] Certain peptide-based antibiotics, however, are in the clinical trial stage for oral candidiasis (PAC-113, Pacgen Biopharmaceutical), catheter-associated infection (Omiganan, Micrologix Biotech), and implant surface disinfectants (hLF1-11, AM-Pharma).[11] In spite of their usefulness, these are very costly in part due to challenges in the synthesis and purification of these peptides. This challenge is complicated by the fact that there are no structure-function relationship studies that could lead to a rational design of these drugs rather than screening through expensive trial-and-error approaches. If rational design principles for effective peptide-based antibiotics did exist, chemical biologists could expand the functionality and stability by modifying the peptide, leading to cost-effective peptide-like antibiotics.

In the following section, our current understanding of antimicrobial peptides from both *in vitro* and *in vivo* studies is briefly summarized.

Structure and Membrane Permeabilization through In Vitro Experiments

The structural studies of AMPs are performed through x-ray crystallography, NMR spectroscopy, Fourier transform IR (FT-IR) spectroscopy, Raman spectroscopy, fluorescence spectroscopy, and circular dichroism (CD).[12] AMPs are categorized into five different classes: 1) Anionic peptides, 2) Linear, cationic α-helical peptides, 3) Cationic peptides enriched for specific amino acids, 4) Anionic and cationic peptides that contain cysteine and form disulfide bonds, and 5) Anionic and cationic peptide fragments of larger proteins. Most antimicrobial peptides with no disulfide bond linkage exhibit a disordered structure in pure water. However, these peptides adopt a helical structure in high salt, such as 15 mM bicarbonate, trifluoroacetate (TFA), or sulfate[13] or upon binding to the membrane[12], observed by NMR spectroscopy and circular dichroism on micelles.

A majority of *in vitro* studies, however, has focused on the interaction of AMPs with artificial membranes, such as unilamellar vesicles or supported lipid bilayers. This arose from early observations of cell lysis upon the treatment of AMPs, suggesting their membrane activity. The activity on artificial membranes was visualized through oriented circular dichroism, neutron diffraction, x-ray diffraction, and/or fluorescent dye leakage from vesicles.[12] From these studies, several membrane permeabilization mechanisms were suggested, mainly divided into two categories: pore formation and detergent-like permeabilization (**Figure 1**).

Pore formation has been directly observed for several AMPs. There are two categories of pores: 1) Barrel-stave pores and 2) Toroidal pores (**Figure 1**). The barrel-stave pore is similar to a protein ion channel, where antimicrobial peptides are laterally arranged as staves that form a barrel,[14] enclosing a water-filled channel across the membrane. The lipid head and tail arrangement was unperturbed upon the formation of the barrel-stave pore. This is a special case,

as the only known example of an AMP that forms barrel-stave pore is alamethicin.[15] It creates a small channel with inner and outer diameter of ~1.8 nm and ~4.0 nm, respectively.[16]

Toroidal pores, on the other hand, are more common among AMPs, including magainin[17], protegrin[18], and melittin[14]. Here, AMPs cooperatively induce changes in the local curvature of the membrane, forming a peptide-lipid toroid (**Figure 1.1**). This causes the formation of a pore-like structure, letting ions and small molecules pass through the channel.

In contrast, detergent-like permeabilization was inferred from the vesicle leakage behavior of several AMPs.[12] Wimley and coworkers suggested that there is little to no evidence for pore formation, especially on live cells.[10] Hence, several groups propose that AMPs destabilizes the membrane through several mechanisms that resemble detergent-like permeabilization. Epand and coworkers have proposed a *lipid clustering model,* where AMPs cluster the lipids. This leads to a formation of "defects" on the membrane, allowing the leakage of contents.[19] On the other hand, Wimley and coworkers suggest an *interfacial activity model* in which an imperfectly amphipathic peptide inserts into the bilayer interface, driving the rearrangement of lipids. These defects could lead to the observed leakage of contents by many AMPs.[20]

However, membrane permeabilization alone may not be the key to bacteriostatic and/or bactericidal activity of AMPs on live cells. The studies from Wimley group recently demonstrated that there was no correlation between the peptides that readily permeabilizes unilamellar vesicles and those that are killing the bacteria.[21] This suggests that the actual bacteriostatic and/or bactericidal activity from AMP treatment may not result solely from membrane permeabilization.

Bulk In Vivo Experiments Suggest More Than Permeabilization

There is a growing suspicion that growth halting occurs long before the leakage of content and total lysis of cells.[22] In combination with lack of correlation between peptide permeabilization of lipid vesicles and antimicrobial activity on live cells, membrane permeabilization as a main mechanism of action poses a question. What is, then, the main mechanism of cell death from AMP treatment? In 2002, Brodgen wrote a review article suggesting that AMPs are more than pore formers. For example, autolysins and phospholipases can be activated by antimicrobial peptide Pep5.[23] Buforin II exhibits antimicrobial activity with no membrane permeabilization.[24] Short, proline-rich AMPs exhibit different effects, such as inhibiting chaperone proteins such as DnaK[25] or GroEL[26]. Indolicidin, a bovine proline-rich AMP, showed complete inhibition of DNA and RNA synthesis in *E. coli*.[27] Gramicidin S, a cyclic antimicrobial peptide produced by *Bacillus brevis,* is shown to inhibit cytochrome oxidase *bd* complex.[28] Much evidence suggests that AMPs are multifaceted antibiotics.

Many environmental factors are also shown to modulate the antimicrobial efficacy of AMPs. The most recent studies on hBD-1 showed that reducing conditions that cause breakage of disulfide bond in hBD-1 increases the antimicrobial potency.[29] Another studies on LL-37 that is expressed in the *E. coli* cytoplasm showed that LL-37 activity is significantly reduced in anaerobic conditions, possibly due to formation of reactive oxygen species.[30] These environmental factors may be used in host organisms to retain population of gut microbiota while suppressing population of opportunistic pathogens that are exposed to different environment than their own niche.

Advantage of Single-cell Time-lapse Microscopy Experiments

Although bulk *in vivo* provides great insight into the machinery involved in cell death by AMPs, these assays have low spatial and time resolution. Some α-helical peptides kill bacteria so quickly that it is challenging to visualize the symptoms and behavior of live cells under the peptide treatment using conventional methods.[31] The usual *in vivo* experiments focused on bulk assays with fluorogenic dyes that can monitor membrane permeabilization, potassium leakage, and dissipation of the proton motive force (pmf). When the assays are performed, the general assumption is that observed phenomena are homogenously distributed among the population. However, spatiotemporal inhomogeneity in cell cultures is highly likely especially for the multifaceted actions of AMPs. Thus, bulk assays will significantly blur the mechanistic insight of how AMPs work on live cells. For example, in the previous studies using single-cell time-lapse microscopy, LL-37 is shown to preferentially permeabilize cells undergoing septation.[32] Visualization of such a process is not possible using conventional bulk assays or even through flow cytometry. Because direct observation of the population distribution is possible, single-cell, time-lapse microscopy provides detailed mechanistic insights of AMP action on live cells that cannot be achieved through conventional bulk assays.

Here, my dissertation primarily focused on understanding the mechanisms of antimicrobial peptide action on live *E. coli* cells using single-cell, time-lapse microscopy with high spatiotemporal resolution. Chapter 2 is designed to guide readers who are not familiar with the electron transport chain and reactive oxygen species (ROS) formation in *E. coli* to fully appreciate Chapter 3 and 4. Chapter 3 focuses on how antimicrobial peptide CM15 causes ROS formation in live *E. coli* cells. Chapter 4 expands Chapter 3 work to other natural antimicrobial peptides, including LL-37, Melittin, and Indolicidin. Chapter 5 explains in detail how structure-

function relationships can be affected by the selection of the growth medium. Finally, Chapter 6 describes how a particular antimicrobial nylon-3 random copolymer attacks *E. coli* cells via multiple pathways.

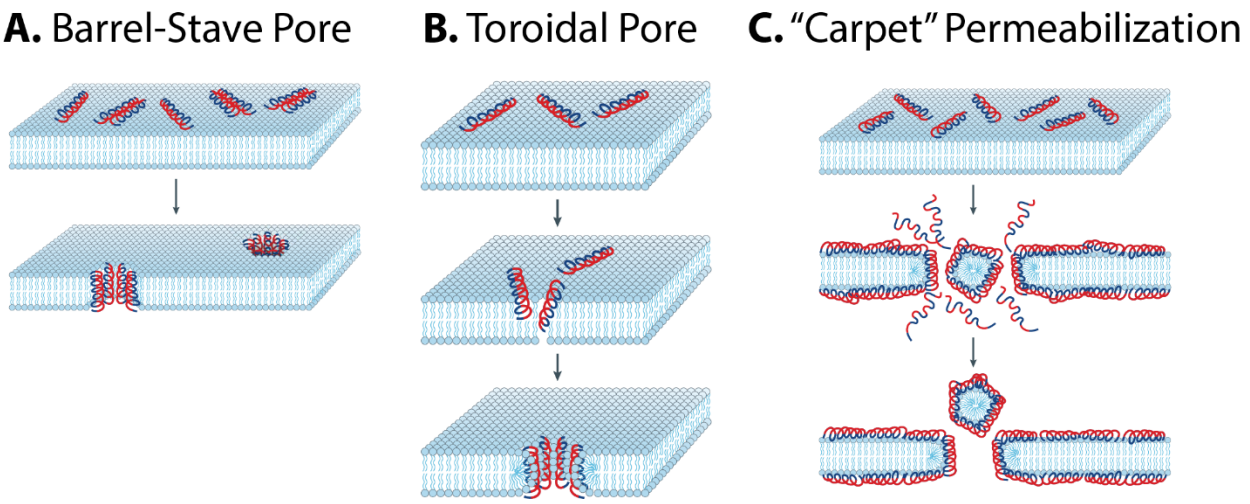

Figure 1.1 Three hypothesized mechanism of antimicrobial peptide permeablizing membrane: **A)** Barrel-Stave pore model **B)** Toroidal pore model **C**) "Carpet" permeabilization model. Blue-red helices represent amphipathic antimicrobial peptides. This figure is modified from Brogden's review.[12]

References

1. Blair, J. M. A.; Webber, M. A.; Baylay, A. J.; Ogbolu, D. O.; Piddock, L. J. V., Molecular mechanisms of antibiotic resistance. *Nat. Rev. Microbiol.* **2015,** *13* (1), 42-51.

2. Davies, J.; Davies, D., Origins and Evolution of Antibiotic Resistance. *Microbiology and Molecular Biology Reviews* **2010,** *74* (3), 417-+.

3. Boucher, H. W.; Talbot, G. H.; Bradley, J. S.; Edwards, J. E., Jr.; Gilbert, D.; Rice, L. B.; Scheld, M.; Spellberg, B.; Bartlett, J., Bad Bugs, No Drugs: No ESKAPE! An Update from the Infectious Diseases Society of America. *Clinical Infectious Diseases* **2009,** *48* (1), 1-12.

4. Sieber, S. A.; Marahiel, M. A., Learning from nature's drug factories: Nonribosomal synthesis of macrocyclic peptides. *J. Bacteriol.* **2003,** *185* (24), 7036-7043.

5. Hamad, B., THE ANTIBIOTIC MARKET MARKET INDICATORS. *Nat. Rev. Drug Discov.* **2010,** *9* (9), 676-676.

6. Zasloff, M., Antimicrobial peptides of multicellular organisms. *Nature* **2002,** *415* (6870), 389-395.

7. Tossi, A.; Sandri, L.; Giangaspero, A., Amphipathic, alpha-helical antimicrobial peptides. *Biopolymers* **2000,** *55* (1), 4-30.

8. Ganz, T., The role of antimicrobial peptides in innate immunity. *Integrative and Comparative Biology* **2003,** *43* (2), 300-304.

9. Sarmasik, A., Antimicrobial peptides: A potential therapeutic alternative for the treatment of fish diseases. *Turkish Journal of Biology* **2002,** *26* (4), 201-207.

10. Wimley, W. C.; Hristova, K., Antimicrobial peptides: successes, challenges and unanswered questions. *J Membr Biol* **2011,** *239* (1-2), 27-34.

11. Fjell, C. D.; Hiss, J. A.; Hancock, R. E. W.; Schneider, G., Designing antimicrobial peptides: form follows function (vol 11, pg 37, 2012). *Nat. Rev. Drug Discov.* **2012,** *11* (2), 124-124.

12. Brogden, K. A., Antimicrobial peptides: pore formers or metabolic inhibitors in bacteria? *Nat Rev Micro* **2005,** *3* (3), 238-250.

13. Johansson, J.; Gudmundsson, G. H.; Rottenberg, M. E.; Berndt, K. D.; Agerberth, B., Conformation-dependent Antibacterial Activity of the Naturally Occurring Human Peptide LL-37. *J. Biol. Chem.* **1998,** *273* (6), 3718-3724.

14. Yang, L.; Harroun, T. A.; Weiss, T. M.; Ding, L.; Huang, H. W., Barrel-stave model or toroidal model? A case study on melittin pores. *Biophys. J.* **2001,** *81* (3), 1475-1485.

15. Spaar, A.; Munster, C.; Salditt, T., Conformation of peptides in lipid membranes studied by X-ray grazing incidence scattering. *Biophys. J.* **2004,** *87* (1), 396-407.

16. He, K.; Ludtke, S. J.; Worcester, D. L.; Huang, H. W., Neutron scattering in the plane of membranes: structure of alamethicin pores. *Biophys J* **1996,** *70* (6), 2659-66.

17. Matsuzaki, K.; Sugishita, K.; Ishibe, N.; Ueha, M.; Nakata, S.; Miyajima, K.; Epand, R. M., Relationship of membrane curvature to the formation of pores by magainin 2. *Biochem.* **1998,** *34*, 11856-11863.

18. Lazaridis, T.; He, Y.; Prieto, L., Membrane Interactions and Pore Formation by the Antimicrobial Peptide Protegrin. *Biophys. J.* **2013,** *104* (3), 633-642.

19. Epand, R. M.; Epand, R. F., Lipid domains in bacterial membranes and the action of antimicrobial agents. *Biochim Biophys Acta* **2009,** *1788* (1), 289-94.

20. Wimley, W. C., Describing the mechanism of antimicrobial peptide action with the interfacial activity model. *ACS Chem Biol* **2010,** *5* (10), 905-17.

21. He, J.; Krauson, A. J.; Wimley, W. C., Toward the De Novo Design of Antimicrobial Peptides: Lack of Correlation Between Peptide Permeabilization of Lipid Vesicles and Antimicrobial, Cytolytic, or Cytotoxic Activity in Living Cells. *Biopolymers* **2014,** *102* (1), 1-6.

22. Brogden, K. A., Antimicrobial peptides: pore formers or metabolic inhibitors in bacteria? *Nat Rev Microbiol* **2005,** *3* (3), 238-50.

23. Bierbaum, G.; Sahl, H. G., Autolytic System of Staphylococcus-Simulans-22 - Influence of Cationic Peptides on Activity of N-Acetylmuramoyl-L-Alanine Amidase. *J. Bacteriol.* **1987,** *169* (12), 5452-5458.

24. Park, C. B.; Yi, K. S.; Matsuzaki, K.; Kim, M. S.; Kim, S. C., Structure-activity analysis of buforin II, a histone H2A-derived antimicrobial peptide: The proline hinge is responsible for the cell-penetrating ability of buforin II. *Proceedings of the National Academy of Sciences of the United States of America* **2000,** *97* (15), 8245-8250.

25. Kragol, G.; Lovas, S.; Varadi, G.; Condie, B. A.; Hoffmann, R.; Otvos, L., The antibacterial peptide pyrrhocoricin inhibits the ATPase actions of DnaK and prevents chaperone-assisted protein folding. *Biochemistry* **2001,** *40* (10), 3016-3026.

26. Otvos, L., Jr.; O, I.; Rogers, M. E.; Consolvo, P. J.; Condie, B. A.; Lovas, S.; Bulet, P.; Blaszczyk-Thurin, M., Interaction between heat shock proteins and antimicrobial peptides. *Biochemistry* **2000,** *39* (46), 14150-14159.

27. Subbalakshmi, C.; Sitaram, N., Mechanism of antimicrobial action of indolicidin. *Fems Microbiology Letters* **1998,** *160* (1), 91-96.

28. Mogi, T.; Ui, H.; Shiomi, K.; Omura, S.; Kita, K., Gramicidin S identified as a potent inhibitor for cytochrome bd-type quinol oxidase. *FEBS Lett.* **2008,** *582* (15), 2299-2302.

29. Schroeder, B. O.; Wu, Z. H.; Nuding, S.; Groscurth, S.; Marcinowski, M.; Beisner, J.; Buchner, J.; Schaller, M.; Stange, E. F.; Wehkamp, J., Reduction of disulphide bonds unmasks potent antimicrobial activity of human beta-defensin 1. *Nature* **2011,** *469* (7330), 419-+.

30. Liu, W.; Dong, S. L.; Xu, F.; Wang, X. Q.; Withers, T. R.; Yu, H. D.; Wang, X., Effect of intracellular expression of antimicrobial peptide LL-37 on growth of escherichia coli strain TOP10 under aerobic and anaerobic conditions. *Antimicrob Agents Chemother* **2013,** *57* (10), 4707-16.

31. Boman, H. G., Peptide antibiotics and their role in innate immunity. In *Annual Review of Immunology*, Paul, W. E., Ed. 1995; Vol. 13, pp 61-92.

32. Sochacki, K. A.; Barns, K. J.; Bucki, R.; Weisshaar, J. C., Real-time attack on single Escherichia coli cells by the human antimicrobial peptide LL-37. *Proceedings of the National Academy of Sciences of the United States of America* **2011,** *108* (16), E77-E81.

Chapter 2

Introduction to Reactive Oxygen Species and Aerobic Respiration

To guide the readers through Chapter 3 and 4, this section provides in-depth background on oxidative stress and cellular respiration. Aerobic organisms thrive in the oxygen-rich environment by effectively incorporating oxygen as a means to produce a proton gradient across the cytoplasmic membrane. ATP synthase then utilizes this proton gradient to produce ATP. These organisms, however, are in constant challenges from oxidative damage imposed by reactive oxygen species (ROS). In prokaryotes, one possible source of ROS is the electron transport chain. ROS can be produced upon accidental reduction of molecular oxygen by redox molecules, such as FADH2, inside the cell (**Figure 2.1**). The proteins involved in the electron transport chain in *E. coli* are briefly summarized below.

E. coli Electron Transport Chain (ETC)

Two major complexes are involved in the electron transport chain of *E coli*: primary dehydrogenases and terminal oxidoreductases (**Figure 2.2**).[1] The dehydrogenases act as functional quinone reductases while the terminal oxidoreductases act as functional quinone oxidases.[2] Unlike mitochondria, enteric bacteria such as *E. coli* do not have cytochrome c to carry out the electron transfer reaction. Quinones link the dehydrogenases and terminal reductases in electron transfer reactions. In *E. coli*, there are three different kinds of quinones: ubiquinone (UQ), menaquinone (MK), and demethylmenaquinoen (DMK).[2]

E. coli can generate a proton gradient through anaerobic and aerobic oxidative phosphorylation by utilizing various substances. This is possible because *E. coli* has 15 primary dehydrogenases and 14 terminal oxidoreductases with 8 different electron acceptors (O_2, nitrate, nitrite, fumarate, TMAO, DMSO, tetrathionate, and thiosulfate).[2] Use of diverse substrates for energy production allow *E. coli* to adapt in many different environments, including the human gut. In this chapter, the focus will be on proteins involved in aerobic growth of *E. coli*.

Two Major Primary Dehydrogenases under Aerobic Growth

During aerobic growth, *E. coli* utilizes NDH-1 and 2 complexes as the major primary dehydrogenases.[2] The NDH-2 complex is predominant in aerobic conditions. Both complexes utilize NADH as a substrate to carry out the first step of redox reactions in the electron transport chain. There are several differences in these two complexes as discussed below.

The NDH-1 complex is encoded by the gene *nuoA-N*. NDH-1 has the molecular weight of 534.4 kDa (Figure 2).[3] This multi-subunit protein spans the inner membrane. It is homologous to the proton pumping NADH dehydrogenase I (commonly known as Complex I) in mitochondria.[4] NDH-1 is essential for fumarate and DMSO respiration and it can function under both aerobic and anaerobic conditions.[5] NDH-1 contains FMN cofactor and forms ligands for nine Fe-S clusters that shuttle electrons from reduced flavin cofactors to the quinone binding site near the membrane interface.[3] These clusters are linearly arranged such that the distance between each cluster is less than 14 Å to reduce the possibility for electrons to escape.[3] The electrons on Fe-S clusters are finally delivered to ubiquinone or menaquinone. NDH-I is a proton pump that pumps out 4 H^+/NADH to the periplasm.

In contrast to the multi-subunit protein NDH-1, the NDH-2 complex is encoded from a single gene *ndh* and the protein has the molecular weight of 45 kDa.[3] This complex is used preferentially in aerobic and nitrate respiration.[5] Unlike NDH-1, NDH-2 is not used in anaerobic condition.[5] It does not contain iron-sulfur clusters but utilizes FAD.[3] NDH-2 is associated with the inner membrane, but the method of association to the membrane is unknown.[3] The reduced FADH2 directly reduces either ubiquinone or menaquinone.[6] The NDH-2 complex does not generate a proton gradient; it only serves as an electron carrier in the electron transport chain.[3]

Major Terminal Oxidoreductases in Aerobic Growth:

Once quinone is reduced to quinol by primary dehydrogenases, the electrons are carried to terminal oxidoreductases. Two major terminal oxidoreductases are used in aerobic conditions: quinol oxidases CyoABCD and CydAB. Both terminal reductases span the inner membrane of *E. coli.* A brief summary of these complexes is provided.

CyoABCD, commonly known as the cytochrome-*bo*3 complex, is a member of the heme copper oxidase family that couples the redox reaction to proton pumping, resulting in $4H^+/2e^-$.[7] This complex solely interacts with ubiquinol to accept electrons.[8] It is highly expressed in aerobic conditions and is transcriptionally regulated by ArcA and FNR. CyoAB contains redox groups including heme *b*, heme *o3*, and Cu, which are required for electron transfer, reduction of molecular oxygen, and proton pumping.[7] This complex has relatively low affinity for O_2 with K_D $\geq$0.3 mM.[9] This complex is also sensitive to cyanide and azide, which interact with the heme iron to inhibit the electron transfer reactions.[10]

CydAB, commonly known as the cytochrome *bd-I* complex, is heavily expressed at low O_2 concentration and has high affinity for O_2, with K_D = 0.28 μM.[11] This complex contains only three hemes (heme b_{595}, heme b_{558}, and heme *d*) and no copper.[7] Unlike cytochrome *bo3* complex, the *bd* complex does not act as a proton pump, but produces $2H^+$ at the periplasmic face of the membrane when quinol oxidizes on the surface of the protein.[7] CydAB can utilize both menaquinol and ubiquinol,[12] serve as an oxygen scavenger, and inhibit the degradation of oxygen sensitive enzymes present under anaerobic and microaerobic conditions.[13] The expression of *cydAB* increases under some unfavorable conditions, such as alkaline pH,[14] high temperature,[15] the presence of protonophores,[14] and low concentration of cyanide.[6] Certain deletion or defect mutants are sensitive to H_2O_2 and unable to exit from the stationary phase and

resume aerobic growth at 37 ºC.[16] This complex is less sensitive to cyanide or azide, partly because the heme groups are buried deeply in the hydrophobic core of the enzyme, limiting the access of charged species like cyanide or azide.[7] However, aurachin D specifically inhibits cytochrome *bd* complex, but not the *bo3* complex.[17]

Oxidative Stress in *E. coli*

Molecular oxygen (O_2) serves as an excellent electron acceptor for cellular respiration, as evident by the number of protons (xx give number) pumped to the periplasm per cycle.[7] However, adventitious reduction of oxygen poses great danger to cellular growth and survival.[18] O_2 by itself does not cause much damage to *E. coli*. This is because O_2 is a diradical; any adventitious reductions must occur through accepting one electron at a time because two-electron reduction (triplet-to-singlet) is generally spin-forbidden.[18] Nonetheless, many redox enzymes possess the ability to reduce oxygen at a slow rate. The byproducts of these oxygen reactions are commonly termed as reactive oxygen species (ROS) (**Figure 2.1**).[19] ROS generally refers to superoxide (O_2^-), hydrogen peroxide (H_2O_2), and hydroxyl radical ($\cdot OH$). The accumulation of ROS inside a cell is detrimental, exemplified by the multiple growth defects in aerobically grown *E. coli* mutants that lack ROS scavenging proteins.[18]

What then is the source of ROS in *E. coli* cells? The major source of ROS in *E. coli* is currently unknown.[18] However, it is clear that respiration is one important source of ROS.[18] This is especially true in mitochondria. The major source of ROS in healthy eukaryotic cells is mitochondria, especially from the Complex I and III in the electron transport chain.[20] Similarly, Imlay and coworkers have found that NDH-II complex produces ROS by adventitious oxidation of reduced flavin cofactor.[21] They further showed that flavoenzymes such as succinate

dehydrogenase, fumarate reductase, and NDH-I complex produce H_2O_2 upon the oxidation of flavin cofactors, a process known as autoxidation.[22] In addition, they also showed that menaquinol is a source of ROS in the periplasm.[23]

What damage does O_2^- and H_2O_2 impose on cellular machinery? Superoxide is not a strong oxidant at physiological pH partly because the charge repulsion from an electron-rich reductant destabilizes the interaction with negatively charged superoxide. Instead, superoxide is a mild oxidant that does not seem to react significantly with nucleic acid, amino acids, and most carbohydrates.[22] However, SOD-deficient mutants cannot grow when branched chain amino acids are not supplemented, and they grow poorly on non-fermentable carbon substrates, such as acetate and fumarate.[24] This is because enzymes that utilizes 4Fe-4S clusters, such as dihydroxyacid dehydratase (a common enzyme for branched chain amino acid synthesis), acotinases, and fumarases are damaged. Further studies showed that, in the absence of a substrate, the surface-exposed iron in 4Fe-4S cluster in these enzymes can be complexed with O_2^-. Subsequent protonation and electron transfer generates H_2O_2 while releasing the Fe^{2+} from the 4Fe-4S cluster (**Figure 2.3**). This reaction causes loss of enzymatic function.[22] The rate constant for this reaction is ~ 10^6 to 10^7 $M^{-1}s^{-1}$.[22]

H_2O_2 can act as either a univalent or divalent oxidant. Although the reduction of H_2O_2 is generally thermodynamically favored, the high activation energy of breaking a dioxygen bond in H_2O_2 prevents it from reacting with most biomolecules. This is surprising because the addition of H_2O_2 to lab media will immediately stop the growth of most cells and prolong exposure will result in the loss of cell viability.[25] It has been suggested that the generation of hydroxyl radical from the univalent reduction of H_2O_2 by oxidation of Fe^{2+} is the toxic effect:

$$Fe^{2+} + H_2O_2 \rightarrow OH^- + \cdot OH + Fe^{3+} \quad (1)$$

This reaction is called Fenton reaction. Although many heavy metal ions can potentially produce hydroxyl radical through a similar reaction pathway, iron is the most likely source of the Fenton reaction in live *E. coli* cells because of its abundance in the bacterial cytoplasm (~ 1 mM).[19] The resulted hydroxyl radical can react at nearly diffusion-limited rates with most organic molecules, such as nucleic acids, amino acids, lipids, and carbohydrates.

E. coli in air saturated medium produces O_2^- and H_2O_2 at a rate of 5 μM/s and 10 μM/s, respectively.[18] The cells reduce the intracellular concentration of O_2^- and H_2O_2 through the action of superoxide dismutase (SOD) and catalases/peroxidases, respectively. The defense against ROS formation needs to be robust to ensure proper cell growth and survival.

E. *coli* encodes two cytoplasmic SODs (Mn-SOD and Fe-SOD) and one periplasmic SOD (CuZn-SOD).[22] These enzymes react with superoxide, producing hydrogen peroxide as a byproduct. The cytoplasmic SOD is encoded by gene *sodA* and *sodB* with a total concentration of ~20 μM.[26] These SODs dismutate superoxide almost at the diffusion limited rate (~10^8- 10^9 $M^{-1}s^{-1}$).[27] Their transcription is modulated by oxygen and iron concentration. The periplasmic SOD activity is comparable to its cytoplasmic counterparts, but the transcription of CuZn-SOD is not modulated by OxyR and SoxRS.[18] For more information on transcriptional control of scavenger proteins and survival, please refer to reference 23.

Intracellular hydrogen peroxide is reduced to water by peroxidase and catalases. There are two catalases encoded by *katG* and *katE*, but only one is expressed at a given time. During the exponential phase of *E. coli*, *katG* is dominantly expressed and controlled by OxyR regulon.[28] Upon entering the stationary phase, *katE* expression elevates by induction from RpoS, a

transcription sigma factor responsible for stationary phase.[29] Alkylhydroperoxide reductase (Ahp) is also present in *E. coli* with k_{cat}/K_m of 4 x 10^7 $M^{-1}s^{-1}$.[30] This enzyme is effective at low micromolar concentration of H_2O_2, but it is inactivated at higher doses of H_2O_2.

The steady state concentrations of O_2^- and H_2O_2 are calculated as 0.2 nM and 20 nM, respectively, based on the number of scavenger proteins and their rate constants.[18] This number signifies that the cellular concentration of these species are kept low (<1 molecule of O_2^- and ~20 molecules of H_2O_2 per cell on average) even though their production rate is quite fast. This low steady state concentration of ROS allows *E. coli* cells to flourish in air-rich environments while utilizing oxygen as a terminal electron acceptor (**Figure 2.4**). However, any imbalance of ROS scavenging activity or overproduction of ROS from overactive electron transport chains easily leads to growth defect and possible death. In some cases, ROS may enhance cell death caused by bactericidal antibiotics.[31]

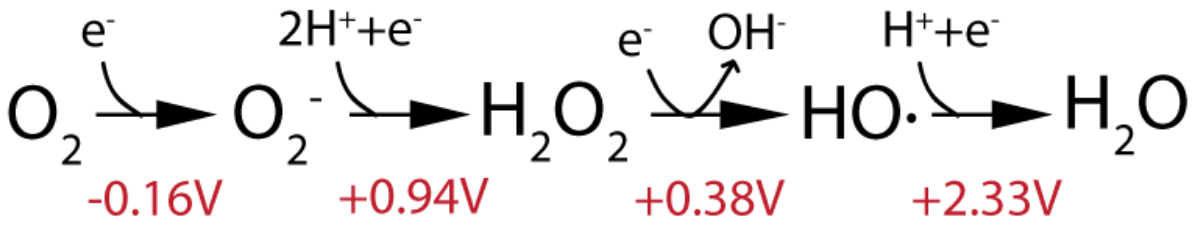

Figure 2.1 Reduction potential of one-electron reduction of molecular oxygen (O_2).

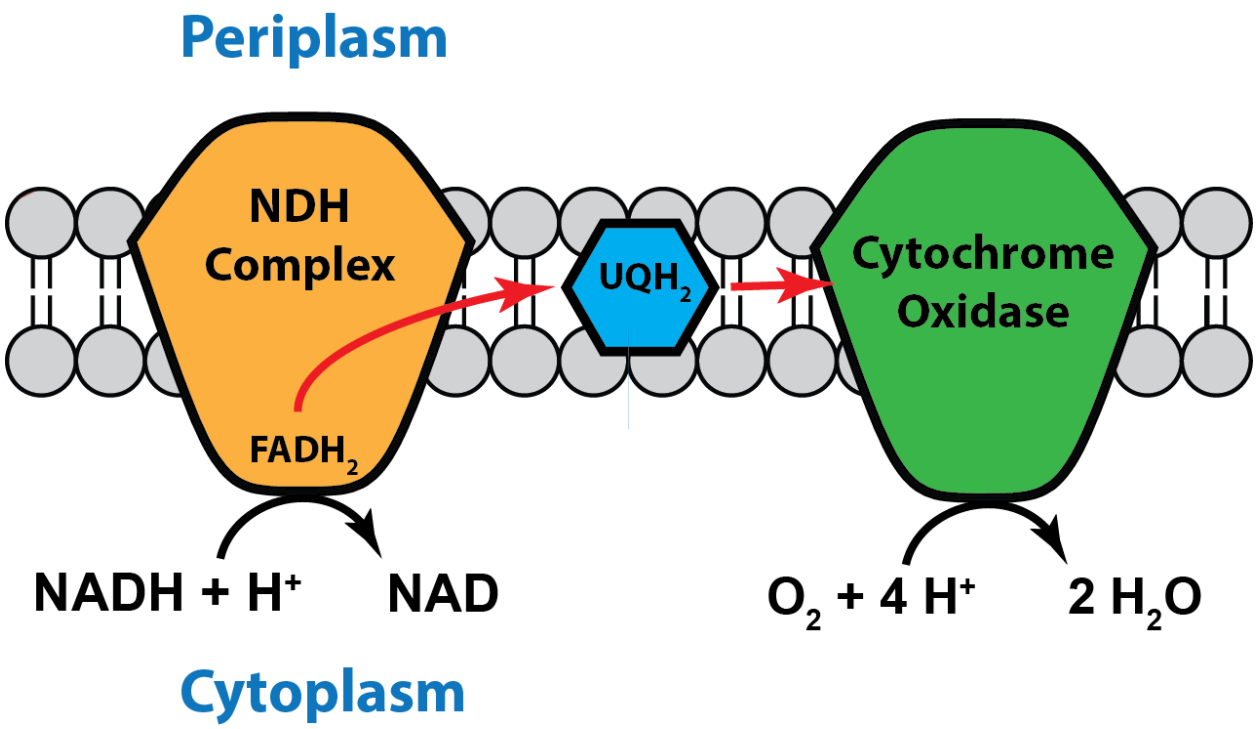

Figure 2.2 Depiction of electron transport chain (ETC) in *E. coli* under aerobic conditions. The electron flows from NADH.

Couple	E' (mV)
NAD/NADH[3]	-320
FeS(ox/red)	-305
FAD/FADH2[3]	-220
FMN/FMNH2[3]	-197
Menaquinone/Menaquinol[7]	-74
Ubiquinone/Ubiquinol[7]	+110
Heme b_{558}, b_{595}[7]	+160 to +170
Heme *b, o3, d* (ox/red)[7]	+260 to +280
Cyt a (ox/red)	+290
Fe^{3+}/Fe^{2+}	+771

Table 2.1 Standard reduction potential (pH 7) for molecules in oxidative phosphorylation.

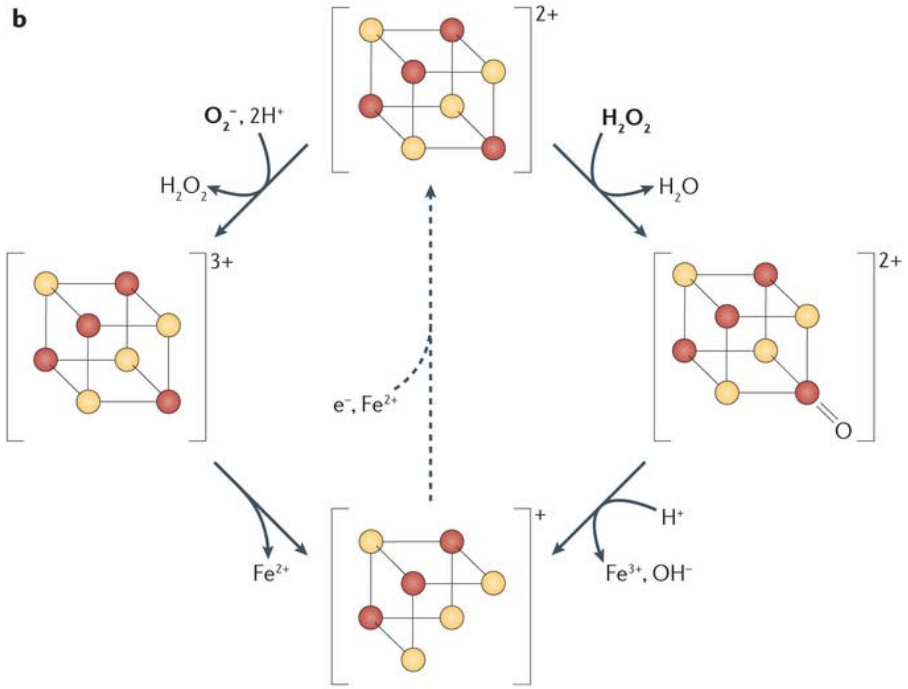

Figure 2.3 Proposed mechanism for inactivation of dehydratase 4Fe-4S cluster by superoxide (Left) and hydrogen peroxide (Right).[18] The figure is adopted from Imlay's review.

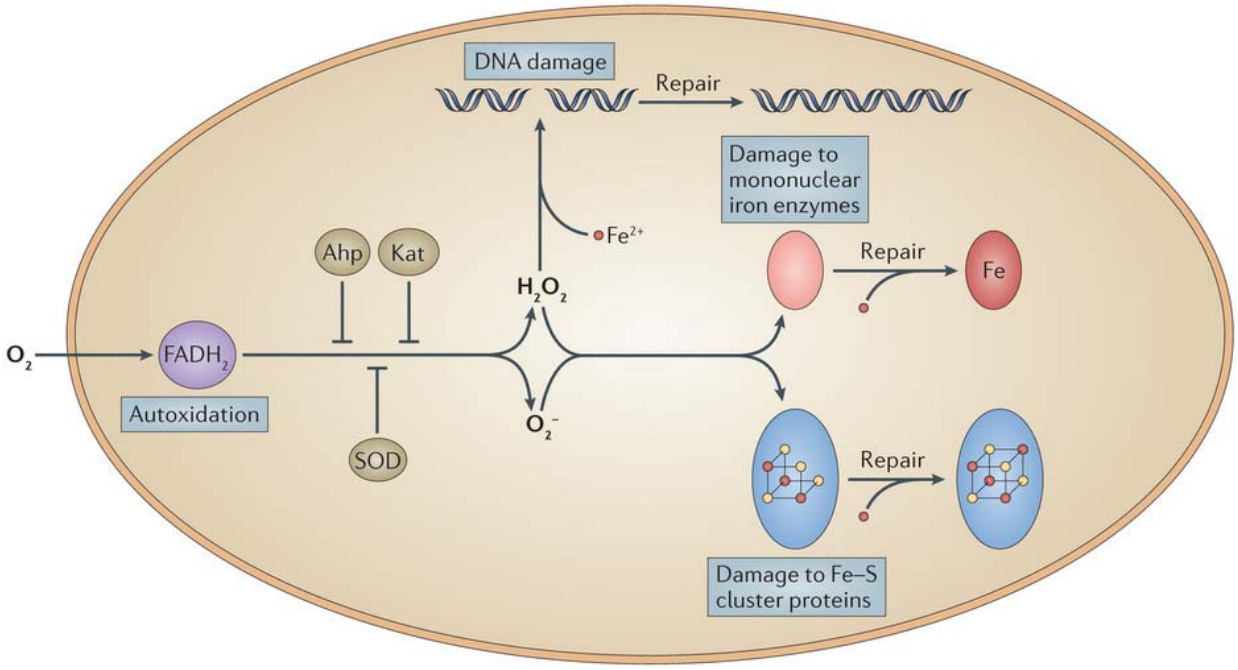

Figure 2.4 Reactive oxygen species formed in *E. coli* during aerobic growth.[18] This figure is adopted from Imlay's review.

References

1. Unden, G.; Bongaerts, J., Alternative respiratory pathways of Escherichia coli: Energetics and transcriptional regulation in response to electron acceptors. *Biochimica Et Biophysica Acta-Bioenergetics* **1997,** *1320* (3), 217-234.

2. Unden, G.; Stenmetz, P. A.; Degreif-Dunnwald, P., The Aerobic and Anaerobic Respiratory Chain of Escherichia coli and Salmonella enterica: Enzymes and Energetics. *EcoSalPlus* **2014**.

3. Friedrich, T.; Pohl, T., NADH as Donor. *EcoSalPlus* **2014**.

4. Guenebaut, V.; Schlitt, A.; Weiss, H.; Leonard, K.; Friedrich, T., Consistent structure between bacterial and mitochondrial NADH : ubiquinone oxidoreductase (complex I). *Journal of Molecular Biology* **1998,** *276* (1), 105-112.

5. Tran, Q. H.; Bongaerts, J.; Vlad, D.; Unden, G., Requirement for the proton-pumping NADH dehydrogenase I of Escherichia coli in respiration of NADH to fumarate and its bioenergetic implications. *European Journal of Biochemistry* **1997,** *244* (1), 155-160.

6. Ashcroft, J. R.; Haddock, B. A., Synthesis of alternative membrane-bound redox carriers during aerobic growth of Escherichia coli in the presence of potassium cyanide. *Biochem J* **1975,** *148* (2), 349-52.

7. Borisov, V. B.; MVerkhovsky, M. I., Oxygen as Acceptor. *EcoSalPlus* **2009**.

8. Poole, R.; Cook, G., Redundancy of aerobic respiratory chains in bacteria? Routes, reasons and regulation. *Advances In Microbial Physiology* **2000,** *43*, 165-224.

9. Svensson, M.; Nilsson, T., Flow-flash study of the reaction between cytochrome bo and oxygen. *Biochemistry* **1993,** *32* (20), 5442-7.

10. Kita, K.; Konishi, K.; Anraku, Y., Terminal oxidases of Escherichia coli aerobic respiratory chain. II. Purification and properties of cytochrome b558-d complex from cells grown with limited oxygen and evidence of branched electron-carrying systems. *J Biol Chem* **1984,** *259* (5), 3375-81.

11. Belevich, I.; Borisov, V. B.; Konstantinov, A. A.; Verkhovsky, M. I., Oxygenated complex of cytochrome bd from Escherichia coli: stability and photolability. *FEBS Lett* **2005,** *579* (21), 4567-70.

12. Yang, K.; Zhang, J.; Vakkasoglu, A. S.; Hielscher, R.; Osborne, J. P.; Hemp, J.; Miyoshi, H.; Hellwig, P.; Gennis, R. B., Glutamate 107 in subunit I of the cytochrome bd quinol oxidase from Escherichia coli is protonated and near the heme d/heme b595 binuclear center. *Biochemistry* **2007,** *46* (11), 3270-8.

13. Hill, S.; Viollet, S.; Smith, A. T.; Anthony, C., Roles for enteric d-type cytochrome oxidase in N2 fixation and microaerobiosis. *J Bacteriol* **1990,** *172* (4), 2071-8.

14. Avetisyan, A. V.; Bogachev, A. V.; Murtasina, R. A.; Skulachev, V. P., Involvement of a d-type oxidase in the Na(+)-motive respiratory chain of Escherichia coli growing under low delta mu H+ conditions. *FEBS Lett* **1992,** *306* (2-3), 199-202.

15. Delaney, J. M.; Wall, D.; Georgopoulos, C., Molecular characterization of the Escherichia coli htrD gene: cloning, sequence, regulation, and involvement with cytochrome d oxidase. *J Bacteriol* **1993,** *175* (1), 166-75.

16. Siegele, D. A.; Imlay, K. R.; Imlay, J. A., The stationary-phase-exit defect of cydC (surB) mutants is due to the lack of a functional terminal cytochrome oxidase. *J Bacteriol* **1996,** *178* (21), 6091-6.

17. Meunier, B.; Madgwick, S. A.; Reil, E.; Oettmeier, W.; Rich, P. R., New inhibitors of the quinol oxidation sites of bacterial cytochromes bo and bd. *Biochemistry* **1995,** *34* (3), 1076-83.

18. Imlay, J. A., The molecular mechanisms and physiological consequences of oxidative stress: lessons from a model bacterium. *Nat. Rev. Microbiol.* **2013,** *11* (7), 443-454.

19. Imlay, J. A., Pathways of oxidative damage. *Annual Review of Microbiology* **2003,** *57*, 395-418.

20. Chen, Q.; Vazquez, E. J.; Moghaddas, S.; Hoppel, C. L.; Lesnefsky, E. J., Production of reactive oxygen species by mitochondria: central role of complex III. *J Biol Chem* **2003,** *278* (38), 36027-31.

21. Massey, V.; Strickland, S.; Mayhew, S. G.; Howell, L. G.; Engel, P. C.; Matthews, R. G.; Schuman, M.; Sullivan, P. A., The production of superoxide anion radicals in the reaction of reduced flavins and flavoproteins with molecular oxygen. *Biochem Biophys Res Commun* **1969,** *36* (6), 891-7.

22. Imlay, J. A., Oxidative Stress. *EcoSalPlus* **2009**.

23. Kona, J.; Brinck, T., A combined molecular dynamics simulation and quantum chemical study on the mechanism for activation of the OxyR transcription factor by hydrogen peroxide. *Org Biomol Chem* **2006,** *4* (18), 3468-78.

24. Blanchard, J. L.; Wholey, W. Y.; Conlon, E. M.; Pomposiello, P. J., Rapid changes in gene expression dynamics in response to superoxide reveal SoxRS-dependent and independent transcriptional networks. *PLoS One* **2007,** *2* (11), e1186.

25. Imlay, J. A.; Linn, S., Bimodal pattern of killing of DNA-repair-defective or anoxically grown Escherichia coli by hydrogen peroxide. *J Bacteriol* **1986,** *166* (2), 519-27.

26. Imlay, J. A.; Linn, S., Mutagenesis and stress responses induced in Escherichia coli by hydrogen peroxide. *J Bacteriol* **1987,** *169* (7), 2967-76.

27. Pomposiello, P. J.; Bennik, M. H.; Demple, B., Genome-wide transcriptional profiling of the Escherichia coli responses to superoxide stress and sodium salicylate. *J Bacteriol* **2001,** *183* (13), 3890-902.

28. Zhao, G.; Ceci, P.; Ilari, A.; Giangiacomo, L.; Laue, T. M.; Chiancone, E.; Chasteen, N. D., Iron and hydrogen peroxide detoxification properties of DNA-binding protein from starved cells. A ferritin-like DNA-binding protein of Escherichia coli. *J Biol Chem* **2002,** *277* (31), 27689-96.

29. Patten, C. L.; Kirchhof, M. G.; Schertzberg, M. R.; Morton, R. A.; Schellhorn, H. E., Microarray analysis of RpoS-mediated gene expression in Escherichia coli K-12. *Mol Genet Genomics* **2004,** *272* (5), 580-91.

30. Park, S.; Imlay, J. A., High levels of intracellular cysteine promote oxidative DNA damage by driving the Fenton reaction. *J. Bacteriol.* **2003,** *185* (6), 1942-1950.

31. Kohanski, M. A.; Dwyer, D. J.; Hayete, B.; Lawrence, C. A.; Collins, J. J., A common mechanism of cellular death induced by bactericidal antibiotics. *Cell* **2007,** *130* (5), 797-810.

Chapter 3

Single-cell, Real-time Detection of Oxidative Stress Induced in *E. coli* by the Antimicrobial Peptide CM15

A portion of the research described in this chapter has been published in:

Choi H., Yang Z., Weisshaar J.C. "Single-cell, Real-time Detection of Oxidative Stress Induced in *E. coli* by the Antimicrobial Peptide CM15." PNAS. **112,** 2015.

INTRODUCTION

In nature, multicellular organisms produce antimicrobial peptides (AMPs) that participate in the first line of defense against bacterial infection.[1] These are ancient molecules that kill a broad, phylogenetically diverse spectrum of bacteria. The selective bacteriostatic (growth-halting) properties of cationic AMPs are most often attributed to their ability to compromise bacterial membranes while leaving eukaryotic cell membranes relatively unharmed. On entry into the periplasm or cytoplasm, various AMPs are known to interfere with cell wall growth, cause loss of osmotic pressure, and degrade the trans-membrane potential. [2] Here we report direct, real-time evidence of oxidative damage induced in the *E. coli* cytoplasm by the synthetic hybrid antimicrobial peptide CM15. The CM15 sequence KWKLFKKIGAVLKVL-NH_2 combines residues 1–7 of cecropin A (from moth) and residues 2–9 of melittin (bee venom). The hybrid retains the potency of cecropin A against multiple species of bacteria without the hemolytic activity of melittin.[3]

Our single-cell, real time, fluorescence assays demonstrate that CM15 translocates across the outer membrane (OM) without permeabilization to periplasmic GFP, then permeabilizes the cytoplasmic membrane (CM), causing abrupt cell shrinkage. Three different intracellular fluorescence signals indicate the onset of oxidative stress within 30 s of cell shrinkage: enhanced cytoplasmic autofluorescence from oxidized flavins, a burst of fluorescence from the permeable dye CellROX Green (known to detect O_2^- and •OH), and a burst of fluorescence from resorufin (the product of the Amplex Red assay, known to specifically detect H_2O_2). Evidently active aerobic respiration is a prerequisite for CM15 to induce oxidative stress. Importantly, in anaerobic growth conditions the CellROX* and resorufin signals decrease significantly and the minimum inhibitory concentration (MIC) increases 20-fold. Oxidative stress is a key component

of the growth-halting capability of CM15. The same may be true of many natural cationic AMPs, as suggested by preliminary results for LL-37 and cecropin A.

It is increasingly clear that AMPs launch multi-pronged attacks on bacterial cells.[4] The same may be true of synthetic antibiotics. A series of recent reports indicates that in addition to their target-specific action, bactericidal drugs such as norfloxacin, ampicillin, and kanamycin also induce oxidative stress in the cytoplasm of strains of *E. coli* and *S. aureus*.[5] These results have been controversial.[6] Nevertheless, oxidative damage may prove to be an important downstream effect of a wide variety of antimicrobial agents. Our new methods enable detection of ROS within the cytoplasm of single cells with 12-s time resolution, a capability that should prove useful in a variety of contexts.

METHODS

Bacterial strains, growth conditions, and materials

The background strain is MG1655 in all cases. For experiments on periplasmic GFP, TorA-GFP was expressed from a plasmid pJW1 as previously described.[7] APEX2 was expressed using tetracycline in same manner as TorA-GFP. The strain with *parS*-ParB-GFP labeling of the DNA locus called "Right2" was received from Boccard lab.[8]

Bulk cultures were grown in EZ rich defined medium (EZRDM),[9] which contains a MOPS-buffered solution with supplemented metal ions (M2130; Teknova), glucose (2 mg/mL), supplemental amino acids and vitamins (M2104; Teknova), nitrogenous bases (M2103; Teknova), 1.32 mM K_2HPO_4, and 76 mM NaCl. Cultures were grown from glycerol frozen stock to stationary phase overnight at 30°C. Subcultures were grown to exponential phase (OD = 0.2-0.6 at 600 nm) before sampling for the microscopy experiments at 30°C, unless otherwise specified.

We received *L*-CM15 with C-terminal amidation from Dr. Jimmy Feix (Wisconsin Medical College). The sequence is: KWKLFKKIGAVLKVL-NH_2. The oxidation sensitive dye CellROX Green (Stock Item No. C10444) and Amplex Red (A22188) was purchased from Invitrogen. Other chemicals are listed in detail in SI.

Minimum inhibitory concentration assay (MIC)

The MIC for CM15 was determined using a broth microdilution method as previously described.[10] Two-fold serial dilutions of CM15 in 1X EZRDM were performed in separate rows of a polystyrene 96-well plate with each plate containing an inoculum of *E. coli* MG1655. The inoculum was a 1:20 dilution from a bulk culture at midlog phase (OD_{600} = 0.5) grown at 30°C. The plate was incubated at 30°C and shaken at 200 rpm in a Lab-Line Orbital Environ Shaker (Model 3527) for 6 hr for aerobic MIC measurements. The MIC values were taken as the lowest concentration for which no growth was discernible (<0.05 O.D) after 6 hr. The MIC value was 5 μM for *L*-CM15.

The anaerobic MIC was measured on a 96-well plate that was sealed with plastic wrap. Cells were incubated in EZRDM containing protocatechuic acid (PCA) at 10 mM and protocatechuate 3,4-dioxygenase (PCD) at 100 nM to scavenge oxygen.[11] The plate was incubated at 30°C for 6 hr, followed by OD measurements. We tested that PCA by itself does not interfere with the CM15-induced burst of CellROX* fluorescence (Appendix 3G).

Microfluidics chamber for aerobic and anaerobic measurements

Imaging of individual cells was carried out at 30ºC in a simple microfluidics chamber consisting of a single rectilinear channel of uniform height of 50 μm and width of 6 mm, with a channel length of 11 mm. The total chamber volume is ~10 μL. The negative of the cell design was patterned onto a silicon wafer via photolithography and the wafer was silanized. Sylgard 184 silicone elastomer mixture (Dow Corning) was poured on to the patterned silicon wafer and baked for 24 hours in a 37°C incubator after removing air in a vacuum desiccator. The cured polydimethylsiloxane (PDMS) slab was removed and holes were punched for entry and exit hypodermic needles. The patterned PDMS slab was fused to a dried, acetone-cleaned, 22-mm x 40-mm glass coverslip pre-cleaned by plasma oxidation. Soon after the bonding of the two pieces, 0.01% poly-*L*-lysine (molecular weight >150,000 Da) was injected through the chamber for 30 min and rinsed thoroughly with millipore water. For imaging experiments, the chamber was maintained at 30°C with a TC-344B dual automatic temperature controller through the CC-28 cable assembly attached to RH-2 heater blocks (Warner Instruments).

The PDMS ceiling of the microfluidics device is permeable to the ambient gases N_2 and O_2. For anaerobic imaging experiments, we needed to prevent O_2 from entering the chamber through its ceiling. A small anaerobic chamber surrounding the microfluidics device was constructed of aluminum with a nitrogen gas inlet and outlet. Prior to injection of cells, nitrogen gas flowed through the chamber continuously for 1.5 hr. *E. coli* were grown in aerobic conditions until injected to the chamber. Fresh de-oxygenated EZRDM was made by treating EZRDM with 50 nM protocatechuate 3,4-dioxygenase (PCD) and 2.5 mM protocatechuic acid (PCA). This was used to wash the cells at 30°C prior to plating. De-oxygenated EZRDM then flowed across the plated cells for 30 min prior to injection of CM15 and CellROX. The subsequent microscopy imaging experiment was carried out as before.

Microscopy

Single-cell imaging was performed on two different microscopes: a Nikon TE300 inverted microscope with a 100X, 1.3 NA phase contrast objective (Nikon) and Nikon Eclipse Ti inverted microscope with a 100X, 1.45 NA phase contrast objective (Nikon). For the Nikon TE300, images were further magnified 1.45X in a home-built magnification box. A line tunable Ar^+ laser (Melles Griot) at 488 nm or 457 nm was expanded to illuminate the field of view uniformly. Laser intensities at the sample were ~10 W/cm^2 at 457 nm and ~5 W/cm^2 at 488 nm. Fluorescence images were obtained with an EMCCD camera, either Andor iXon 897 or Andor iXon 887. In both cases, the pixel size corresponds to 110 ± 10 nm at the sample.

All emission filters were purchased from Chroma Technology. Specific emission filters were: 495LP (long-pass) for observation of autofluorescence after 457-nm excitation and HQ525/50 for observation of GFP or CellROX after 488-nm excitation and HQ617/70 for resorufin after 561-nm excitation.

Unless otherwise noted, time-lapse movies of 60-min total duration were obtained as 600 frames of 50-ms exposure time each, with fluorescence and phase contrast images interleaved at 6-s intervals (12 s per complete cycle). A movie begins immediately after adhesion of cells and the rinsing away of extra cells. The cells were imaged for ~5 min before injection of fresh medium containing the compounds under study (CM15, CellROX, etc).

Measurement of single-cell autofluorescence

To obtain the fluorescence spectrum of normal MG1655 autofluorescence (**Figure 3.2b**), a cell culture grown at 30°C to OD_{600} ~ 0.4 was sampled onto a black 96-well plate. The emission spectrum was obtained using a Tecan Infinite M1000 fluorimeter with excitation at 457 nm. For comparison, the fluorescence spectrum of 100 μM FAD was obtained under the same instrumental conditions (**Figure 3.3a**).

For the single-cell autofluorescence measurements under the microscope, cells are excited by the Ar^+ laser at 457 nm after passage through a notch filter (Z458/10X) to eliminate plasma radiation. The emission through filter HQ525/50 was imaged. Movies were initiated ~5 min before changing the flow from normal aerated growth medium to aerated growth medium containing CM15 at 10 μM or H_2O_2 at 10 μM. For comparisons of autofluorescence intensity under different treatments, the laser intensity and camera gain were kept constant.

CellROX Green oxidation assay

CellROX Green is a proprietary oxidation-sensitive dye whose fluorescence quantum yield at 500-550 nm after excitation at 488 nm increases dramatically on oxidation in the presence of ds-DNA. It readily permeates both *E. coli* membranes. The manufacturer tested its sensitivity to different reactive oxygen species in the presence of ds-DNA *in vitro* including hydroxyl radical (•OH), superoxide (O_2^-), hydrogen peroxide (H_2O_2), peroxynitrite ($ONOO^-$), nitric oxide (NO), and hypochlorite (ClO^-). The only two oxidizing agents that significantly enhanced CellROX fluorescence were hydroxyl radical and superoxide. Importantly, hydrogen peroxide has no effect.

In the basic CellROX* imaging experiments, MG1655 cells were injected into the microfluidics chamber. After allowing 5 min for plating of cells, the bulk solution was washed

away with fresh, pre-warmed, aerated EZRDM. After the wash, cells were grown for 5 min prior to the injection of 10 μM CM15 with 2.5 μM CellROX. CellROX fluorescence after 488 nm excitation was monitored through emission filter HQ525/50. The laser intensity at the sample was ~2.5 W/cm^2. To maintain good aeration and steady bulk concentrations, the medium with CM15 and CellROX flowed continuously at 0.3 mL/hr.

In attempts to intercept cycling of the Fenton reaction by chelating available cytoplasmic iron, cells were incubated in 1 mM of 2,2' dipyridyl for 5 min after plating and prior to the injection of CM15.

Amplex Red oxidation assay

We developed a single-cell, time-resolved measurement of H_2O_2 production following CM15 treatment. The assay is based on the well established Amplex Red method. Some peroxidases (not the catalases naturally occurring in *E. coli*) catalyze reaction of the dye Amplex Red with H_2O_2 to form the fluorescent species resorufin (λ_{em} = 585 nm). To measure the rate of H_2O_2 production under normal metabolism, Imlay and co-workers[12] studied an HPX^- mutant strain of *E. coli* (lacking catalase). The permeable H_2O_2 escapes the cell and undergoes a bulk reaction with Amplex Red, catalyzed by horseradish peroxidase (HRP). The product is resorufin, which absorbs at 570 nm and fluoresces strongly at 585 nm. The time resolution of this method was ~5 min. Recently Collins and co-workers[5c] adapted the method to carry out the Amplex Red + H_2O_2 reaction inside the cytoplasm by inserting a plasmid that expresses the peroxidase APEX2 (mutated ascorbate peroxidase) within the cytoplasm. H_2O_2 was detected after it diffused out of the cell. The time resolution was ~60 min. Here we use the Collins adaptation with single-cell, time-resolved fluorescence detection in the microfluidics chamber.

This enables sensitive detection of H_2O_2 production with 12-s time resolution and correlation of CM15-induced H_2O_2 production with other events in real time.

RESULTS

Disruption of *E. coli* membranes by CM15

We used previously developed single-cell, real-time imaging assays[10, 13] to monitor the disruption of K12 *E. coli* membranes by CM15. The modified K12 cells include a plasmid to express GFP with the twin-Arginine translocase signal peptide appended to the N-terminus. GFP folds in the cytoplasm and is exported to the periplasm, where it is mobile.[14] Cells are plated in a microfluidics chamber and are growing in continuously refreshed, aerated medium. On excitation at 488 nm, the resulting cells exhibit a halo of green fluorescence (**Figure 3.1**), indicating a predominantly periplasmic spatial distribution of GFP. Fluorescence images are interleaved with phase contrast images that monitor cell length vs time to a precision of ±50 nm. One full imaging cycle is completed every 12 s.

At $t = 0$, we initiate flow of 10 μM CM15 (twice the 6-hr MIC, Appendix 3A) in EZRDM medium through the microfluidics chamber and begin imaging single cells. For at least 85% of the cells in a typical field of 25 cells, within 12-24 s of CM15 injection we observe abrupt shrinkage of the cell length and simultaneous migration of GFP from the periplasm into the cytoplasm (Movie S1). Similar events occur later for the remainder of cells. For one representative non-septating cell, Figs. 1a and b show a phase contrast image and the transverse fluorescence intensity profile before and after the shrinkage event. Figure 1c shows the time evolution of total GFP fluorescence intensity and of tip-to-tip cell length. The inward movement of GFP implies rapid translocation of the peptide across the outer membrane (OM) without permeabilization to GFP, followed by permeabilization of the cytoplasmic membrane (CM) to

GFP.[10] Diffusive transfer of most GFP to the cytoplasm is driven by the large cytoplasmic volume compared with the periplasmic volume. We suspect that cell shrinkage is due to leakage of small osmolytes across the CM and consequent loss of turgor pressure. Much later, at ~30 min after cell shrinkage, each cell abruptly loses essentially all GFP fluorescence, indicating that the OM has also been permeabilized to GFP (**Figure 3.1a**). Meanwhile, phase contrast is retained, showing that the chromosomal DNA and larger cytoplasmic components such as ribosomes are retained within the cell envelope.

Our subsequent studies of oxidative stress used wild-type K12 cells (not expressing GFP) to enable clean observation of signals from fluorescent probes of oxidative stress. At the same CM15 concentration of 10 μM, most wild-type cells exhibit cell shrinkage on a similarly rapid timescale of 12–24 s after injection of CM15. The moment of cell shrinkage observed in the phase contrast images serves as a non-fluorescent marker of the time of permeabilization of the CM to GFP, and presumably also to the much smaller CM15.

Enhancement of cellular autofluorescence by CM15 in aerobic conditions

The first probe of oxidative stress measures the intensity of cellular autofluorescence excited at 457 nm as a function of time after CM15 addition. At this excitation wavelength, the autofluorescence of *E. coli* is dominated by the oxidized forms of riboflavin (which is soluble) and flavin nucleotides (such as FAD and FMN). These share a common chromophore which is non-fluorescent in its fully reduced form but becomes weakly fluorescent when fully oxidized.[15] In **Figure 3.2a**, we compare emission spectra from a solution of FAD and a suspension of K12 *E. coli*, both excited at 457 nm. The agreement confirms flavin nucleotides and riboflavins as the likely source of cellular autofluorescence. The transverse spatial distribution is that of a filled

cytoplasm, indicating that cellular autofluorescence is predominantly due to soluble flavins and flavin co-factors bound to soluble enzymes, not membrane-bound species.

Plots of total autofluorescence intensity and cell length vs time for one representative cell are shown in **Figure 3.2b**. The autofluorescence intensity begins to increase within 30 s of cell shrinkage. Evidently the cytoplasm has become more oxidizing. Over the next 2 min, the intensity rises to a plateau value 2-3 times as large as the pre-CM15 level. Prior to permeabilization of the cytoplasmic membrane by CM15, the autofluorescence decreases due to photobleaching. The broad plateau after CM15 action is likely due to a balance between photobleaching and continuing production of oxidized flavins and riboflavins. This same behavior was observed in all cells (typically at least 20) in each of five experiments.

Enhancement of CellROX Green fluorescence by CM15 in aerobic conditions

We have devised single-cell, time-resolved tests of the hypothesis that the oxidative stress induced by CM15 arises from enhanced production of some combination of the reactive oxygen species (ROS) superoxide (O_2^-), hydrogen peroxide (H_2O_2), or hydroxyl radical (•OH). *In vitro*, the permeable dye CellROX Green is oxidized by O_2^- and •OH, but not by H_2O_2.[16] We call reduced CellROX Green "CellROX", and the fluorescent, oxidized form "CellROX*". As added, CellROX exhibits very weak fluorescence. *In vitro*, oxidation of CellROX by superoxide (presumably in its protonated •OOH form) or •OH induces strong CellROX* fluorescence (excited at 488 nm and detected at 525 ± 25 nm), but only in the presence of ds-DNA, to which it must bind in order to fluoresce efficiently. In SI (Appendix 3B), we describe *in vitro* tests that confirm that O_2^- in the presence of dsDNA can induce CellROX* fluorescence. The tests also show that the Fe^{2+} in either superoxide dismutase (SOD) or horseradish peroxidase (HRP) is unable to induce CellROX* fluorescence. *In vitro*, we observe no CellROX* fluorescence in the

presence of 1 mM H_2O_2. To confirm that H_2O_2 itself cannot induce CellROX* fluorescence *in vivo*, we continuously flowed 10 μM H_2O_2 in PBS across plated K12 cells in the absence of CM15.

No CellROX* fluorescence was observed (Appendix 3C). This also indicates that the ambient Fe^{2+} concentration is too low to drive sufficient •OH from Fenton chemistry quickly enough to produce observable CellROX* fluorescence.[17]

We injected CM15 at 10 μM plus CellROX at 2.5 μM onto plated K12 cells at $t = 0$. As shown in **Figure 3.3a**, strong CellROX* fluorescence begins to rise within 12 s of the abrupt cell shrinkage event (Movie S2). The CellROX* intensity peaks ~1 min later. Over the next 5 min, the signal decreases towards a plateau value. Evidently the fluorescent state CellROX* is being destroyed, perhaps by subsequent oxidative damage to the fluorophore; see below. The spatial distribution of the fluorescence intensity is that of the nucleoids, including well separated primary nucleoid lobes and also secondary sub-lobes (**Figure 3.3a**).[18] This pattern confirms binding of the oxidized, fluorescent CellROX* species to DNA. Similar events occurred in all 56 cells observed for 40 min in two separate experiments. Addition of CellROX alone (no CM15) gives only a smaller, slowly rising signal (**Figure 3.3a**).

It was possible that CellROX was being oxidized in the bulk medium, entered the cell upon loss of membrane integrity, and became fluorescent on binding to DNA. We treated cells with 2% Triton X-100 (a non-ionic detergent) plus 2.5 μM CellROX, without CM15. This Triton X-100 treatment permeabilizes both *E. coli* membranes in ~1 min. Over 40 min, cells showed very little CellROX* fluorescence (**Figure 3.3d** and Appendix 3D).

Attenuation of CellROX* fluorescence in anaerobic conditions

If CellROX is oxidized primarily by O_2^- and/or •OH, then addition of CM15 to cells grown anaerobically should induce less CellROX* fluorescence. In the following single-cell studies, the plated cells have adapted to anaerobic conditions for 30 min and are growing in EZRDM. On addition of 10 μM CM15 (twice the *aerobic* MIC) to cells expressing periplasmic GFP, abrupt shrinkage occurred for all cells within 30 s. Subsequent events varied from cell to cell. About 25% of the cells showed behavior similar to that in aerobic conditions. Periplasmic GFP first migrated to the cytoplasm, and GFP was lost completely (permeabilization of the OM) only much later. Other behaviors include membrane blebbing, complete loss of GFP signal as the initial event, and formation of small "bubbles" containing GFP. A gallery of post-shrinkage GFP fluorescence patterns is provided in Appendix 3E.

Next we added 10 μM CM15 plus 2.5 μM CellROX to wild-type K12 cells growing in the anaerobic chamber. Abrupt cell shrinkage again occurred within 30 s. For all 43 cells in two different experiments, we observed an abrupt but small increase in CellROX* signal beginning within 12 s of cell shrinkage (example in **Figure 3.3b**). Comparing 11 well isolated cells in aerobic conditions with 15 well isolated cells in anaerobic conditions, the average peak amplitude was at least five times smaller in anaerobic conditions (**Figure 3.3d**). Evidently oxygen is a prerequisite for induction of a strong CellROX* by CM15.

Importantly, the 6-hr MIC of CM15 against K12 *E. coli* is 20-fold higher in anaerobic conditions (100 μM) than in aerobic conditions (5 μM) (Appendix 3A). This indicates that the oxidative stress induced by CM15 is an important factor in its bacteriostatic potency. While we observed cell shrinkage and other membrane-altering effects of CM15 at 10 μM in anaerobic conditions, evidently some cells survive and re-establish growth. The fivefold decrease in

CellROX* response in anaerobic conditions provides further evidence of ROS enhancement in aerobic conditions.

Below we will present evidence that the CM15-induced CellROX* signal observed in aerobic conditions requires a functional respiratory electron transport chain. To test whether a different functional electron transport chain behaves similarly, we grew cells anaerobically in a constant flow of EZRDM medium supplemented with 10 mM KNO_3 for 30 min, and then injected 10 μM CM15 along with 2.5 μM CellROX and 10 mM KNO_3. Under these conditions, cells respire using nitrate reductase as the terminal complex (instead of cytochrome oxidase) and menaquinone as the membrane-bound electron carrier (instead of ubiquinone).[19] The resulting mean peak CellROX* signal was 12 times lower than in aerobic conditions (**Figure 3.3d**). We do not know how the flux of electrons compares between the anaerobic nitrate reduction pathway and the aerobic oxygen reduction pathway. However, the result suggests that some feature specific to the aerobic electron transport chain facilitates the strong CM15-induced CellROX* signal.

Enhancement of resorufin fluorescence by CM15 in aerobic conditions

Next we developed a single-cell, time-resolved assay for H_2O_2 production following CM15 treatment. The assay is based on the established Amplex Red method used by Imlay and co-workers in their studies of HPX^- mutant strains.[12] Some peroxidases (not the catalases naturally occurring in *E. coli*) catalyze reaction of the non-fluorescent species Amplex Red with H_2O_2 to form the fluorescent species resorufin (emission at 585 nm). Following Collins and co-workers,[5c] we carried out the Amplex Red + H_2O_2 reaction inside the cytoplasm by inserting a plasmid that expresses the non-native peroxidase APEX2 (mutated ascorbate peroxidase). APEX2 is able to convert Amplex Red + H_2O_2 to resorufin.

We repeated the flow experiment in aerobic conditions using the K12 strain expressing APEX2. At $t = 0$, we flowed 10 μM of CM15 plus Amplex Red at 10 μM. A strong burst of resorufin fluorescence begins to rise within 12 s of cell shrinkage (**Figure 3.4a**, Movie S3). The signal peaks ~3 min after cell shrinkage and then partially decays over the next 20 min. All 23 observed cells exhibited similar behavior in aerobic conditions. In anaerobic conditions, there is little if any resorufin fluorescence after cell shrinkage (example in **Figure 3.4b**); the mean peak signal is at least a factor of 50 smaller than in aerobic conditions.

For aerobic conditions, in **Figure 3.4a** we compare the rising edge of resorufin signals averaged over 5 different cells with the rising edge of CellROX* signals (with and without pre-treatment with 2,2'-dipyridyl; see below). To place all signals on the same time axis, the traces are plotted with $t' = 0$ defined as the time of abrupt cell shrinkage. All three averaged signals rise at very similar times relative to the cell shrinkage event. It is possible that the resorufin signal (presumably arising from H_2O_2) may lag the CellROX* signal (presumably from O_2^- and/or •OH) by 1–2 frames, or 12-24 s, but the different overall shapes of the two signals prevents a firm conclusion.

Effects of chelation of free iron by 2,2'-dipyridyl in aerobic conditions

Thus far we have evidence of rapid, CM15-induced production of either O_2^- or •OH or both (from CellROX* fluorescence) and of H_2O_2 (from resorufin fluorescence) within 12–24 s of the cell shrinkage event. If CM15 were to cause a prompt burst of superoxide, at least part of the O_2^- would be rapidly converted to H_2O_2 by SOD. O_2^- is known to release Fe^{2+} from enzymes containing [4Fe–4S] clusters, such as dehydratases, and from mononuclear Fe-containing proteins.[17] Thus a prompt burst of O_2^- might quickly enhance both Fenton reactants ($H_2O_2 + Fe^{2+} \rightarrow$ •OH + OH^- + Fe^{3+}) and lead to a burst of •OH production.

The permeable iron chelating agent 2,2'-dipyridyl (here "dipyridyl") is known to efficiently chelate free iron (Fe^{2+}) and prevent Fenton chemistry in the cytoplasm.[20] In an attempt to dissect the CellROX* signal into contributions from O_2^- (induced by CM15) and from •OH (formed by Fenton chemistry), we pre-incubated K12 cells for 5 min with 1 mM of dipyridyl. After plating the pre-incubated cells, we initiated continuous flow of 10 μM CM15 plus 2.5 μM CellROX plus 1 mM dipyridyl and measured CellROX* fluorescence vs time. The signal begins to rise within 12 s of cell shrinkage and reaches a plateau ~2 min later (example in **Figure 3.3c**). The mean plateau value is about half of the mean peak level of CellROX* fluorescence absent dipyridyl (**Figure 3.3d**). In the presence of dipyridyl the CellROX* signal maintains its plateau level over 10 min. Without dipyridyl, about half of the CellROX* signal decays over 5 min (**Figure 3.3a**). Evidently dipyridyl prevents formation of part of the oxidants that form CellROX*, and also all of the oxidants that degrade the CellROX* signal over 5 min in the absence of dipyridyl (comparison in **Figure 3.3c**). The most likely oxidizing species in both cases is •OH.

The EZRDM growth medium contains 10 μM Fe^{2+} in the form of $FeSO_4$ salt, which might quickly enter the cytoplasm after permeabilization of the cytoplasmic membrane by CM15 and drive Fenton chemistry. To test this possibility, we plated cells, washed them in simple phosphate-buffered saline solution (PBS) to remove external iron, and then flowed in CM15 at 10 μM with CellROX at 2.5 μM, also in PBS. We observed a strong burst of CellROX* fluorescence immediately after cell shrinkage, with similar time dependence as in EZRDM (Appendix 3F).

Presumably the attenuation of CellROX* fluorescence by dipyridyl is due to chelation of internal free iron. These results are consistent with the hypothesis that CM15 induces formation of both O_2^- and •OH, each leading to about half of the peak CellROX* fluorescence intensity.

This qualitative result does not imply that the peak concentrations of O_2^- and •OH are similar. Numerous competitive kinetic factors influence the amount of CellROX* signal generated by O_2^- vs •OH.

Effects of cyanide and azide pre-treatment in aerobic conditions

Cyanide (added as KCN) and azide (NaN_3) are known to inhibit heme-containing enzymes. In *E. coli*, these include the catalases, the peroxidases, and the terminal cytochrome oxidase complex, but not NADH dehydrogenase I and II (NDH-I and NDH-II) or the ubiquinones of the electron transport chain. [21] In aerobic conditions, cytochrome oxidase carries out the four-electron transfer step converting O_2 to H_2O, simultaneously pumping protons across the CM to generate part of the proton-motive force (PMF).[17] Treatment of cells with either azide or cyanide degrades the PMF by inhibiting binding of O_2 to the catalytic site of cytochrome oxidase.

We pre-treated plated K12 cells with 15 mM NaN_3 in EZRDM for 5 min, after which we initiated flow of medium containing CM15 at 10 μM plus CellROX at 2.5 μM. A small CellROX* signal begins to rise within 12 s of cell shrinkage, reaching a plateau that is 4-fold smaller on average than for untreated cells (**Figure 3.3d**). We also flowed NaN_3 plus CellROX (no CM15) over plated cells growing aerobically. We observed a very small CellROX* signal about half the magnitude of that induced by CM15 action on cells pre-treated with azide (8-fold smaller than that induced by CM15 in untreated cells, **Figure 3.3d**). Similar results were observed for pre-treatment with 1 mM KCN for 5 min followed by CM15 (**Figure 3.3d**). Evidently inhibition of aerobic respiration by pre-treatment with azide or cyanide interferes with the mechanism by which CM15 induces CellROX* formation. In addition, inhibition of respiration by azide alone (no CM15) produces very little CellROX*.

"Freezing" of motion of DNA loci and of RNA polymerase by CM15 treatment

In a final set of observations, we found that CM15 treatment in aerobic conditions quickly freezes the local jiggling motion of fluorescently labeled chromosomal loci (Movie S4). Details are provided in SI and Appendix 3H. Pre-treatment with dipyridyl followed by CM15 also promptly froze DNA motion, suggesting the effect is not due to •OH radicals from Fenton chemistry. Treatment with NaN_3 alone did not alter the jiggling motion. In addition, CM15 treatment also strongly attenuated the normal jiggling/diffusive searching movement of RNA polymerase (Movie S5).[22] These results suggest that CM15 induces DNA damage. We speculate that the mechanism may involve inter-strand crosslinking of DNA with itself and protein-DNA crosslinking.

DISCUSSION

The initial inward movement of periplasmic GFP caused by the short, cationic antimicrobial peptide CM15 contrasts sharply with the effects of the longer cationic, helical antimicrobial peptides LL-37 [10] and cecropin A.[13b] For those AMPs, the first observed effect was permeabilization of the OM to GFP, resulting in complete loss of GFP fluorescence. Several minutes later, the CM was permeabilized, as evidenced by entry into the cytoplasm of the DNA-staining dye Sytox Green. Facile translocation across the OM of *E. coli* by short cationic peptides may prove fairly general.

Taken together, the new time-resolved data provide very strong evidence that in aerobic growth conditions CM15 induces a burst of reactive oxygen species in the *E. coli* cytoplasm. Three independent fluorescence signals indicate the abrupt onset of oxidative stress within 30 s of the cell shrinkage event: enhancement of cellular autofluorescence (**Figure 3.2b**), a burst of CellROX* fluorescence (**Figure 3.3a**), and a burst of resorufin fluorescence from the Amplex

Red/APEX2 assay (**Figure 3.4**). Studies *in vitro* show that CellROX Green detects both O_2^- and •OH, but does not detect H_2O_2 or the iron within SOD or HRP (Appendix 3B). The two-fold attenuation of CellROX* fluorescence by the iron chelator 2,2'-dipyridyl (**Figure 3.3c**, **d**) implicates free Fe^{2+} and suggests appreciable formation of both O_2^- and •OH, the latter presumably from Fenton chemistry. The Amplex Red/APEX2 assay detects H_2O_2 by a specific enzymatic reaction. In anaerobic growth conditions, the CellROX* fluorescence is attenuated five-fold (**Figure 3.3b, d**), the resorufin fluorescence is attenuated at least 50-fold (**Figure 4b**), and the MIC increases by a factor of 20. The anaerobic data confirm oxygen as an underlying effector of the strong signals in aerobic conditions, corroborate involvement of reactive oxygen species (ROS), and demonstrate that aerobic conditions greatly enhance the growth-halting effects of CM15.

Drawing on previous studies of ROS formation and control mechanisms in *E. coli*,[17] we can infer some features of the underlying mechanism by which CM15 induces ROS and rule out some possibilities. First, normally functioning members of the aerobic respiratory chain are not oxidizing CellROX directly to produce the burst of CellROX* fluorescence. On addition of CellROX alone (without CM15), only a moderate amplitude CellROX* signal rises slowly over tens of minutes (**Figure 3.3a**). This may be due to oxidation of CellROX by the normal, background levels of O_2^- or •OH or by other ambient oxidants.

In *E. coli* respiring aerobically, an important source of O_2^- and H_2O_2 is "autoxidation". That is the accidental scavenging of an electron by O_2, typically from reduced flavins in the cytoplasm or from reduced flavin cofactors in the membrane-bound respiratory chain.[17] The concentrations of ROS are kept low by superoxide dismutases (SODs, which convert O_2^- to H_2O_2) and catalases (which convert H_2O_2 to H_2O).

The smaller CM15-induced CellROX* signal after pre-treatment of cells with azide or cyanide implies that proper respiration is essential for most of the strong CM15-induced CellROX* fluorescence burst in aerobically growing cells. However, simple disruption of the flow of electrons through the respiratory chain and degradation of the proton-motive force by CM15 does not explain the burst of CellROX* fluorescence. If it did, we would expect treatment with azide or cyanide alone, which blocks respiration, to yield similar CellROX* fluorescence as treatment with CM15. Instead, it is eightfold smaller.

CM15 interaction with the aerobic respiratory electron transport chain itself is appealing, because the chain is membrane-bound. We know that CM15 strongly disrupts the cytoplasmic membrane, even to the point of permeabilization to periplasmic GFP. CM15 might interact with NDH-I, NDH-II, the respiratory ubiquinones (**Figure 3.5**), or soluble, cytoplasmic flavins in a way that enhances the rate of autoxidation.

However, the attenuation of CM15-induced CellROX* fluorescence after pre-treatment with cyanide or azide tends to rule out enhanced autoxidation as the main source of ROS under treatment with CM15 alone. Both cyanide and azide block the initial O_2 binding site within cytochrome oxidase (**Figure 3.5**), causing electrons to "pile up" in the respiratory electron transport chain.[23] NADH concentration increases, which in turn leads to larger concentrations of reduced flavins. Two of many documented examples are the flavin co-factor within the NDH-II complex (which is reduced by reaction with NADH) and free FAD (which is reduced by electron transfer from NADH catalyzed by flavin reductase). Imlay has shown that cyanide treatment leads to enhanced autoxidation of such reduced flavins, increasing the flux of O_2^- and H_2O_2.[17] Pre-treatment of cells with azide or cyanide should enhance the concentrations of these reduced flavins prior to the CM15 attack. If CM15 were further enhancing autoxidation of the reduced

flavins, we would expect a larger burst of CellROX* fluorescence from the pre-treated cells. Instead, it is fourfold smaller. The same argument applies to autoxidation of the electron transport carrier ubiquinone (**Figure 3.5**). Pre-treatment with cyanide or azide should enhance the concentration of UQH_2, but CM15-induced production of CellROX* fluorescence is reduced.

As an alternative to enhancement of autoxidation, we suggest that CM15 may interact with cytochrome oxidase-*bo*$_3$ (**Figure 3.5**) to induce improper release of O_2^- from its initial binding site at the heme Fe^{2+} center. After all, transfer of one electron to form an Fe^{3+}–O–O^- complex is likely the first step in the four-electron reduction of O_2 to H_2O.[24] This hypothesis is consistent with the experimental fact that inhibition of O_2 binding to the heme by pre-treatment with cyanide or azide decreases the CM15-induced CellROX* signal. Furthermore, CM15 addition to cells respiring anaerobically in nitrate-supplemented EZRDM induced a CellROX* signal 12 times smaller than that in aerobic conditions (**Figure 3.3d**). The anaerobic chain uses the same NDH-I and NDH-II complexes as the aerobic chain and has similar electron carrier species (menaquinone instead of ubiquinone). The main difference is the terminal complex, which is nitrate reductase instead of cytochrome oxidase-*bo*$_3$.[19]

There is additional, indirect evidence supporting this hypothesis.[25] A synthetic heme species was designed to mimic the catalytic function of cytochrome-*c* oxidase, the mitochondrial cytochrome oxidase, which is homologous to *E. coli* cytochrome-*bo*$_3$ complex. Proper coordination of the iron-porphyrin complex with a nearby copper center (mimicking Cu_B) and with a phenol group (mimicking Tyr^{244}) were essential to minimize release of partially reduced oxygen species, detected electrochemically as H_2O_2. Similarly, we suggest that CM15 perturbs cytochrome oxidase-*bo*$_3$, either by direct binding or indirectly by disrupting the local membrane

structure, in a way that facilitates release of O_2^- from the complex. Future biochemical studies on mutant strains and on inverted *E. coli* membranes will provide greater mechanistic insight.

Preliminary data suggest that natural antimicrobial peptides also induce oxidative stress in aerobically growing *E. coli*. Both the α-helical human cathelicidin LL-37 (37 aa, +7 net charge) and the α-helical cecropin A (37 aa, +7 net charge) cause an abrupt increase in CellROX* fluorescence at the time of cell shrinkage, much like CM15 did. It seems plausible that the degree of oxygenation in different local environments might act to modulate AMP efficacy, attenuating killing of *E. coli* in the gut but enabling killing in more aerobic environments. This was suggested earlier for defensins.[26]

There is other recent evidence of oxidative damage by antimicrobial peptides, antimicrobial proteins, and even by standard small-molecule antibiotics. Expression of LL-37 from a plasmid in the *E. coli* cytoplasm led to enhanced fluorescence from the ROS reporter dye DCFH-DA, detected on a two-hour timescale.[27] In both *Bacillus subtilis* and *E. coli*, the natural antibacterial agent peptidoglycan recognition protein (PGRP) enhanced fluorescence of the •OH reporter dye HPF, detected on a one-hour timescale.[28] In *B. subtilis*, treatment with the synthetic peptide MP196 was shown to dislodge the electron carrier protein cytochrome-*c* (which plays the role of the *E.coli* ubiquinones) from the cytoplasmic membrane.[4] Oxidative damage has also been inferred after treatment of bacteria with common bactericidal antibiotics,[5, 29] although this result has been controversial.[6]

In summary, single-cell observations using permeable, oxidation-sensitive dyes provide a sensitive and selective means of measuring ROS formation in live bacterial cells with sub-minute time resolution. This enables correlation of the onset of ROS with other cellular events in real time. Previously developed assays carried out on bulk cultures lack such spatiotemporal

resolution. In future work, we will apply these methods to a variety of AMPs and extend the scope to Gram positive species as well.

ACKNOWLEDGMENTS

This work was supported by the National Institutes of Health (NIGMS, R01-GM094510 to JCW and R01-GM093265 to JCW and Samuel H. Gellman). We thank Prof. Jimmy Feix (Wisconsin College of Medicine) for providing CM15 samples and Dr. Piercen Oliver of the Weibel lab for guidance in construction of the microfluidic device. Profs. Tricia Kiley (UW-Madison Department of Bacteriology) and James Imlay (UIUC Department of Microbiology) were tremendously helpful in discussions of oxidative stress mechanisms.

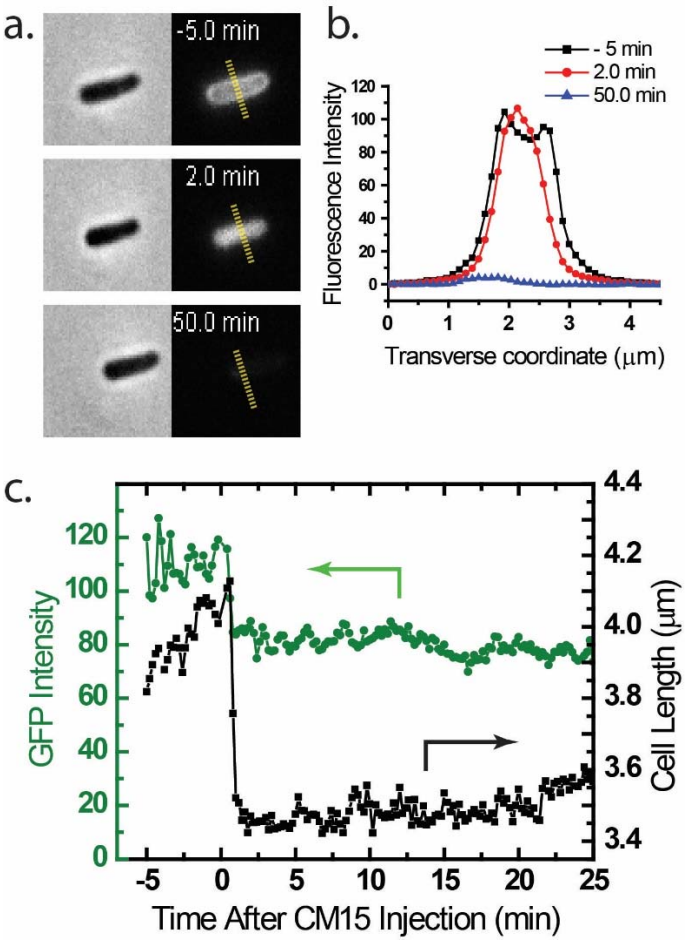

Figure 3.1 Effects of 10 μM CM15 (twice the 6-hr MIC) on MG1655 *E. coli* expressing periplasmic GFP. (a) Phase contrast and GFP fluorescence images of the same cell 5 min before, 2 min after, and 50 min after the onset of CM15 injection. (b) Transverse intensity linescans along the yellow hashed lines of panel (a), showing periplasmic (–5 min), cytoplasmic (+2 min), and essentially absent (+50 min) GFP spatial distributions. (c) Single-cell time dependence of cell length (from phase contrast images) and total GFP fluorescence intensity before and after injection of 10 μM CM15. Cell length and GFP intensity decrease abruptly and simultaneously as GFP enters the cytoplasm. The decrease in GFP intensity is presumably due to the higher pH in the cytoplasm.[13a]

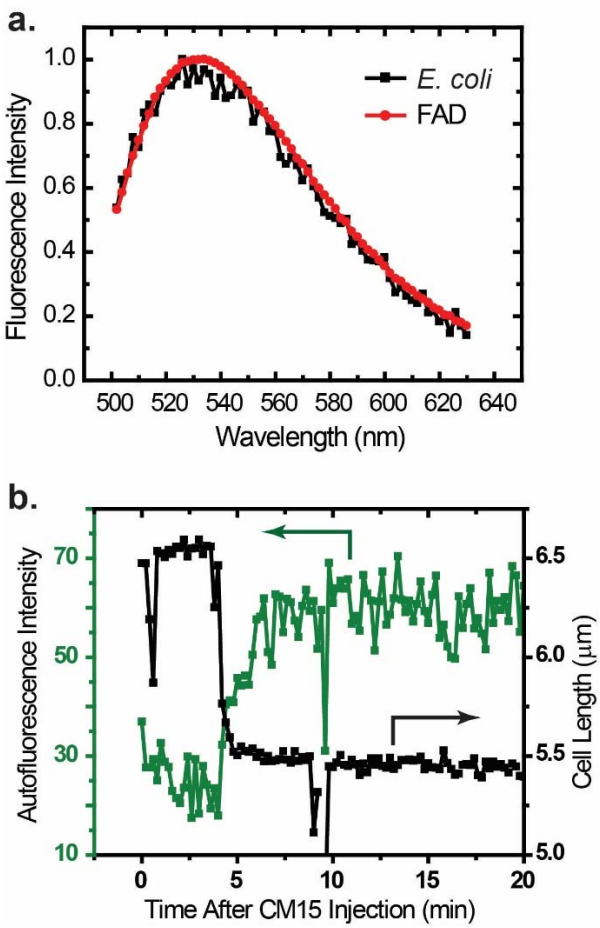

Figure 3.2 (a) Comparison of emission spectra excited at 457 nm for an *E. coli* cell culture grown at 30°C to OD_{600} ~ 0.4 and a solution of 100 μM FAD. (b) Single-cell time dependence of cell length (from phase contrast images) and total autofluorescence (excited at 457 nm) before and after injection of 10 μM CM15.

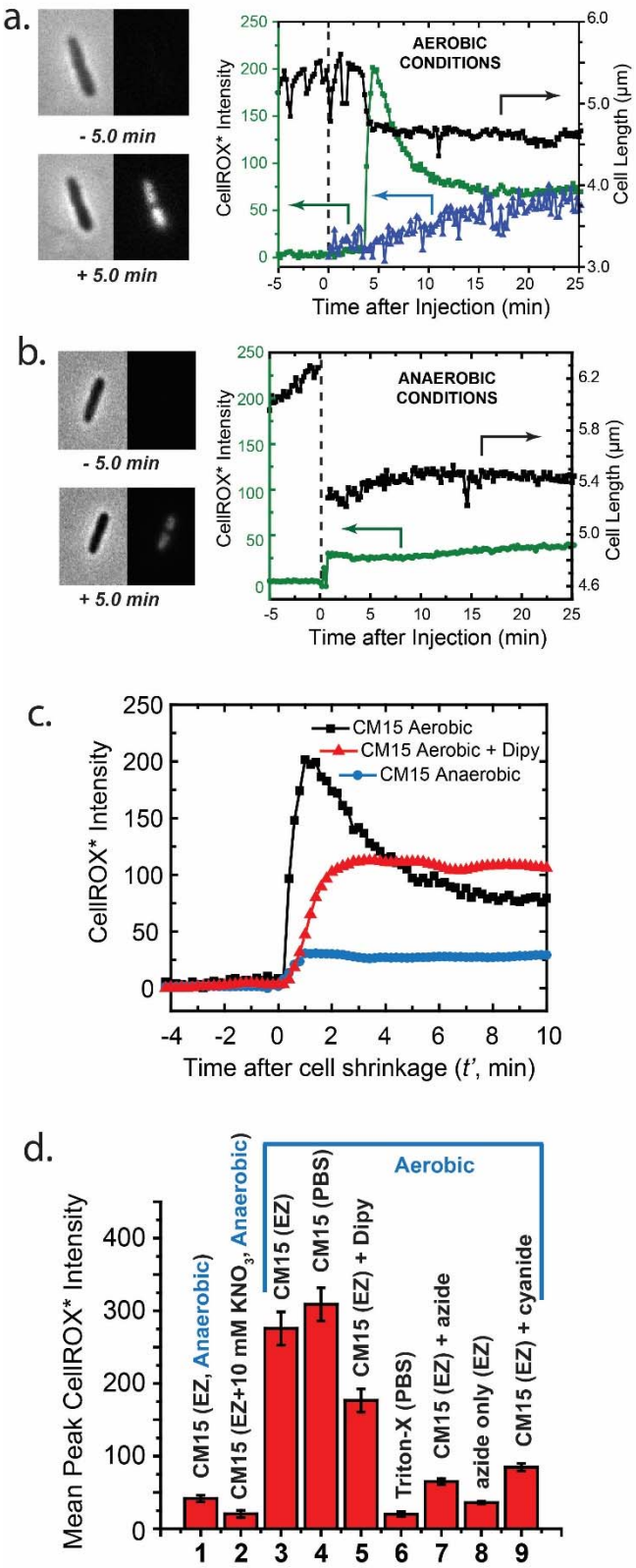

See next page for the figure legend.

Figure 3.3 CellROX* fluorescence and cell length measurements on addition of 10 μM CM15 in various conditions. (a) Aerobic growth conditions. *Left:* Phase contrast and green fluorescence images before and after CM15 addition at $t = 0$. *Right:* Time dependence of cell length (black) and total CellROX* fluorescence intensity (green) for the same cell. Blue data show CellROX* intensity vs time for a different cell for which CellROX* alone (no CM15) flowed beginning at $t = 0$. (b) Anaerobic growth conditions. *Left:* Phase contrast and green fluorescence images before and after CM15 addition at $t = 0$. *Right:* Time dependence of cell length and total CellROX* fluorescence intensity.

(c) Comparison of representative single-cell CellROX* fluorescence intensity traces after CM15 addition in aerobic conditions, in aerobic conditions with addition of 2,2'-dipyridyl (iron chelating agent), and in anaerobic conditions. (d) Bar graph of mean, single-cell CellROX* peak fluorescence intensity in nine different sets of experimental conditions. Error bars are ±1 standard deviation of the mean in each condition. **1** and **2**: Anaerobic conditions. CM15 addition to cells in standard EZRDM medium and in EZRDM supplemented with 10 mM KNO_3, respectively. **3-9:** Aerobic conditions as follows. **3:** CM15 addition to cells growing in EZRDM. **4:** CM15 addition after rinsing cells with PBS to remove external iron. **5**: CM15 addition in EZRDM to cells pre-treated with 2,2'-dipyridyl to chelate free cytoplasmic iron. **6:** No CM15; addition of 2% Triton-X in PBS. **7:** CM15 addition to cells pre-treated with 15 mM azide (NaN_3). **8**: No CM15. Addition of 15 mM azide alone to cells growing in EZRDM. **9**: CM15 addition to cells pre-treated with 1 mM cyanide (NaCN). See text for additional details.

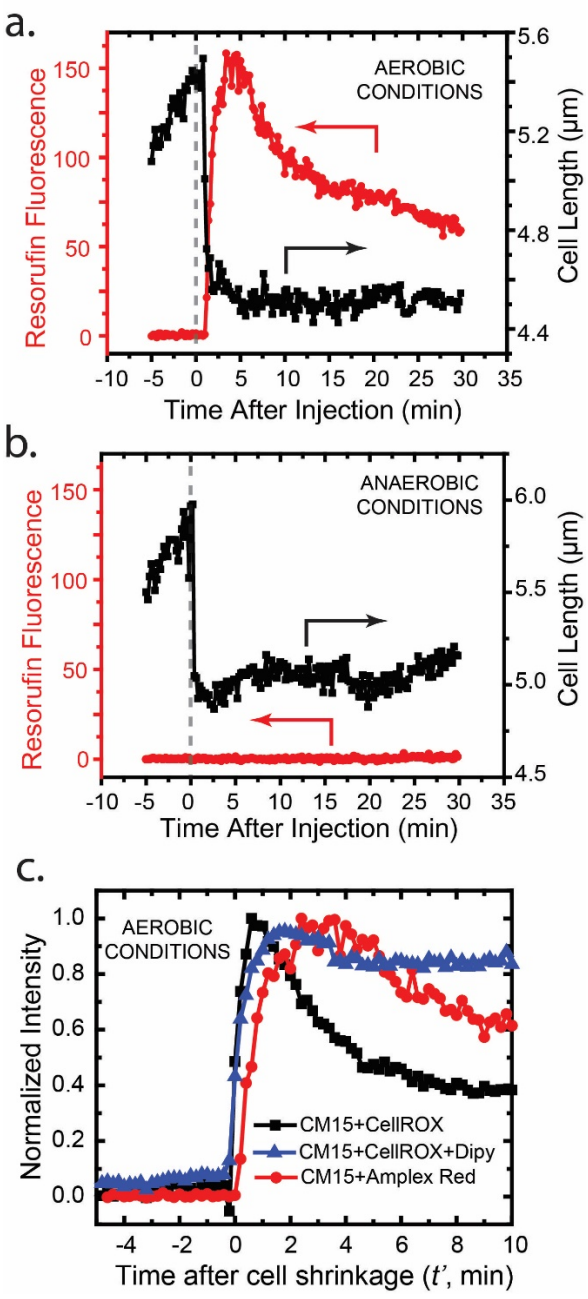

See next page for the figure legend.

Figure 3.4 Single-cell detection of H_2O_2 production following CM15 addition to cells expressing the non-native peroxidase APEX2 from a plasmid. a) Aerobic growth conditions. Single-cell measurement of resorufin fluorescence vs time after addition of 10 μM CM15 at $t = 0$. Signal begins to rise within 12 s of cell shrinkage event. (b) Same as panel (a), but for growth in anaerobic conditions. (c) Comparison of rising edge of CellROX* signal (with and without 2,2'-dipyridyl) and of resorufin signal after 10 μM CM15 treatment. Each trace is an average of five experiments, and the traces are normalized to the same peak intensity to facilitate comparisons. Time $t' = 0$ is the moment of cell shrinkage, used to place all cells on a common time axis.

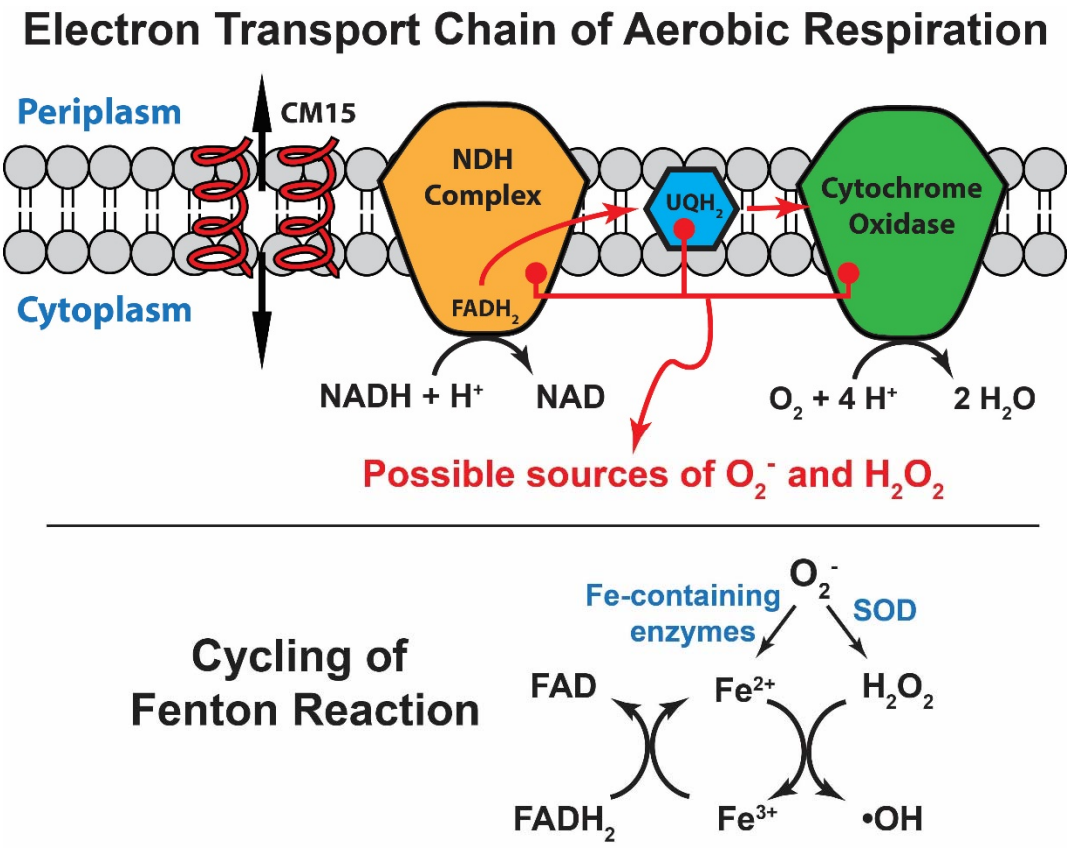

Figure 3.5 *Top:* Schematic of the aerobic respiratory electron transport chain in *E. coli*. Red arrows depict flow of electrons; black arrows depict chemical reactions. The NDH complex transfers electrons from NADH to ubiquinone (UQ) to form UQH_2. UQH_2 carries electrons to the terminal cytochrome oxidase-*bo*$_3$, which converts O_2 to H_2O in a four-electron reduction process. Helices depict CM15, which permeabilizes the cytoplasmic membrane seconds before the onset of oxidative stress. We suggest that CM15 induces premature release of O_2^- from cytochrome oxidase-*bo*$_3$. The data argue against a mechanism of enhanced autoxidation of the reduced flavin co-factor within NDH or of UQH_2. *Bottom:* A burst of O_2^- enhances free Fe^{2+} by attacking Fe-containing enzymes and enhances H_2O_2 by the action of superoxide dismutase. This leads to cycling of the Fenton reaction, resulting in enhanced autofluorescence from oxidized flavin species (FAD) and further oxidation of CellROX Green.

Appendix

Bacterial strains, growth conditions, and materials

The background strain is MG1655 in all cases (doubling time 50 min in EZRDM at 30°C). For experiments on periplasmic GFP, TorA-GFP was expressed from a plasmid pJW1 as previously described.[7] The bulk doubling time is 51 min. APEX2 was amplified with CGTA**GAATTC**ATGGACTACAAGGA TGACGAC and CGTA**GGATCC**TTAGTCCAGGGTCAGGCG and inserted into a pASK-IBA3plus vector using EcoRI and BamHI, yielding strain ZY01 (doubling time 53 min). APEX2 was expressed using tetracycline in same manner as TorA-GFP. The strain with *parS*-ParB-GFP labeling of the DNA locus called "Right2" was received from Boccard lab (doubling time 47 min).[8]

Bulk cultures were grown in EZ rich defined medium (EZRDM),[9] which contains a MOPS-buffered solution with supplemented metal ions (M2130; Teknova), glucose (2 mg/mL), supplemental amino acids and vitamins (M2104; Teknova), nitrogenous bases (M2103; Teknova), 1.32 mM K_2HPO_4, and 76 mM NaCl. Cultures were grown from glycerol frozen stock to stationary phase overnight at 30°C. Subcultures were grown to exponential phase (OD = 0.2-0.6 at 600 nm) before sampling for the microscopy experiments at 30°C, unless otherwise specified.

CM15 is a hybrid of the N-terminus of cecropin A and the N-terminus of melittin, designed to maximize antimicrobial action while minimizing hemolysis of eukaryotic cells.[30] We received *L*-CM15 with C-terminal amidation from Dr. Jimmy Feix (Wisconsin Medical College). The sequence is: KWKLFKKIGAVLKVL-NH_2. The net charge is +5 at neutral pH. The oxidation sensitive dye CellROX Green (Stock Item No. C10444) was purchased from Invitrogen. Flavin adenine dinucleotide (FAD) (F6625), protocatechuic acid (PCA) (37580),

protocatechuate 3,4-dioxygenase (PCD) (P8279), 2,2'-dipyridyl (D216305), superoxide dismutase (S5639), xanthine (X0626), and xanthine oxidase (X1875) were purchased from Sigma Aldrich. Amplex Red was purchased from Invitrogen (A22188).

MIC measurements in aerobic and anaerobic conditions

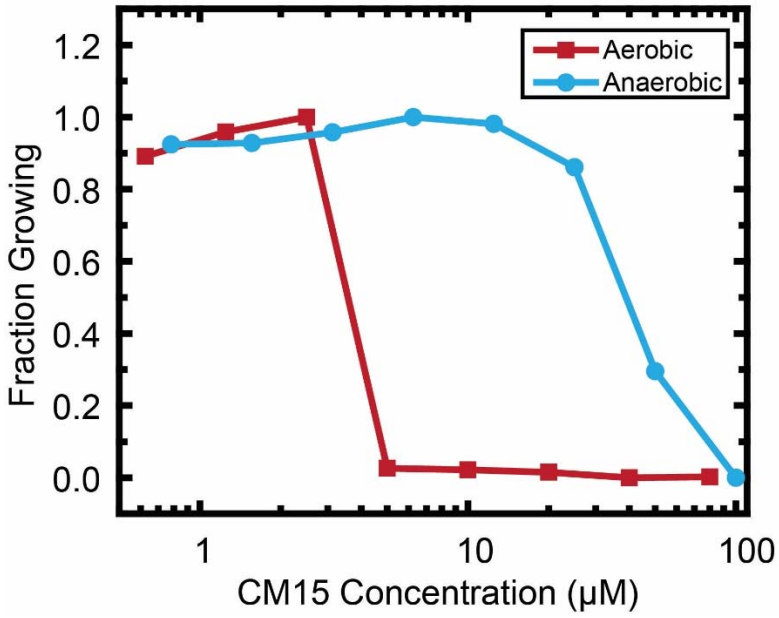

Appendix 3A. Bulk minimum inhibitory concentration (MIC) assay was performed for CM15 on K12 *E. coli* at 30ºC in anaerobic (blue) and aerobic (red) conditions. Cell growth was measured by optical density (OD) in each well at the 6-hr time point. The data are plotted as *Fraction Growing* = (OD – minOD)/(maxOD – minOD) to enable direct comparison between aerobic and anaerobic conditions. Here OD is the measurement at a given CM15 concentration, minOD is the minimum OD obtained at large CM15 concentration, and maxOD is the maximum OD obtained at zero CM15 concentration. The MICs of CM15 in aerobic and anaerobic conditions were determined to be 5 μM and 100 μM, respectively.

In vitro tests of CellROX oxidation

The structure of CellROX Green is proprietary. CellROX Green oxidation was tested for the reactive oxygen species superoxide, hydroxyl radical, and hydrogen peroxide. The first test used a mixture buffered at pH = 7.8 and containing 50 mM K_2HPO_4, 100 μM EDTA, 50 mM xanthine, 2.5 μM CellROX, and 40 μg/mL λ DNA. To suppress possible Fenton chemistry, EDTA was added to chelate any iron contaminant in the solution. DNA was added so that oxidized CellROX* can bind to λ DNA and become fluoresce. The CellROX* fluorescence was measured in 96-well plate containing xanthine oxidase (XO, 0.05 unit/mL), superoxide dismutase (SOD, 10 unit/mL), or both. XO uses xanthine as a substrate to produce either hydrogen peroxide or superoxide, depending on the oxidation state of the flavin cofactor. As shown in Appendix 3B, XO alone produces a large CellROX* signal. This signal presumably results from superoxide, as the signal is fivefold smaller on inclusion of SOD. Neither SOD alone nor horseradish peroxidase (HRP) alone is able to oxidize CellROX Green. Evidently CellROX is not oxidized by heme Fe^{2+}. Hydrogen peroxide (1 mM) does not oxidize the dye. Instead, it evidently quenches the background fluorescence from the mixture.

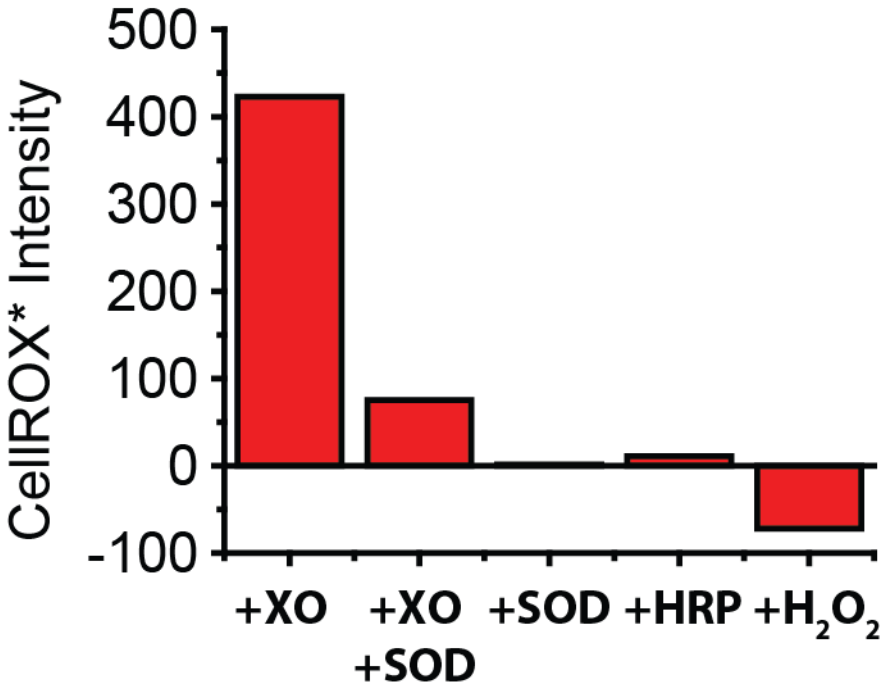

Appendix 3B. *In vitro* assay for CellROX* fluorescence in 96-well plate reader at 25°C. In all cases the buffered mixture contains 50 mM K_2HPO_4, 100 µM EDTA, 50 mM xanthine, 2.5 µM CellROX Green, and 40 µg/mL λ DNA. Each bar shows total CellROX* fluorescence on inclusion of the reagents shown, measured 5 min after mixing. All data are corrected by subtracting the 50 units of background fluorescence observed for the mixture alone. The concentrations of xanthine oxidase (XO) and superoxide dismutase (SOD) are 0.05 units/mL and 10 units/mL respectively. The concentrations of horseradish peroxidase (HRP) and hydrogen peroxide are 10 units/mL and 1 mM, respectively.

External addition of 10 μM H_2O_2 does not oxidize CellROX Green

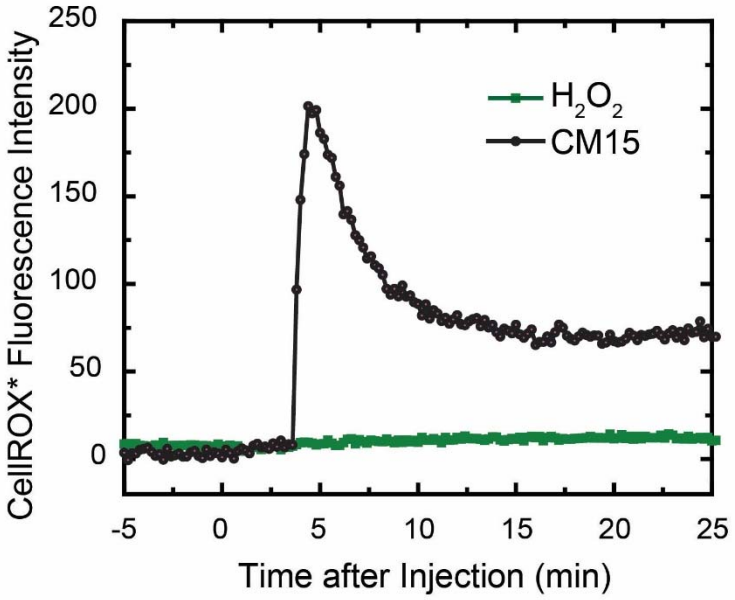

Appendix 3C. Single-cell CellROX* fluorescence intensity vs time after injection of 10 μM H_2O_2 plus CellROX Green (2.5 μM). CellROX* signal following CM15 addition in aerobic conditions was plotted as a comparison.

Permeabilization of cell membrane by Triton-X does not induce CellROX* fluorescence

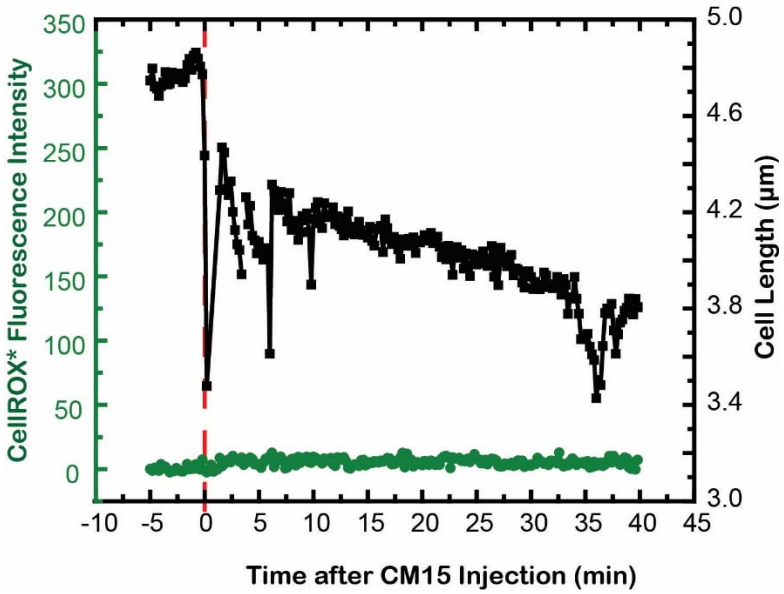

Appendix 3D. Single-cell length and total CellROX* fluorescence intensity vs time after injection of 2% Triton-X 100 plus CellROX Green at 2.5 µM. The detergent was dissolved in PBS. The dashed line indicates the time of injection.

CM15 effects in anaerobic conditions on cells expressing periplasmic GFP

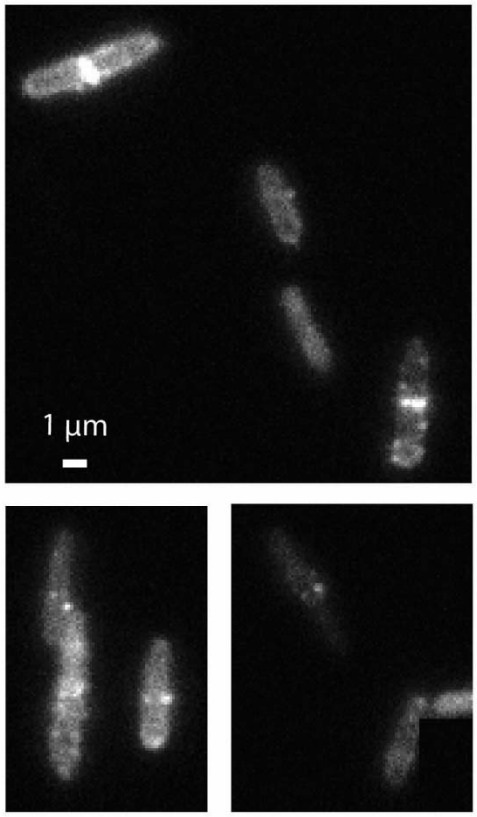

Appendix 3E. Heterogeneity of CM15 effects on *E. coli* expressing periplasmic GFP under anaerobic conditions. Images taken 1 min after abrupt cell shrinkage.

External Fe^{2+} is not involved in CellROX* formation by CM15

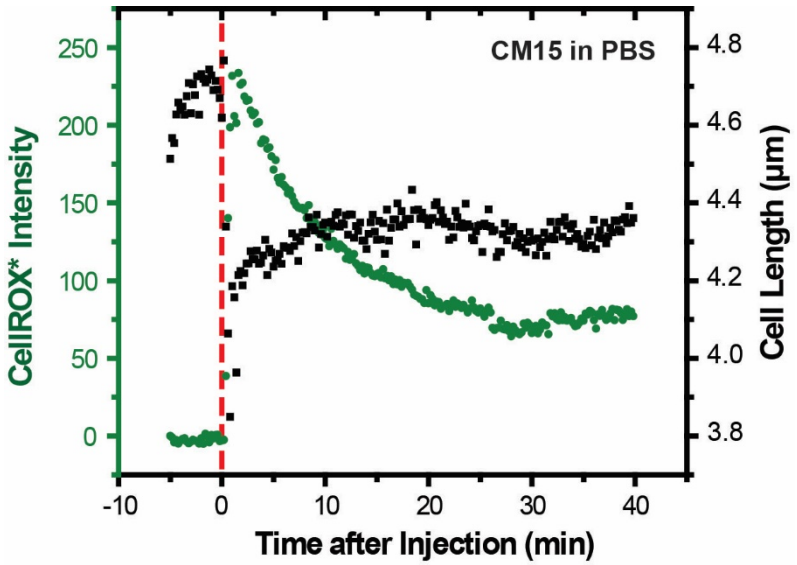

Appendix 3F. Single-cell length vs time and CellROX* fluorescence intensity vs time after injection of 10 µM CM15 with CellROX Green at 2.5 µM in PBS. The dashed line indicates the time of injection.

Oxygen scavenging substrate PCA alone does not affect growth or quench CellROX* fluorescence

Separate tests showed that the protocatechuic acid/protocatechuate 3,4-dioxygenase (PCA /PCD) additive that removes O_2 did not perturb cell growth in anaerobic conditions. PCA is itself a permeable antioxidant that scavenges free radicals. It seemed possible that in our anaerobic conditions, PCA (rather than the absence of O_2) was preventing oxidation of CellROX on addition of CM15. In aerobic conditions, we tested the effects of PCA by itself (without the enzyme PCD) on the CellROX response to CM15. In fact, PCA *enhanced* the peak amplitude of the CellROX fluorescence burst by about a factor of two and also slowed its decay time by about a factor of two (Appendix 3H). If further oxidation of the fluorescent form CellROX* causes the decay of fluorescence, then PCA may partially protect the CellROX*.

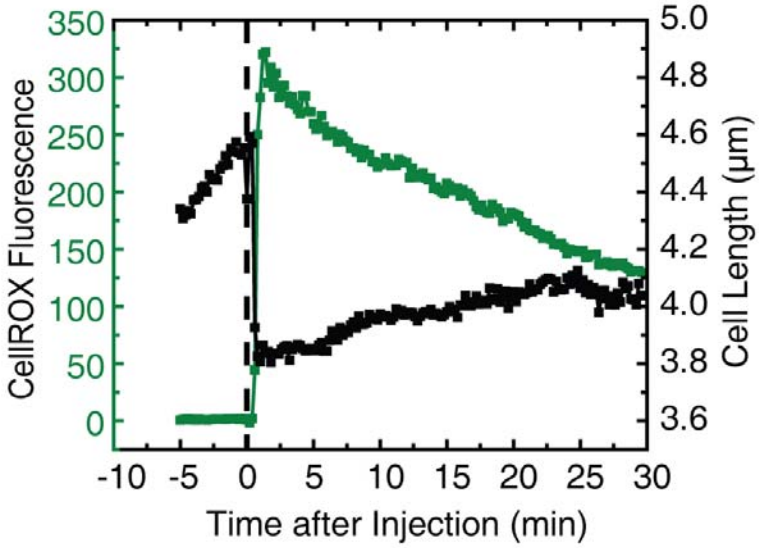

Appendex 3G. Single MG1655 cell length and CellROX Green fluorescence vs time after injection of 10 µM CM15, 2.5 µM CellROX Green and 5 mM PCA.

Assay for jiggling of DNA locus and diffusive motion of RNA polymerase

We monitored the movement of the chromosomal locus Right2 fluorescently labeled by a *parS*–ParB-GFP construct and of RNA polymerase (RNAP) labeled by expression of β'-YFP from the chromosome. In normal conditions, the Right2 locus exhibits sub-diffusive motion (jiggling in place). Within 12 s of cell shrinkage by CM15, the jiggling motion as judged by eye halted completely (Movie S4). When CM15 was added to cells pre-treated with 2,2'-dipyridyl (chelating Fe^{2+} and preventing Fenton chemistry), abrupt halting of Right2 jiggling again occurred. Treatment of cells with NaN_3 alone (no CM15) did not halt Right2 jiggling.

We quantify the relative motion of two foci as the mean-square displacement of the distance between them at fixed lag time τ = 1 frame = 12 s:

$$\delta r_{rel}^2(t) = |\boldsymbol{r}_1(t+\tau) - \boldsymbol{r}_2(t+\tau) + \boldsymbol{r}_1(t) - \boldsymbol{r}_2(t)|^2 \qquad \text{(S1)}$$

Here $\boldsymbol{r}_1$ and $\boldsymbol{r}_2$ are position vectors of two foci within the same cell at times *t* and *t* + τ. We prefer this relative squared displacement over a single-particle measure of displacement because the entire microfluidics chamber abruptly moves several microns relative to the camera on injection of CM15. The two-particle quantity $\delta r_{rel}^2(\tau)$ is fairly insensitive to this motion. Plots of $\delta r_{rel}^2(t)$ for normal cells and for cells before and after CM15 treatment are provided in Appendix 3H.

Normal RNAP motion on the 12-s timescale is heterogeneous. Copies searching for transcription initiation sites undergo fast diffusion (non-specific binding plus 3D "hopping" between DNA strands) while copies actively transcribing jiggle in place. Shortly after cell shrinkage induced by CM15, RNAP motion halts essentially completely (Movie S5).

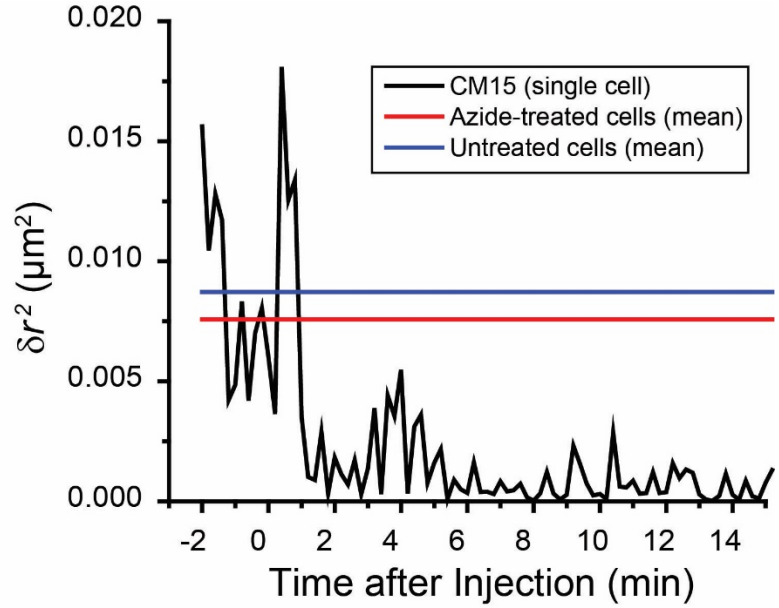

Appendix 3H. Plot of δr^2 between two particles vs time after injection of 10 μM CM15. The average δr^2 for several untreated cells (blue line) and for several cells treated with azide alone (red line) are shown for comparison.

REFERENCES

1. Wimley, W. C.; Hristova, K., Antimicrobial peptides: successes, challenges and unanswered questions. *J Membr Biol* **2011,** *239* (1-2), 27-34.

2. (a) Brogden, K. A., Antimicrobial peptides: pore formers or metabolic inhibitors in bacteria? *Nat Rev Microbiol* **2005,** *3* (3), 238-50; (b) Hancock, R. E.; Sahl, H. G., New strategies and compounds for anti-infective treatment. *Curr Opin Microbiol* **2013,** *16* (5), 519-21.

3. Schlamadinger, D. E.; Wang, Y.; McCammon, J. A.; Kim, J. E., Spectroscopic and computational study of melittin, cecropin A, and the hybrid peptide CM15. *J Phys Chem B* **2012,** *116* (35), 10600-8.

4. Wenzel, M.; Chiriac, A. I.; Otto, A.; Zweytick, D.; May, C.; Schumacher, C.; Gust, R.; Albada, H. B.; Penkova, M.; Kramer, U.; Erdmann, R.; Metzler-Nolte, N.; Straus, S. K.; Bremer, E.; Becher, D.; Brotz-Oesterhelt, H.; Sahl, H. G.; Bandow, J. E., Small cationic antimicrobial peptides delocalize peripheral membrane proteins. *Proc Natl Acad Sci U S A* **2014,** *111* (14), E1409-18.

5. (a) Kohanski, M. A.; Dwyer, D. J.; Hayete, B.; Lawrence, C. A.; Collins, J. J., A common mechanism of cellular death induced by bactericidal antibiotics. *Cell* **2007,** *130* (5), 797-810; (b) Kohanski, M. A.; Dwyer, D. J.; Collins, J. J., How antibiotics kill bacteria: from targets to networks. *Nat Rev Microbiol* **2010,** *8* (6), 423-35; (c) Dwyer, D. J.; Belenky, P. A.; Yang, J. H.; MacDonald, I. C.; Martell, J. D.; Takahashi, N.; Chan, C. T.; Lobritz, M. A.; Braff, D.; Schwarz, E. G.; Ye, J. D.; Pati, M.; Vercruysse, M.; Ralifo, P. S.; Allison, K. R.; Khalil, A. S.; Ting, A. Y.; Walker, G. C.; Collins, J. J., Antibiotics induce redox-related physiological alterations as part of their lethality. *Proc Natl Acad Sci U S A* **2014,** *111* (20), E2100-9.

6. (a) Liu, Y.; Imlay, J. A., Cell Death from Antibiotics Without the Involvement of Reactive Oxygen Species. *Science* **2013,** *339* (6124), 1210-1213; (b) Keren, I.; Wu, Y.; Inocencio, J.; Mulcahy, L. R.; Lewis, K., Killing by bactericidal antibiotics does not depend on reactive oxygen species. *Science* **2013,** *339* (6124), 1213-6; (c) Ezraty, B.; Vergnes, A.; Banzhaf, M.; Duverger, Y.; Huguenot, A.; Brochado, A. R.; Su, S.-Y.; Espinosa, L.; Loiseau, L.; Py, B.; Typas, A.; Barras, F., Fe-S Cluster Biosynthesis Controls Uptake of Aminoglycosides in a ROS-Less Death Pathway. *Science* **2013,** *340* (6140), 1583-1587.

7. Sochacki, K. A.; Shkel, I. A.; Record, M. T.; Weisshaar, J. C., Protein diffusion in the periplasm of E. coli under osmotic stress. *Biophys J* **2011,** *100* (1), 22-31.

8. Thiel, A.; Valens, M.; Vallet-Gely, I.; Espeli, O.; Boccard, F., Long-Range Chromosome Organization in E. coli: A Site-Specific System Isolates the Ter Macrodomain. *Plos Genetics* **2012,** *8* (4), 564-575.

9. Neidhardt, F. C.; Bloch, P. L.; Smith, D. F., Culture medium for enterobacteria. *J Bacteriol* **1974,** *119* (3), 736-47.

10. Sochacki, K. A.; Barns, K. J.; Bucki, R.; Weisshaar, J. C., Real-time attack on single Escherichia coli cells by the human antimicrobial peptide LL-37. *Proc Natl Acad Sci U S A* **2011,** *108* (16), E77-81.

11. Aitken, C. E.; Marshall, R. A.; Puglisi, J. D., An oxygen scavenging system for improvement of dye stability in single-molecule fluorescence experiments. *Biophys. J.* **2008,** *94* (5), 1826-1835.

12. Park, S.; You, X. J.; Imlay, J. A., Substantial DNA damage from submicromolar intracellular hydrogen peroxide detected in Hpx(-) mutants of Escherichia coli. *Proceedings of the National Academy of Sciences of the United States of America* **2005,** *102* (26), 9317-9322.

13. (a) Barns, K. J.; Weisshaar, J. C., Real-time attack of LL-37 on single Bacillus subtilis cells. *Biochim Biophys Acta* **2013,** *1828* (6), 1511-20; (b) Rangarajan, N.; Bakshi, S.; Weisshaar, J. C., Localized permeabilization of E. coli membranes by the antimicrobial peptide Cecropin A. *Biochemistry* **2013,** *52* (38), 6584-94.

14. Sargent, F., The twin-arginine transport system: moving folded proteins across membranes. *Biochem Soc Trans* **2007,** *35* (Pt 5), 835-47.

15. Lu, H. P., Single-molecule enzymatic dynamics (vol 282, pg 1877, 1998). *Science* **1999,** *283* (5398), 35-35.

16. Technologies, L., CellROX product data sheet, available on request.

17. Imlay, J. A., The molecular mechanisms and physiological consequences of oxidative stress: lessons from a model bacterium. *Nat. Rev. Microbiol.* **2013,** *11* (7), 443-454.

18. Bakshi, S.; Siryaporn, A.; Goulian, M.; Weisshaar, J. C., Superresolution imaging of ribosomes and RNA polymerase in live Escherichia coli cells. *Mol Microbiol* **2012,** *85* (1), 21-38.

19. Unden, G.; Bongaerts, J., Alternative respiratory pathways of Escherichia coli: Energetics and transcriptional regulation in response to electron acceptors. *Biochimica Et Biophysica Acta-Bioenergetics* **1997,** *1320* (3), 217-234.

20. Hassett, D. J.; Imlay, J. A., Bactericidal antibiotics and oxidative stress: A radical proposal. *ACS chemical biology* **2007,** *2* (11), 708-710.

21. Woodmansee, A. N.; Imlay, J. A., A mechanism by which nitric oxide accelerates the rate of oxidative DNA damage in Escherichia coli. *Mol. Microbiol.* **2003,** *49* (1), 11-22.

22. Bakshi, S.; Dalrymple, R. M.; Li, W.; Choi, H.; Weisshaar, J. C., Partitioning of RNA polymerase activity in live Escherichia coli from analysis of single-molecule diffusive trajectories. *Biophys J* **2013,** *105* (12), 2676-86.

23. Messner, K. R.; Imlay, J. A., Mechanism of superoxide and hydrogen peroxide formation by fumarate reductase, succinate dehydrogenase, and aspartate oxidase. *Journal of Biological Chemistry* **2002,** *277* (45), 42563-42571.

24. Yoshikawa, S.; Muramoto, K.; Shinzawa-Itoh, K., Proton-Pumping Mechanism of Cytochrome c Oxidase. In *Annual Review of Biophysics, Vol 40*, Rees, D. C.; Dill, K. A.; Williamson, J. R., Eds. 2011; Vol. 40, pp 205-223.

25. Collman, J. P.; Devaraj, N. K.; Decreau, R. A.; Yang, Y.; Yan, Y.-L.; Ebina, W.; Eberspacher, T. A.; Chidsey, C. E. D., A cytochrome c oxidase model catalyzes oxygen to water reduction under rate-limiting electron flux. *Science* **2007,** *315* (5818), 1565-1568.

26. Schroeder, B. O.; Wu, Z.; Nuding, S.; Groscurth, S.; Marcinowski, M.; Beisner, J.; Buchner, J.; Schaller, M.; Stange, E. F.; Wehkamp, J., Reduction of disulphide bonds unmasks potent antimicrobial activity of human beta-defensin 1. *Nature* **2011,** *469* (7330), 419-23.

27. Liu, W.; Dong, S. L.; Xu, F.; Wang, X. Q.; Withers, T. R.; Yu, H. D.; Wang, X., Effect of intracellular expression of antimicrobial peptide LL-37 on growth of escherichia coli strain TOP10 under aerobic and anaerobic conditions. *Antimicrob Agents Chemother* **2013,** *57* (10), 4707-16.

28. Kashyap, D. R.; Rompca, A.; Gaballa, A.; Helmann, J. D.; Chan, J.; Chang, C. J.; Hozo, I.; Gupta, D.; Dziarski, R., Peptidoglycan recognition proteins kill bacteria by inducing oxidative, thiol, and metal stress. *PLoS Pathog* **2014,** *10* (7), e1004280.

29. Dwyer, D. J.; Kohanski, M. A.; Collins, J. J., Role of reactive oxygen species in antibiotic action and resistance. *Curr Opin Microbiol* **2009,** *12* (5), 482-9.

30. Andreu, D.; Ubach, J.; Boman, A.; Wahlin, B.; Wade, D.; Merrifield, R. B.; Boman, H. G., Shortened Cecropin-A Melittin Hybrids--Significant Size Reduction Retains Potent Antibiotic Activity *FEBS Lett.* **1992,** *296* (2), 190-194.

Chapter 4

Cationic Antimicrobial Peptides Cause Reactive Oxygen Species Formation in Live *E. coli* cells

Introduction

In nature, commensal microorganisms coexist in host organisms. The host, then, needs to modulate the activity of its defense system in a way that allows proliferation of these commensal bacteria but simultaneously enables rapid killing of pathogens upon their arrival. Evolutionary selection in turn pushed the commensal bacteria to develop resistance to such a defense system by means such as modifying the lipopolysaccharide (LPS) layer.[1] The host is also under the same selection pressure. One possible way for the host to develop such modulatory activity is by utilizing environmental cues to enhance or diminish antibacterial activity.

Evidence for such modulatory activity in the host defense system can be found among antimicrobial peptides (AMPs). AMPs are ribosomally synthesized short peptides (15-50 AA).[2] They are produced in granulocytes and are used as a first line of defense against microorganisms.[3] AMPs such as defensins and LL-37 are expressed in epithelial cells in the human gut, where commensal bacteria flourish. The population of commensal bacteria, however, needs to be controlled to avoid deleterious effects, as seen in Crohn's disease.[4] How, then, do organisms control the population level of commensal bacteria in the gut? One way to resolve this issue is to modulate the population based on environmental cues. In recent studies, the antimicrobial peptide human β-defensin 1 showed higher antimicrobial potency when all disulfide bonds are reduced.[5] As the human gut is generally a reducing environment, human β-defensin 1 may thus be more potent in the gut in comparison to in other regions. In our recent studies with artificial antimicrobial peptide CM15, we have shown that dissolved oxygen enhances the activity of CM15 by accelerating the formation of reactive oxygen species (ROS) in live *E. coli* cells.[6] The human gut is in an anaerobic condition. We hypothesized that the antimicrobial potency of many AMPs against opportunistic pathogens may be greater once they

penetrate the layer of epithelial cells in intestine, where cells are growing aerobically. The commensal bacteria in the gut, on the other hand, remain unharmed.

To test this hypothesis, we examined the ability to induce oxidative stress of three antimicrobial peptides: LL-37 (human cathelicidin-derived antimicrobial peptide), Melittin (bee venom), and Indolicidin (bovine antimicrobial peptide) (Table 1). Here, we show that the antimicrobial activity of LL-37 and Melittin on live *E. coli* cells is attenuated in anaerobic conditions. Indolicidin, on the other hand, did not show a significant difference in growth inhibition under anaerobic and aerobic conditions. In new mechanistic insights, we show that AMP accumulation in the periplasm may be the cause of accelerated ROS formation and that the formation of ROS requires active aerobic cellular respiration.

Materials and Methods

Bacterial strains, growth conditions, and materials

Most of the experimental details have been described in Chapter 3. The background strain is MG1655 in all cases. For experiments on periplasmic GFP, TorA-GFP was expressed from a plasmid pJW1 as previously described.[7] APEX2 was expressed using tetracycline in same manner as TorA-GFP.

Bulk cultures were grown in EZ rich defined medium (EZRDM),[8] which contains a MOPS-buffered solution with supplemented metal ions (M2130; Teknova), glucose (2 mg/mL), supplemental amino acids and vitamins (M2104; Teknova), nitrogenous bases (M2103; Teknova), 1.32 mM K_2HPO_4, and 76 mM NaCl. Cultures were grown from glycerol frozen stock to stationary phase overnight at 30°C. Subcultures were grown to exponential phase

(OD = 0.2-0.6 at 600 nm) before sampling for the microscopy experiments at 30°C, unless otherwise specified.

LL-37 (AS-61302) was purchased from Anaspec. Melittin (M2272) was purchased from Sigma-Aldrich. Indolicidin (AS-60999) was purchased from Anaspec. The oxidation sensitive dye CellROX Green (Stock Item No. C10444) and Amplex Red (A22188) was purchased from Invitrogen.

Minimum inhibitory concentration assay (MIC)

The MIC for CM15 was determined using a broth microdilution method as previously described.[9] Two-fold serial dilutions of LL-37, Melittin, and Indolicidin in 1X EZRDM were performed in separate rows of a polystyrene 96-well plate with each plate containing an inoculum of *E. coli* MG1655. The inoculum was a 1:20 dilution from a bulk culture at midlog phase (OD_{600} = 0.5) grown at 30°C. The plate was incubated at 30°C and shaken at 200 rpm in a Lab-Line Orbital Environ Shaker (Model 3527) for 6 hr for aerobic MIC measurements. The MIC values were taken as the lowest concentration for which no growth was discernible (<0.05 O.D) after 6 hr.

The anaerobic MIC was measured on a 96-well plate that was sealed with plastic wrap. Cells were incubated in EZRDM containing protocatechuic acid (PCA) at 10 mM and protocatechuate 3,4-dioxygenase (PCD) at 100 nM to scavenge oxygen.[10] The plate was incubated at 30°C for 6 hr, followed by OD measurements. The previous studies showed that there is no growth defects from oxygen scavenging protein or substrate.[6]

Microfluidics chamber for aerobic and anaerobic measurements

Imaging of individual cells was carried out at 30ºC in a simple microfluidics chamber consisting of a single rectilinear channel of uniform height of 50 μm and width of 6 mm, with a channel length of 11 mm. The total chamber volume is ~10 μL. The negative of the cell design was patterned onto a silicon wafer via photolithography and the wafer was silanized. Sylgard 184 silicone elastomer mixture (Dow Corning) was poured on to the patterned silicon wafer and baked for 24 hours in a 37°C incubator after removing air in a vacuum desiccator. The cured polydimethylsiloxane (PDMS) slab was removed and holes were punched for entry and exit hypodermic needles. The patterned PDMS slab was fused to a dried, acetone-cleaned, 22-mm x 40-mm glass coverslip pre-cleaned by plasma oxidation. Soon after the bonding of the two pieces, 0.01% poly-*L*-lysine (molecular weight >150,000 Da) was injected through the chamber for 30 min and rinsed thoroughly with millipore water. For imaging experiments, the chamber was maintained at 30°C with a TC-344B dual automatic temperature controller through the CC-28 cable assembly attached to RH-2 heater blocks (Warner Instruments).

The PDMS ceiling of the microfluidics device is permeable to the ambient gases N_2 and O_2. For anaerobic imaging experiments, we needed to prevent O_2 from entering the chamber through its ceiling. A small anaerobic chamber surrounding the microfluidics device was constructed of aluminum with a nitrogen gas inlet and outlet. Prior to injection of cells, nitrogen gas flowed through the chamber continuously for 1.5 hr. *E. coli* were grown in aerobic conditions until injected to the chamber. Fresh de-oxygenated EZRDM was made by treating EZRDM with 50 nM protocatechuate 3,4-dioxygenase (PCD) and 2.5 mM protocatechuic acid (PCA). This was used to wash the cells at 30°C prior to plating. De-oxygenated EZRDM then flowed across

the plated cells for 30 min prior to injection of CM15 and CellROX. The subsequent microscopy imaging experiment was carried out as before.

Microscopy

Single-cell imaging was performed on two different microscopes: a Nikon TE300 inverted microscope with a 100X, 1.3 NA phase contrast objective (Nikon) and Nikon Eclipse Ti inverted microscope with a 100X, 1.45 NA phase contrast objective (Nikon). For the Nikon TE300, images were further magnified 1.45X in a home-built magnification box. A line tunable Ar^+ laser (Melles Griot) at 488 nm or 457 nm was expanded to illuminate the field of view uniformly. Laser intensities at the sample were ~10 W/cm^2 at 457 nm and ~5 W/cm^2 at 488 nm. Fluorescence images were obtained with an EMCCD camera, either Andor iXon 897 or Andor iXon 887. In both cases, the pixel size corresponds to 110 ± 10 nm at the sample.

All emission filters were purchased from Chroma Technology. Specific emission filters were: HQ525/50 for observation of GFP or CellROX after 488-nm excitation and HQ617/70 for resorufin after 561-nm excitation.

Unless otherwise noted, time-lapse movies of 35-min total duration were obtained as 400 frames of 50-ms exposure time each, with fluorescence and phase contrast images interleaved at 6-s intervals (12 s per complete cycle). A movie begins immediately after adhesion of cells and the rinsing away of extra cells. The cells were imaged for ~5 min before injection of fresh medium containing the compounds under study.

CellROX Green oxidation assay

CellROX Green is a proprietary oxidation-sensitive dye whose fluorescence quantum yield at 500-550 nm after excitation at 488 nm increases dramatically on oxidation in the presence of

ds-DNA. It readily permeates both *E. coli* membranes. The manufacturer tested its sensitivity to different reactive oxygen species in the presence of ds-DNA *in vitro* including hydroxyl radical (•OH), superoxide (O_2^-), hydrogen peroxide (H_2O_2), peroxynitrite ($ONOO^-$), nitric oxide (NO), and hypochlorite (ClO^-). The only two oxidizing agents that significantly enhanced CellROX fluorescence were hydroxyl radical and superoxide. Importantly, hydrogen peroxide has no effect.

In the basic CellROX* imaging experiments, MG1655 cells were injected into the microfluidics chamber. After allowing 5 min for plating of cells, the bulk solution was washed away with fresh, pre-warmed, aerated EZRDM. After the wash, cells were grown for 5 min prior to the injection of 10 μM CM15 with 2.5 μM CellROX. CellROX fluorescence after 488 nm excitation was monitored through emission filter HQ525/50. The laser intensity at the sample was ~2.5 W/cm^2. We maintained the intensity, laser set-up, and camera for LL-37, Melittin, and Indolicidin experiments to allow quantitative comparison between peptides. To maintain good aeration and steady bulk concentrations, the medium with CM15 and CellROX flowed continuously at 0.3 mL/hr.

Amplex Red oxidation assay

We developed a single-cell, time-resolved measurement of H_2O_2 production following CM15 treatment. The assay is based on the well-established Amplex Red method. Some peroxidases (not the catalases naturally occurring in *E. coli*) catalyze reaction of the dye Amplex Red with H_2O_2 to form the fluorescent species resorufin (λ_{em} = 585 nm). To measure the rate of H_2O_2 production under normal metabolism, Imlay and co-workers[11] studied an HPX^- mutant strain of *E. coli* (lacking catalase). The permeable H_2O_2 escapes the cell and undergoes a bulk reaction with Amplex Red, catalyzed by horseradish peroxidase (HRP). The product is

resorufin, which absorbs at 570 nm and fluoresces strongly at 585 nm. The time resolution of this method was ~5 min. Recently Collins and co-workers[12] adapted the method to carry out the Amplex Red + H_2O_2 reaction inside the cytoplasm by inserting a plasmid that expresses the peroxidase APEX2 (mutated ascorbate peroxidase) within the cytoplasm. H_2O_2 was detected after it diffused out of the cell. The time resolution was ~60 min. Here we use the Collins adaptation with single-cell, time-resolved fluorescence detection in the microfluidics chamber. This enables sensitive detection of H_2O_2 production with 12-s time resolution and correlation of AMP-induced H_2O_2 production with other events in real time. We maintained the intensity, laser set-up, and camera for LL-37, Melittin, and Indolicidin experiments to allow quantitative comparison between peptides.

Results

Disruption of *E. coli* membrane by LL-37, Melittin, and Indolicidin

First we repeated the previously developed single-cell, time-lapse microscopy experiments to monitor the time-dependent disruption of membrane integrity of K12 *E. coli* MG1655 by the antimicrobial peptides LL-37, Melittin, and Indolicidin. This assay utilizes the modified K12 cells with a plasmid pJW1. The plasmid, pJW1, encodes a GFP with the twin-Arginine translocase signal peptide appended to the N-terminus of GFP. The signal peptide allows the cytoplasmic, folded GFP to export to the periplasm. The exported GFP, then, is freely diffusing in the periplasm.[13] As previously described, cells are plated in a microfluidics chamber and are growing in continuously refreshed medium. The cells exhibit a halo of green fluorescence upon the excitation at 488 nm, indicating a predominantly periplasmic spatial distribution of GFP. The three AMPs differ significantly in the sequence and timing of membrane permeabilization events.

At $t = 0$, we initiate flow of 4 μM LL-37 (1X 6-hr MIC, Table 2) in EZRDM medium through the microfluidics chamber. Because we previously observed the outer membrane (OM) permeabilization for LL-37, 5 nM of SYTOX green, an impermeable DNA dye that fluoresces upon binding to DNA, was added into the LL-37 solution. The sudden increase of SYTOX green signal with the chromosomal DNA pattern is used as a proxy for cytoplasmic membrane (CM) permeabilization. For ~90% cells in a typical field of 50 cells, the growth is attenuated within 10 minutes of the injection, as monitored by the cell length vs time (**Figure 4.1A**). The growth attenuation is likely caused by the accumulation of LL-37 in the periplasm, as shown in previous experiments with Rhodamine-labeled LL-37.[13b] For ~60% of the cells, we observed the sudden decrease in GFP signal and loss of a halo of green fluorescence within 35 min, indicating that the OM is permeabilized. The other ~40% of the cells exhibit an attenuated growth rate, yet are still elongating without the loss of periplasmic GFP. Presumably these cells have an intact outer membrane. For the ~60% of the cells that underwent OM permeabilization, SYTOX green signal increased within 5 min post-OM permeabilization, as evident by the chromosomal DNA distribution of the fluorescence from SYTOX green. This signal indicates CM permeabilization. The ~40% cells that are continuously growing did not display a sudden increase of SYTOX, indicating that both CM and OM are intact during this period.

We repeated the same assay with Melittin, without the use of SYTOX green because the initial CM permeabilization and the subsequent OM permeabilization occur nearly simultaneously. At $t = 0$, we initiate flow of 10 μM Melittin (2X 6-hr MIC, Table 2) in EZRDM medium through the microfluidics chamber as described above. For ~60% of the cells, the sudden loss of periplasmic GFP occurs within 1 min after the injection (**Figure 4.2B**). For ~40% of the cells, the observation occurs later than 1 min. The OM permeabilization occurs nearly

simultaneously with the cell shrinkage. Unlike LL-37, there is not complete loss of periplasmic GFP signal, possibly indicating that OM permeabilization is a transient event. Within 30 sec of the OM permeabilization, migration of GFP from the periplasm into the cytoplasm was observed. This nearly concurrent OM to CM permeabilization may be due to the rapid accumulation of Melittin on the CM upon OM permeabilization. After variable lag time, the complete loss of GFP was observed.

We repeated the same assay on the cells with Indolicidin. At $t = 0$, we initiate flow of 30 μM Indolicidin (the 6-hr MIC, Table 2) and monitor single cells. For >80% of the cells, the cell shrinkage was observed within 15 min of the injection (**Figure 4.2C**). Within 25 min of the injection, all the cells in the field of view have shrunk in length. The CM permeabilization was observed ~1 minute after the cell shrinkage, as evident by the movement of GFP into cytoplasm. No outer membrane permeabilization was ever observed for the duration of the movie (~1 hr).

Antimicrobial Activity of LL-37 and Melittin is Enhanced under Aerobic Condition

To test the efficacy toward K12 *E. coli* MG1655, we performed a minimum inhibitory concentration (MIC) assay under aerobic and anaerobic condition using the 96-well broth-dilution method previously described.[6] After 6-hr incubation, the MICs for CM15, LL-37, Melittin, and Indolicidin were measured and are summarized in Table 2. Strong enhancement of the growth inhibition was observed under the aerobic condition for CM15 (20X), LL-37 (4X), and Melittin (8X). However, there is no difference between aerobic and anaerobic growth inhibition for Indolicidin. To correlate the effects observed on bulk MICs with microscopy experiments, we performed the CellROX* and Amplex Red assays as previously described. At this writing, Melittin and LL-37 have been studied, but the Indolicidin work remains in progress.

Melittin Causes ROS upon Cytoplasmic Membrane Permeabilization

As previously described, Melittin shares common hydrophobic residues with CM15. Although the sequence of permeabilizations differs from CM15, Melittin showed both CM and OM permeabilization. We determined the time at which the reactive oxygen species (ROS) is formed during the treatment with Melittin. To observe the formation of ROS, we injected 10 μM Melittin (2.5X the aerobic MIC) with 2.5 μM of CellROX Green. CellROX Green is a profluorophore that can be oxidized by ROS such as superoxide (O_2^-) and hydroxyl radical (·OH). The oxidized CellROX (here, CellROX*) becomes fluorescent upon binding to DNA. Here, we plated aerobically grown K12 *E. coli* cells without the pJW1 plasmid. Upon excitation of 488 nm, the cells exhibit a low level of autofluorescence from flavin molecules such as riboflavin, FMN, and FAD. At $t = 0$, 10 μM Melittin with 2.5 μM of CellROX green is injected into aerobically grown K12 *E. coli* MG1655 cells. CellROX* fluorescence begins to rise immediately upon the cell shrinkage event (**Figure 4.2A**). The CellROX* intensity peaks ~1 min later. Over the next 5 min, the signal decreases toward a plateau value. All cells studied exhibited an abrupt burst of CellROX* fluorescence. The subsequent signal decrease is observed in ~70% of the cells under the Melittin treatment. Higher CellROX* peak intensity was observed for those cells that exhibit the decrease in signal, supporting the hypothesis that the fluorescent state CellROX* is being destroyed by subsequent oxidative damage. The time course of the event of CellROX* intensity vs time under Melittin treatment is reminiscent of that under CM15 treatment. The spatial distribution of CellROX* intensity is that of chromosomal DNA of *E. coli*, indicating that there is no major contribution from either non-specific binding of CellROX* or unoxidized CellROX. Similar events occurred in >100 cells observed for 40 min in four separate experiments.

To further confirm that the CellROX* signal is due to the formation of ROS, we added Melittin to cells grown anaerobically. Here, the plated, aerobically grown cells have adapted to anaerobic conditions for 30 min and are growing in continuously refreshed, oxygen-free EZRDM. On addition of 10 μM Melittin (2.5X aerobic MIC) along with 2.5 μM CellROX green in oxygen-free EZRDM, the cell shrinkage event was observed for 90% of the cells under the field of view. However, there was no significant increase in CellROX* intensity upon the shrinkage (**Figure 4.2C**), suggesting no ROS formation under the anaerobic condition. Approximately 10% of the cells in the field of view continuously grow under the Melittin treatment, supporting the hypothesis that oxygen is an important factor for growth attenuation for cells under Melittin treatment. The 8-fold lower MIC in aerobic condition (4 μM) compared to the MIC of anaerobic condition (32 μM) further supports that ROS-mediate cell growth attenuation.

To augment the CellROX* result, we monitored H_2O_2 production by Melittin via recently developed single-cell, time-resolved resorufin assay. This assay utilizes a mutated ascorbate peroxidase, APEX2, whose catalytic state upon reacting with H_2O_2 reacts with the non-fluorescent species Amplex Red to form the fluorescent species resorufin. Resorufin emission can be monitored by excitation of 561 nm. This mutated enzyme is necessary, as catalase and peroxidases inside *E. coli* cannot catalyze the reaction.

We repeated the flow experiment in aerobic conditions using the K12 *E. coli* expressing APEX2 under the inducible promoter. We allow ample time for APEX2 to fold properly in cytoplasm to ensure its catalytic activity. At $t = 0$, we flowed 10 μM of Melittin plus Amplex Red at 10 μM. A strong burst of resorufin signal occurred simultaneously with cell shrinkage. The signal gradually decreases, possibly because there is no specific binding target in the *E. coli*

cytoplasm or periplasm and resorufin is permeable (**Figure 4.2B**). This is further supported by the increase in background fluorescence from the surrounding medium over time. In anaerobic conditions, we see little if any resorufin fluorescence after cell shrinkage (**Figure 4.2D**). This phenomenon strongly reminisces the resorufin signal vs time under CM15 treatment (**Figure 4.5**).

LL-37 Induces ROS upon Accumulation in Periplasm

We repeated the same CellROX green assay under aerobic condition by flowing aerated EZRDM with 4 μM LL-37 (1X the aerobic MIC) and 2.5 μM CellROX Green. Gradual growth rate attenuation was observed for many cells upon injection of LL-37, as described above for the periplasmic GFP experiments. Interestingly, the CellROX* intensity gradually increases while the growth attenuation occurs (**Figure 4.3A**). Later on, a sudden decrease in CellROX* signal was observed, presumably at the moment of CM permeabilization. This is deduced based on the cell length change under phase contrast images. The CM permeabilization occurs immediately before the last step of shrinkage. We observed that the rate at which CellROX* intensity increases during growth rate attenuation correlates with a shorter lag time to OM and CM permeabilization. Evidently CM permeabilization is not a requirement for induction of ROS formation.

We initially hypothesized that growth rate attenuation in aerobic conditions prior to OM permeabilization under LL-37 treatment is due to rapid formation of ROS inside a cell. This was tested by repeating the same assay under anaerobic conditions as previously described. Interestingly, growth attenuation was still observed for all the cells under anaerobic conditions, indicating that the initial growth rate attenuation is not solely caused by oxygen concentration. The growth rate attenuation may be caused by LL-37 accumulation inside the periplasm, causing

osmotic imbalance. If so, then the CellROX* signal may indirectly show the amount of LL-37 that has accumulated inside the periplasm. Further study is required to fully understand this behavior. However, under anaerobic conditions, a significantly higher percentage of cells (~40% ($+O_2$) compared to ~80% ($-O_2$)) continue to grow, albeit at an attenuated rate. This indicates that the dissolved oxygen concentration may modulate the OM and CM permeabilization observed in the aerobic condition.

We tested for H_2O_2 induction by repeating the flow experiment in aerobic conditions using the K12 strain expressing APEX2. At $t = 0$, we flowed 4 μM of LL-37 plus Amplex Red at 10 μM. A small burst of resorufin fluorescence begins to rise once the CM permeabilization occurred, as evident by the last step of cell shrinkage (**Figure 4.3B**). The resorufin signal decreases after a few minutes. We suspect that this decrease is due to permeabilization of the outer membrane, leading to rapid escape of resorufin. In anaerobic condition, we observed a little to no resorufin fluorescence signal, indicating that the production of H_2O_2 is oxygen dependent (**Figure 4.3D**).

Discussion

We showed that LL-37, Melittin, and Indolicidin differ substantially in the sequence of membrane permeabilization events they induce in live *E. coli* cells. As mentioned earlier, the main focus of this Chapter 4 was to show whether oxygen plays a key role in modulating the antimicrobial activity of AMPs. Several tested AMPs (LL-37, Melittin, and CM15) have now been shown to exhibit oxygen-dependent growth inhibition of *E. coli* cells. However, it seems that not all AMPs display oxygen-dependent antimicrobial activity. For example, there was no difference in MICs under aerobic and anaerobic conditions for Indolicidin (Table 2). In addition, there is a different extent of oxygen-mediated killing by all these antimicrobial peptides, as

exemplified by the different factors of activity enhancement under aerobic condition in comparison to anaerobic conditions (Table 2).

What then is the key moment or phenomenon that needs to occur in order to induce oxygen-mediated growth inhibition under aerobic condition? We have previously established that the growth inhibition of CM15 is caused by reactive oxygen species (ROS) through real-time detection of O_2^-/·OH and H_2O_2 via CellROX* and resorufin signal in single *E. coli* cells.[6] For CM15, CM permeabilization coincides with the abrupt burst of CellROX* and resorufin signal (**Figure 4.5**). Based on several controls, we concluded that 1) cellular respiration through electron transport chain (ETC) is important for generation of ROS under CM15 treatment, and that 2) CM permeabilization is the key moment at which the burst of ROS formation occurs. We hypothesized that many antimicrobial peptides can induce ROS through similar mechanisms and that CM permeabilization is a key requirement for ROS formation.

Perhaps it is not surprising that Melittin showed the similar intensity trace of CellROX* and resorufin as did CM15. By design, 8 out of 15 residues in CM15 are identical to Melittin, and this region is thought to cause high toxicity toward both eukaryotic and prokaryotic cells.[14] Both CM15 and Melittin showed a burst of CellROX* and resorufin intensity upon CM permeabilization. This seemingly supported the previous hypothesis that CM permeabilization may be the key requirement for ROS formation under AMP treatment.

However, the results for both LL-37 and Indolicidin suggest that CM permeabilization may not be the primary requirement for ROS formation. Even though Indolicidin caused CM permeabilization in *E. coli* cells, the induced CellROX* intensity was much smaller (**Figure 4.4**). In addition, the LL-37 results clearly show that ROS formation precedes OM permeabilization, as evident by the increase CellROX* intensity prior to either OM or CM

permeabilization. It seems that the accumulation of LL-37 in the periplasm causes the increase in ROS formation. The rate at which ROS is generated seemingly correlates with the rate of LL-37 accumulation in the periplasm. Accordingly, a faster rise of CellROX* signal correlates with earlier CM permeabilization. When CellROX* intensity rises slowly, we do not see either OM or CM permeabilization during the time scale of our measurement (~1 hr).

The cause of ROS formation under AMP treatment is currently unknown. However, we have much evidence that active aerobic cellular respiration is necessary. In previous studies with CM15, we showed that the cells pretreated with either cyanide or azide showed attenuated CellROX* intensity. Cyanide and azide preferentially attack the cytochrome oxidase-*bo3* complex, thus stopping the active respiration through this complex. Active respiration itself evidently does not oxidize CellROX*, as evident by low CellROX* signal from cells under the anaerobic respiration using nitrate as a terminal electron acceptor. We further confirmed that LL-37 showed attenuated CellROX* intensity for the cells pretreated with CCCP (preliminary data, **Figure 4.6**). CCCP is a protonophore that equilibrates the proton gradient across the cytoplasmic membrane. This stops transport of glucose into the cytoplasm, ultimately halting cellular respiration and growth. This result further supports our hypothesis that active aerobic cellular respiration is important for generation of ROS under AMP treatment.

Surprisingly, the active cellular respiration is also important for the activity of bactericidal antibiotics. The recent studies by Collins *et. al.* suggested that the growth inhibition through blocking the active respiration attenuate the killing by bactericidal antibiotics, such as Norfloxacin, Ampicillin, and Gentamicin. The elevated active respiration under these bacteriocidal antibiotics has shown to cause reactive oxygen species (ROS). It is currently debated whether the formation of ROS is important for oxygen-mediated killing by these

antibiotics, but it is clear that the cellular respiration is important for these. Further studies are necessary to elucidate 1) the relationship between bactericidal activity and ROS interaction, 2) the cause of ROS formation under aerobic condition by AMPs.

Here, we showed that highly cationic AMP accumulates in the periplasm of cells. The accumulation of highly cationic AMP in the periplasm enables strong interaction with the outer leaflet of the CM. We hypothesize that this perturbs active aerobic cellular respiration, causing inappropriate release of superoxide and other partially reduced oxygen species into the cytoplasm. This slows the growth and ultimately the membrane permeabilization completely halts the growth. Further tests are needed to confirm the molecular target of these peptides.

Table 4.1. Antimicrobial Peptides (AMPs) Used in This Study

AMPs	Sequence	Charge
LL-37	***LLGDFFRKSKEKIGKEFKRIVQRIKDFLRNLVPRTES***	+6
Melittin	***GIGAVLKVLTTGLPALISWIKRKRQQ***	+5
CM15	**KWKLFKKIGAVLKVL**	+5
Indolicidin	***ILPWKWPWWPWRR***	+3

Table 4.2. Minimum Inhibitory Concentrations (MICs) of AMPs under aerobic and anaerobic conditions.

AMPs	+O_2, MIC (μM)	-O_2, MIC (μM)
LL-37	4	16
Melittin	4	32
CM15	5	100
Indolicidin	32	32

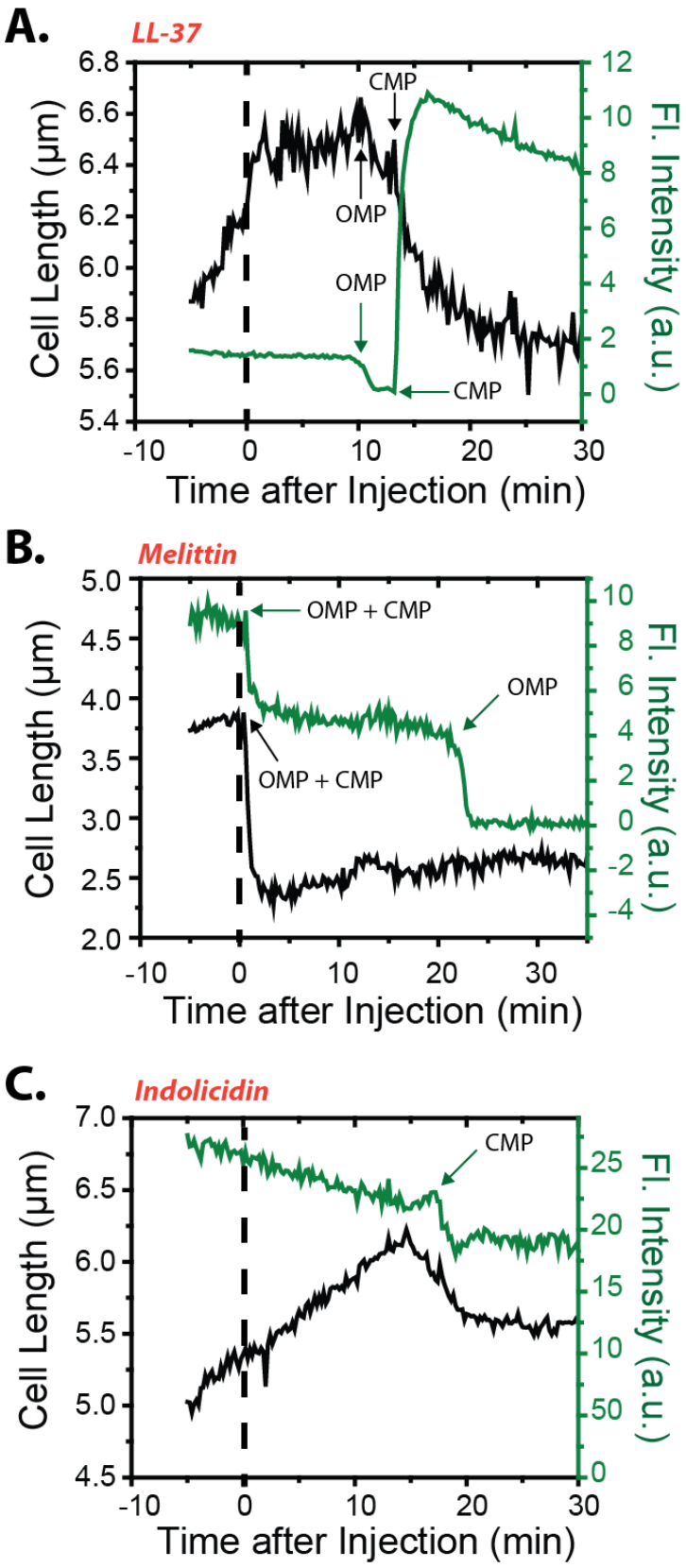

See next page for the detailed figure legend.

Figure 4.1 (A) Effects of 4 μM LL-37 (the 6-hr aerobic MIC) with 5 nM SYTOX green on MG1655 *E. coli* expressing periplasmic GFP. Single-cell time dependence of cell length (from phase contrast images) and total GFP and SYTOX green fluorescence intensity before and after injection of 4 μM LL-37. Outer membrane permeabilization (OMP) and cytoplasmic membrane permeabilization (CMP) are denoted with arrows in the figure. The initial decrease of fluorescence is due to GFP leaking out of the periplasm to the surrounding. The burst of fluorescence intensity at the later time is from accumulation of SYTOX green into cytoplasm upon CM permeabilization. (B) Effects of 10 μM Melittin (twice the 6-hr aerobic MIC) on MG1655 *E. coli* expressing periplasmic GFP. Single-cell time dependence of cell length (from phase contrast images) and total GFP fluorescence intensity before and after injection of 10 μM Melittin. Nearly simultaneous OMP and CMP are observed from the sudden drop of GFP fluorescence and the changes in periplasmic GFP distribution. The cell shrinkage correlates with the OM permeabilization. (C) Effects of 30 μM Indolicidin (the 6-hr aerobic MIC) on MG1655 *E. coli* expressing periplasmic GFP. Single-cell time dependence of cell length (from phase contrast images) and total GFP fluorescence intensity before and after injection of 30 μM Indolicidin. Only CM permeabilization is observed. The observed permeabilization is on average 1 min after the cell shrinkage.

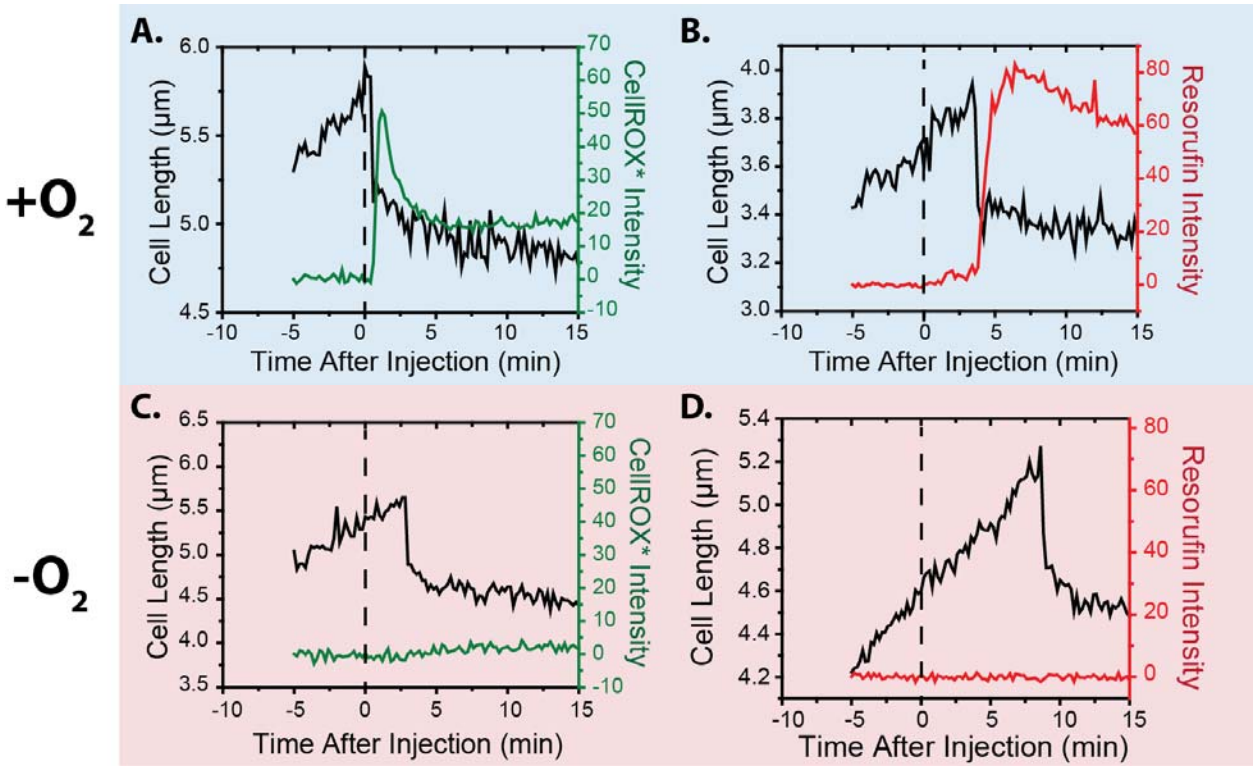

Figure 4.2 CellROX* signal (left) and Resorufin signal (right) under the treatment of 10 μM Melittin on K12 MG1655 *E. colli* growing in aerobic (upper panel) and anaerobic (lower panel) conditions. The injection of Melittin occurred at time = 0 min for all the conditions.

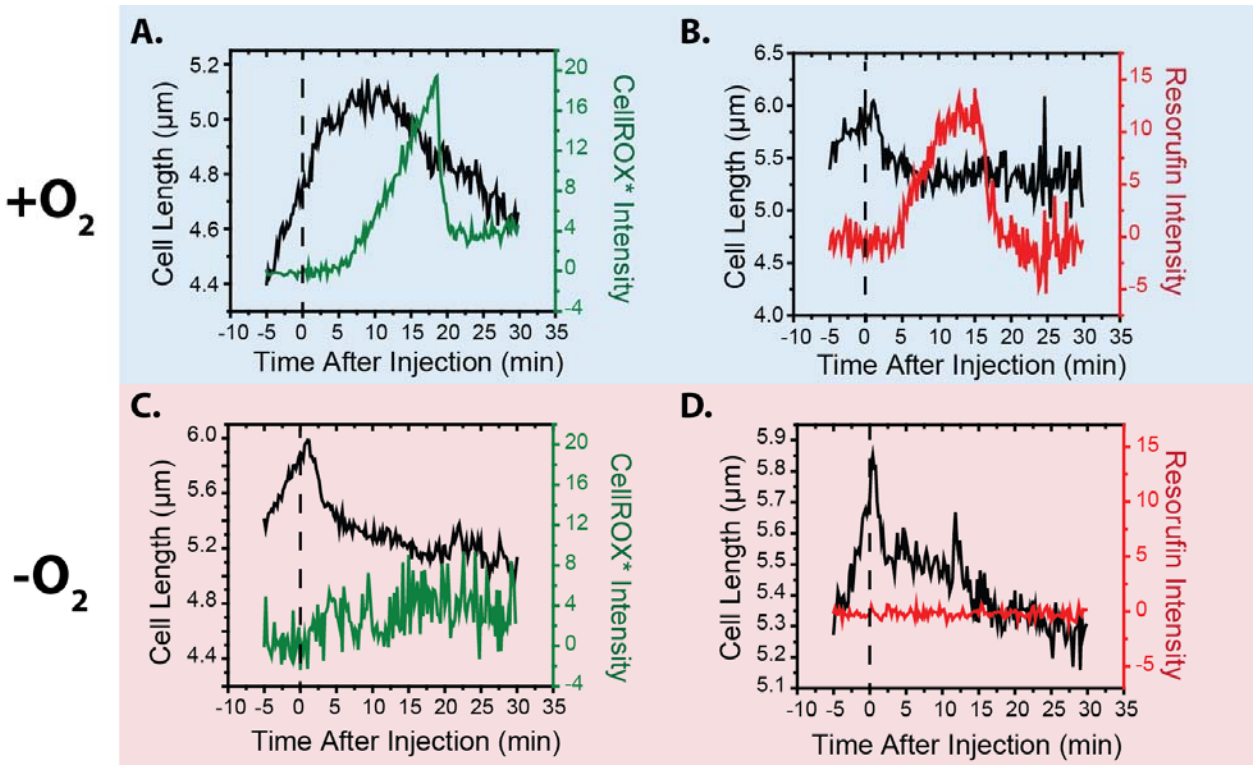

Figure 4.3 CellROX* signal (left) and Resorufin signal (right) under the treatment of 4 μM LL-37 on K12 MG1655 *E. colli* growing in aerobic (upper panel) and anaerobic (lower panel) conditions. The injection of LL-37 occurred at time = 0 min for all the conditions.

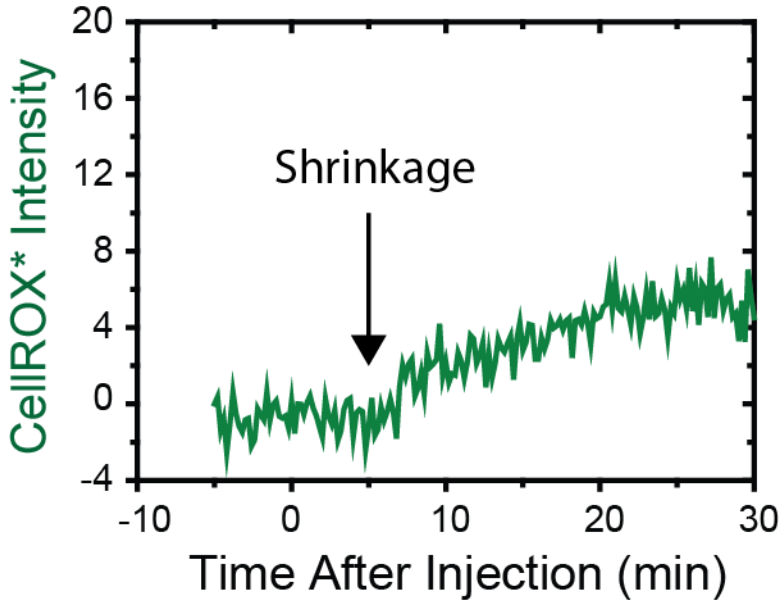

Figure 4.4 CellROX* intensity under the treatment of 30 μM Indolicidin. The injection occurred at time = 0. The length measurement cannot be done accurately under this condition due to changes in phase contrast images. The visual shrinkage time, however, is denoted with the arrow. CellROX* intensity begins to rise upon the cell shrinkage.

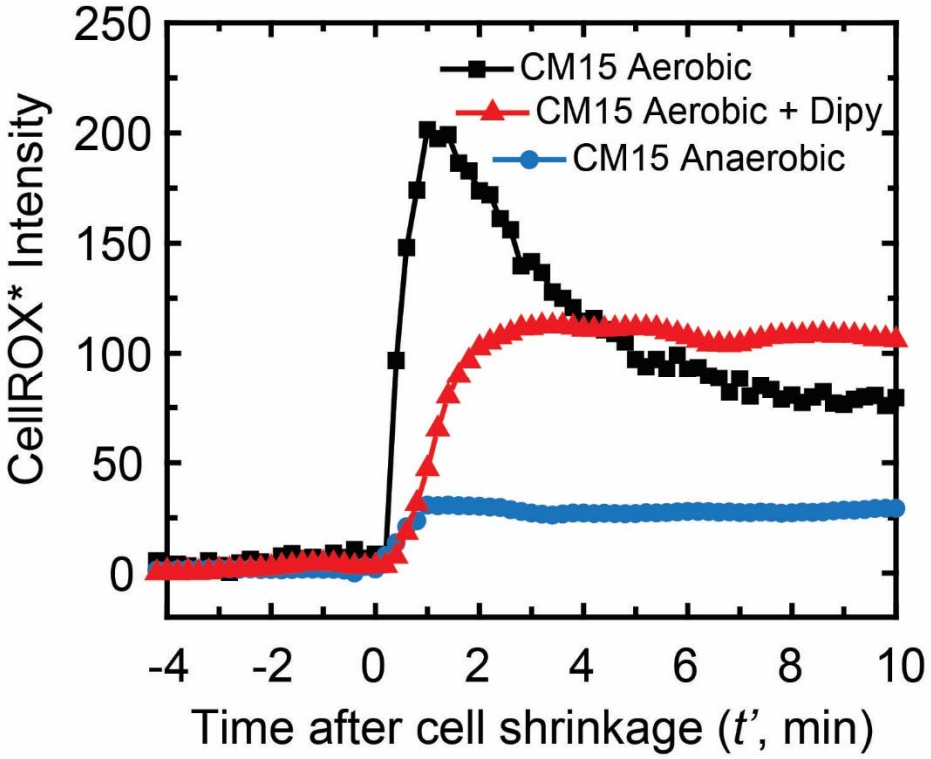

Figure 4.5 Comparison of representative single-cell CellROX* fluorescence intensity traces after CM15 addition in aerobic conditions, in aerobic conditions with addition of 2,2'-dipyridyl (iron chelating agent), and in anaerobic conditions.

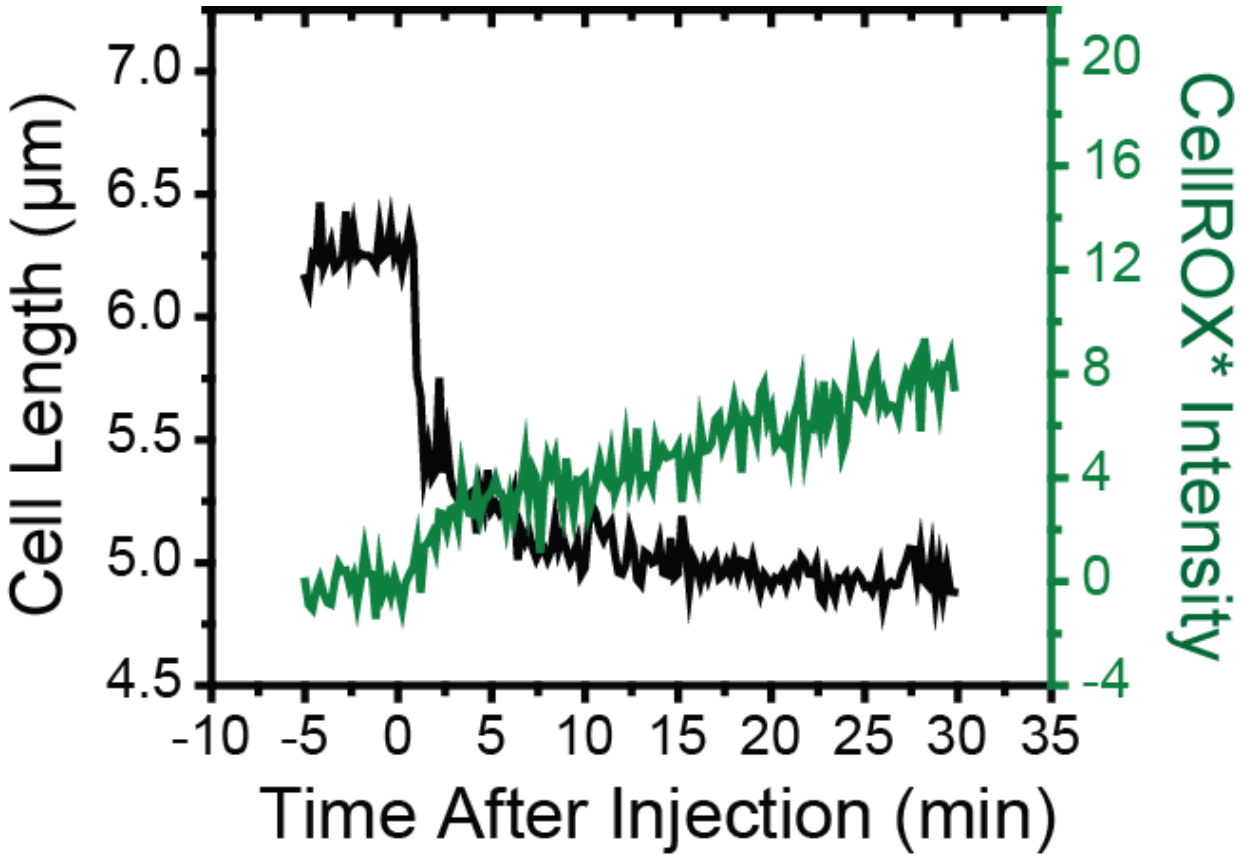

Figure 4.6 CellROX* intensity under the treatment of 4 μM LL-37 on WT MG1655 pretreated with CCCP.

References

1. Cullen, T. W.; Schofield, W. B.; Barry, N. A.; Putnam, E. E.; Rundell, E. A.; Trent, M. S.; Degnan, P. H.; Booth, C. J.; Yu, H.; Goodman, A. L., Gut microbiota. Antimicrobial peptide resistance mediates resilience of prominent gut commensals during inflammation. *Science* **2015,** *347* (6218), 170-5.

2. (a) Brogden, K. A., Antimicrobial peptides: pore formers or metabolic inhibitors in bacteria? *Nat Rev Micro* **2005,** *3* (3), 238-250; (b) Zasloff, M., Antimicrobial peptides of multicellular organisms. *Nature* **2002,** *415* (6870), 389-395; (c) Hancock, R. E. W.; Sahl, H.-G., Antimicrobial and host-defense peptides as new anti-infective therapeutic strategies. *Nat Biotech* **2006,** *24* (12), 1551-1557.

3. (a) Turner, J.; Cho, Y.; Dinh, N. N.; Waring, A. J.; Lehrer, R. I., Activities of LL-37, a cathelin-associated antimicrobial peptide of human neutrophils. *Antimicrobial Agents and Chemotherapy* **1998,** *42* (9), 2206-2214; (b) Rosen, H.; Lewis, P. J.; Nitzel, C. M., Neutrophil microbicidal activity: screening bacterial mutants for survival after phagocytosis using quantitative PCR. *Jpn J Infect Dis* **2004,** *57* (5), S19-21.

4. Grimm, M. C.; Pavli, P., NOD2 mutations and Crohn's disease: are Paneth cells and their antimicrobial peptides the link? *Gut* **2004,** *53* (11), 1558-60.

5. Schroeder, B. O.; Wu, Z.; Nuding, S.; Groscurth, S.; Marcinowski, M.; Beisner, J.; Buchner, J.; Schaller, M.; Stange, E. F.; Wehkamp, J., Reduction of disulphide bonds unmasks potent antimicrobial activity of human beta-defensin 1. *Nature* **2011,** *469* (7330), 419-23.

6. Choi, H.; Yang, Z.; Weisshaar, J. C., Single-cell, real-time detection of oxidative stress induced in Escherichia coli by the antimicrobial peptide CM15. *Proceedings of the National Academy of Sciences of the United States of America* **2015,** *112* (3), E303-E310.

7. Sochacki, K. A.; Shkel, I. A.; Record, M. T.; Weisshaar, J. C., Protein diffusion in the periplasm of E. coli under osmotic stress. *Biophys J* **2011,** *100* (1), 22-31.

8. Neidhardt, F. C.; Bloch, P. L.; Smith, D. F., Culture medium for enterobacteria. *J Bacteriol* **1974,** *119* (3), 736-47.

9. Sochacki, K. A.; Barns, K. J.; Bucki, R.; Weisshaar, J. C., Real-time attack on single Escherichia coli cells by the human antimicrobial peptide LL-37. *Proc Natl Acad Sci U S A* **2011,** *108* (16), E77-81.

10. Aitken, C. E.; Marshall, R. A.; Puglisi, J. D., An oxygen scavenging system for improvement of dye stability in single-molecule fluorescence experiments. *Biophys. J.* **2008,** *94* (5), 1826-1835.

11. Park, S.; You, X. J.; Imlay, J. A., Substantial DNA damage from submicromolar intracellular hydrogen peroxide detected in Hpx(-) mutants of Escherichia coli. *Proceedings of the National Academy of Sciences of the United States of America* **2005,** *102* (26), 9317-9322.

12. Dwyer, D. J.; Belenky, P. A.; Yang, J. H.; MacDonald, I. C.; Martell, J. D.; Takahashi, N.; Chan, C. T.; Lobritz, M. A.; Braff, D.; Schwarz, E. G.; Ye, J. D.; Pati, M.; Vercruysse, M.; Ralifo, P. S.; Allison, K. R.; Khalil, A. S.; Ting, A. Y.; Walker, G. C.; Collins, J. J., Antibiotics induce redox-related physiological alterations as part of their lethality. *Proc Natl Acad Sci U S A* **2014,** *111* (20), E2100-9.

13. (a) Sochacki, K. A.; Shkel, I. A.; Record, M. T.; Weisshaar, J. C., Protein Diffusion in the Periplasm of E-coli under Osmotic Stress. *Biophys. J.* **2011,** *100* (1), 22-31; (b) Sochacki, K. A.; Barns, K. J.; Bucki, R.; Weisshaar, J. C., Real-time attack on single Escherichia coli cells by the human antimicrobial peptide LL-37. *Proceedings of the National Academy of Sciences of the United States of America* **2011,** *108* (16), E77-E81.

14. Andreu, D.; Ubach, J.; Boman, A.; Wahlin, B.; Wade, D.; Merrifield, R. B.; Boman, H. G., SHORTENED CECROPIN-A MELITTIN HYBRIDS - SIGNIFICANT SIZE-REDUCTION RETAINS POTENT ANTIBIOTIC-ACTIVITY. *FEBS Lett.* **1992,** *296* (2), 190-194.

Chapter 5

Medium Effects on Minimum Inhibitory Concentrations of Nylon-3 Polymers against *E. coli*

Published as:

Choi H., Chakraborty S., Liu R., Gellman SH, Weisshaar J.C. "Medium Effects on Minimum Inhibitory Concentrations of Nylon-3 Polymers against *E. coli*." *PlosOne*. **9,** 2014.

***** Nylon-3 copolymers are synthesized by Saswata Chakraborty and Runhui Liu.

INTRODUCTION

There is a pressing need to develop new ways to kill harmful bacteria while causing minimal damage to eukaryotic cells [1]. An important component of the innate response to invasive bacteria is the release of antimicrobial peptides (AMPs) that permeabilize bacterial membranes and ultimately kill the invaders [2]. These peptides target bacterial membranes selectively relative to eukaryotic membranes. Thousands of natural AMPs are now known [3]. Substantial effort has been devoted to development of synthetic analogues containing α-amino acid residues and/or unnatural subunits that mimic the selective antibacterial action of AMPs. Examples include discrete oligomers generated from L-α-amino acids [4], N-alkyl glycines ("peptoids") [5], β-amino acids ("β-peptides") [6], or combinations of these building blocks. Many of these oligomers have been designed to adopt an amphipathic helical conformation, because this structural motif is common among natural AMPs.

The synthesis of sequence-specific oligomers requires a step-by-step approach, typically involving solid-phase methods, which is time-consuming and expensive. This synthetic problem has encouraged several research groups to explore polymerization-based methods to generate antimicrobial materials [7]. In many cases, a pair of precursors is copolymerized, with one precursor giving rise to a hydrophobic subunit and the other giving rise to a cationic subunit in the polymer chains. The resulting materials are heterogeneous, containing chains that vary in length, composition, subunit sequence and, frequently, subunit stereochemistry. Antibacterial activity in such cases cannot depend on adoption of a single amphipathic conformation. Nevertheless, careful tuning of the proportion and identities of the cationic and hydrophobic subunits can provide polymeric materials that exhibit strong bacteriostatic action against both

Gram negative and Gram positive bacteria at concentrations that do not cause destruction of red blood cells ("hemolysis").

Our recent structure-function study of binary nylon-3 copolymers (β-peptide backbone) showed that a specific proportion of hydrophobic and cationic subunits plus inclusion of a hydrophobic group such as p-*t*-butylbenzoyl at the N-terminus provided a favorable balance of bacteriostatic and hemolytic properties [7f]. Bacteriostatic potency was evaluated in terms of the minimum inhibitory concentration (MIC), the lowest polymer concentration that halted bacterial growth. Four bacterial species were evaluated, among which *Escherichia coli* was the only Gram negative organism. *E. coli* MIC measurements were carried out using brain-heart infusion (BHI) growth medium. Hemolytic activity was measured as the minimum hemolytic concentration (MHC), the smallest polymer concentration that caused detectable release of hemoglobin from human red blood cells.

We have been developing fluorescence microscopy methods that monitor membrane disruption induced by antimicrobial peptides acting on single bacterial cells in real time [8]. The broths typically used for rapid bacterial growth, including brain-heart infusion (BHI) and Luria-Bertani (LB), are unsuitable for sensitive fluorescence work due to their strong background fluorescence on excitation with visible light. Instead, we use a low-fluorescence, chemically defined medium called "EZ rich, defined medium" (EZRDM) [9]. As a prelude to studies of the mechanism of nylon-3 action against *E. coli*, we measured MIC values for a panel of nylon-3 polymers in the EZRDM medium. Surprisingly, we observed a dramatic reduction of MIC values (greater polymer efficacy) in EZRDM as compared with either BHI or LB. In particular, cationic homopolymers (lacking hydrophobic subunits) were much more effective against *E. coli* in EZRDM than in BHI or LB media.

We report studies intended to elucidate the effect of bacterial growth medium on MIC values measured for *E. coli*. By adding tryptone, the tryptic digest of bovine casein, to EZRDM, we recover the pattern of activity observed in BHI. We also present evidence indicating that anionic peptide components of tryptone (and, by extension, those in BHI and LB) diminish the ability of the highly cationic polymers to attack *E. coli* relative to the effects observed in EZRDM. This functional attenuation presumably results from formation of relatively inert electrostatically bound complexes between the cationic polymers and the anionic peptide components. In sharp contrast to the behavior of the cationic polymers, two natural AMPs (LL-37 and Cecropin A) showed consistent MIC values in all media. Another natural AMP, Magainin 2, was inactive against *E. coli* in EZRDM and had low activity in BHI as well. We suggest that the MIC measurements in EZRDM reveal the "intrinsic activity" of a polymer or AMP.

These results expand our understanding of structure-activity relationships among the nylon-3 polymers and suggest new design strategies for the future. Moreover, these observations highlight a previously undocumented feature of natural AMPs, which can apparently be fine-tuned by evolutionary selection to avoid the polyanion-based neutralization mechanism suggested by our polymer findings.

MATERIALS AND METHODS

Materials

The nylon-3 polymers used in this study (**Figure 5.1**) were synthesized as previously described [7f]. Polymers were prepared from racemic β-lactams, and each polymer was therefore heterochiral. Polymer samples had mean chain lengths of 27 (polymer **A**), 27 (**B**), and 24 (**C**). Polydispersity index (PDI) values ranged from 1.02-1.15. To check for possible batch-to-batch

variation in polymer properties, each polymer was synthesized twice. The MIC values measured for different batches of the same polymer were indistinguishable in each case. Human cathelicidin LL-37 was purchased from Bachem, and moth Cecropin A and Magainin 2 were purchased from Anaspec. All three peptides were used without purification. EZ rich defined medium (EZRDM, Teknova), brain heart infusion broth (BHI, Difco), and Luria-Bertani broth (LB, Sigma Aldrich) were purchased as powders and dissolved in water. Tryptone powder was purchased from BD Sciences. We compared the effects of supplements made from tryptone powder as received vs tryptone powder that was dissolved, dialyzed to remove small ions and solutes (1 kDa cutoff), and then lyophilized. No differences were observed. We use "tryptone" or "dialyzed tryptone" to mean a solution of the dialyzed tryptone powder dissolved in EZRDM. We use "raw tryptone" to mean a solution of the tryptone powder as received. The free base ion-exchange resin Amberlite IRA67 was purchased from Sigma Aldrich.

We devised two tests of the effects of anionic species within tryptone on MIC values. First, the large polyanions in raw tryptone were removed from dialyzed tryptone solution using a washed, free-base anion-exchange resin (Amberlite IRA67, Sigma Aldrich). At pH = 7, the resin removes H^+ and polyanions from solution. A solution of dialyzed tryptone was incubated with 1.2X (wt/wt) resin for 2 hr and then filtered to remove the beads. We designate the product of this operation "anion-exchanged tryptone". The filtered product was lyophilized and added to EZRDM for MIC assays. Second, we used solid-phase methods to synthesize a single, specific anionic peptide, FQSEEQQTEDELQDK, and tested its effects at 400 μM in EZRDM. This peptide is a putative component of raw tryptone based on the predicted products of digestion of bovine beta-casein by trypsin. The peptide was used without purification (estimated purity ~85%).

Minimum Inhibitory Concentration (MIC) Assay

E. coli strains JM109 and MG1655 were studied. MIC values were determined using a standard serial microdilution method. Serial two-fold dilutions of each nylon-3 polymer, and of LL-37, Cecropin A, and Magainin 2, were performed in separate rows of a polystyrene 96-well plate in the chosen medium containing an inoculum of either JM109 or MG1655. Polymer concentrations between 6.3 μg/mL and 200 μg/mL were evaluated. Each assay plate contained a dilution series with ampicillin as a positive control. To test for possible effects of the MIC procedural details, the measurements in BHI medium were carried out with cells initially sampled either from stationary phase (as in the earlier study) [7f] or from mid-log phase. In the stationary phase procedure, a culture grown overnight at 37ºC to stationary phase was sampled and diluted to $OD_{600} = 0.05$ with medium at the same temperature. In the mid-log phase procedure, the stationary culture was diluted in fresh medium (1:100) and grown until it reached $OD_{600} = 0.5$. For the MIC measurements, the plate was incubated at 37°C for 6 hr. For both the stationary phase procedure and the mid-log phase procedure, we tested for effects of stationary incubation in a VWR 1525 digital incubator vs increased aeration due to shaking at 200 rpm in a Lab-Line Orbital Environ Shaker (Model 3527). For experiments augmenting EZRDM medium with tryptone solution, the appropriate amount of raw or dialyzed tryptone powder was dissolved in EZRDM and used in the dilution steps.

The MIC results were not affected by the choice of *E. coli* strain or any of the other variations in experimental procedure. Following these initial tests, our standard procedure used stationary phase cultures with no shaking during outgrowth and tryptone solution made from dialyzed tryptone powder. The overnight culture of *E. coli* was grown in EZRDM prior to the addition of tryptone supplemented EZRDM.

The MIC is reported as the lowest concentration for which no cell growth could be detected after 6 hr (OD = 0.00 ± 0.05), as determined by measurements at 595 nm using an EnVision 2100 Multilabel Reader (Perkin-Elmer). Examples of OD vs time curves are provided in Appendix 5A, 5B, and 5C. With care, the resulting MIC measurements are more accurate than a factor of two, as evidenced by exact reproduction over repeated trials of the particular concentration step that halted growth over 6 hr. When growth inhibition did not occur at the highest concentration of polymer studied (200 μg/mL), we report 200 μg/mL as a lower bound on the MIC, denoted by an upward arrow in the MIC bar graphs (**Figure 5.2**).

RESULTS

Experimental Design

This study focuses on three nylon-3 polymers that have been previously described [7f] (**Figure 5.1**; **A-C**). **A** is a copolymer generated from a ring-opening polymerization reaction mixture containing two β-lactams, CHβ and MMβ, in 37:63 molar ratio. "CH" denotes a hydrophobic cyclohexyl side chain within the monomer and "MM" (monomethyl) denotes a single methyl group at the C_α site of the cationic monomer. Since the β-lactams are racemic, the resulting polymer sample contains chains with many different stereochemistries, as well as many different sequences. After polymerization, deprotection provides a side chain amino group in the MM subunit. These amino groups are protonated when the polymer is dissolved in aqueous solution near or below neutral pH, which confers a positive charge on the polymer.

The 37:63 ratio of CH and MM subunits was previously shown [7f] to provide a favorable compromise between antibacterial activity in BHI medium (lower MIC preferred) and hemolytic activity (higher minimum hemolytic concentration, MHC, preferred). Antibacterial activity in BHI medium was enhanced by the presence of a hydrophobic group at the N-terminus of the

polymer chains; **A** bears a p-*t*-butylbenzoyl group at this position. In BHI medium, nylon-3 polymers **B** and **C** showed diminished antibacterial activity relative to **A**. Copolymer **B** shares the 37:63 CH:MM ratio of **A**, but **B** lacks a hydrophobic group at the N-terminus. **C** is a homopolymer of the cationic MM subunit.

We were originally motivated to explore cationic-hydrophobic copolymers such as **A** because AMPs are commonly rich in both cationic and hydrophobic amino acid residues. A net positive charge is believed to be necessary to attract AMPs to the lipopolysaccharide (LPS) surface of a bacterial cell, which bears a net negative charge. Hydrophobic side chains are thought to be essential for interaction with the nonpolar interior of a lipid bilayer and the resulting membrane barrier disruption. From this perspective, it is sensible that a cationic homopolymer such as **C** would not display strong antibacterial effects, as observed in previous studies of *E. coli* MICs conducted in BHI medium [7f]. We were therefore surprised to discover that cationic homopolymer **C** is highly active against *E. coli* in the chemically defined EZRDM. The experiments described here were undertaken to try to determine why MIC results differ between a traditional but chemically undefined medium such as BHI and chemically defined EZRDM.

EZRDM is a MOPS-buffered solution that contains glucose (0.2%), supplemental amino acids and vitamins, nucleotides, 1.32 mM K_2HPO_4, and 76 mM NaCl. This is our preferred medium for optical imaging experiments on bacteria because of its low autofluorescence [9]. In contrast, BHI medium is not chemically defined, since it is generated from calf brain and heart. BHI medium is supplemented with peptone, a digest of an undefined mixture of proteins from cow and pig. The enzyme used in the digest is proprietary, and the peptide mixture in peptone is therefore uncharacterized. As shown below, we found that *E. coli* MIC studies conducted in LB

provide results similar to those conducted in BHI. LB is a common bacterial growth medium that, like BHI medium, is chemically undefined. LB medium contains tryptone along with yeast extract and sodium chloride. Tryptone is generated via tryptic digestion of casein.

We considered the hypothesis that peptides from a supplement such as tryptone (an additive in LB) or peptone (an additive in BHI medium) might interact with cationic nylon-3 polymers in a way that affects antibacterial potency. Since EZRDM contains amino acids rather than enzymatically generated peptides, the peptide-polymer interactions that we proposed to inhibit antibacterial activity of nylon-3 polymers would not be possible in EZRDM. Thus, the absence of enzymatically generated peptides in EZRDM might explain why polymer MIC values were lower in this medium than in LB or BHI medium.

This hypothesis was tested by supplementing EZRDM with dialyzed tryptone solution. The supplement was generated by dialyzing raw tryptone solution against pure water for 48 hr to remove small ions and molecules below 1000 Da. The retained material was assumed to be composed largely of peptides generated via the cleavage of casein by trypsin. The retained solution was lyophilized, and the resulting dialyzed tryptone powder was added in varying proportions to EZRDM. As shown by the data presented below, this simple supplementation strategy caused a shift in nylon-3 MIC values for *E. coli* from the EZRDM profile to the profile observed in complex media such as BHI or LB.

Two additional sets of measurements tested whether or not anionic peptides were responsible for the larger MIC values observed on addition of dialyzed tryptone to EZRDM. We measured MICs against *E. coli* for copolymers **A**, **B**, and **C** in EZRDM supplemented by the single anionic peptide FQSEEQQTEDELQDK. We also measured MICs for **A**, **B**, and **C** in EZRDM supplemented with anion-exchanged tryptone, which should lack anionic polypeptides.

Both tests support the hypothesis that complexation of the highly cationic copolymer with polyanionic peptides diminishes antimicrobial activity.

MIC measurements for polymers

Results obtained for the nylon-3 polymers in BHI medium (**Figure 5.2**) agree with previous reports: cationic-hydrophobic copolymer **A** displays moderate activity against *E. coli* in this medium, but absence of the hydrophobic N-terminal group (copolymer **B**) or absence of the hydrophobic CH subunits (homopolymer **C**) leads to a profound loss of activity. MIC values measured in LB medium show the same pattern as those measured in BHI medium (**Figure 5.2**). In contrast, the MIC pattern in EZRDM is quite different: all three polymers are more active in EZRDM than in BHI or LB, and there is little distinction among the three polymers in EZRDM.

We supplemented EZRDM with dialyzed tryptone solution at three concentrations, 1 g/L, 5 g/L or 10 g/L, to generate media designated "EZ + 0.1X tryptone", "EZ + 0.5X tryptone" and "EZ + 1X tryptone". These designations are based on the fact that LB medium typically contains 10 g of tryptone powder per liter. Detailed MIC curves and MIC values vs tryptone concentrations are included in Appendix 5C. The antimicrobial activity of each polymer decreases (i.e., MIC value increases) as the concentration of dialyzed tryptone in EZRDM increases. The effects of 1X tryptone supplement on the MIC values for the three polymers are included in **Figure 5.2**. The factor by which the MIC increases depends on polymer composition: polymer **A**, which is the most active of the three in complex media, is less strongly affected than polymers **B** and **C**, both of which are inactive in complex media but highly active (low MIC values) in EZRDM. Supplementation of EZRDM with 1X dialyzed tryptone recapitulates the effects of BHI and LB on MIC values. Polymer **A**, the most active polymer in BHI and LB, is

the only polymer that retains reasonably good activity in EZRDM supplemented with 1X tryptone, in BHI, and in LB.

To test the ability of polyanions within dialyzed tryptone to alter MICs, we supplemented EZRDM with anion-exchanged tryptone, from which polyanionic components have been removed. The concentration of anion-exchanged tryptone was 10 g/L (as in 1X tryptone) *minus* the mass of the polyanions removed by the resin. The effects on MIC values for the three polymers are summarized in **Figure 5.2**. Removal of polyanions from tryptone drastically reduces the MICs of the three polymers to the point where they are comparable to the MICs in EZRDM. In addition, the pattern of relative MICs in EZRDM is recovered by removal of anionic molecules from the tryptone additive.

To investigate further the effect of polyanionic peptides in tryptone, the anionic peptide FQSEEQQTEDELQDK was added to EZRDM without tryptone supplementation. The anionic peptide concentration was chosen as 200 μM or 400 μM. The value 400 μM matches the estimated concentration of this particular peptide in 1X tryptone (based on 10 g/L of the digest products of the 23 kDa protein bovine beta-casein). The MICs of all three polymers increased with added concentration of the anionic peptide, as shown in Appendix 5E. Addition of 400 μM of added anionic peptide increases the MICs of all three polymers by a factor of four to eight compared with EZRDM (**Figure 5.2**).

MIC measurements for antimicrobial peptides

For comparison, we measured the MIC values against *E. coli* of two natural antimicrobial peptides, LL-37 and Cecropin A, in four media: BHI, EZRDM, and EZRDM supplemented with 0.5X or 1X tryptone. As shown in **Figure 5.3**, LL-37 and Cecropin A showed strong antimicrobial activity in all four media. Detailed OD data are provided in Appendix 5D. In fact,

MIC values for these two AMPs were slightly smaller in EZRDM plus 1X tryptone than in unsupplemented EZRDM. The natural AMP Magainin 2 was not active against *E. coli* in EZRDM (MIC > 100 μM) and had an MIC of 40 μM in BHI. Unlike polymers **A-C**, Magainin 2 does not gain activity when the medium changes from BHI to EZRDM (**Figure 5.3**).

DISCUSSION

Medium Effects on polymer MIC values

The susceptibility of bacteria to antibiotics, including antimicrobial peptides, can depend on environmental conditions such as temperature, aeration, and pH, as well as the concentrations of ionic species [2b]. A high concentration of Ca^{2+} [10] or Mg^{2+} [11] in the growth medium increases MIC values for AMPs, presumably due to competition between the divalent cation and the cationic peptide for binding sites within the bacterial cell surface. Addition of polyanions such as DNA [12] also increases MIC values, presumably by binding to cationic AMPs and decreasing the concentration of free AMP available for disruptive interactions with the bacterial cell surface. To avoid such complications, most laboratories screen for antimicrobial peptide activity without varying the growth medium. The few studies that compare MIC values between two different media [13] have not provided clear conclusions because of the inherent complexity of the broths employed. The present work compares cationic polymer and AMP activities in two widely used complex media (BHI and LB) with activities in a chemically defined medium (EZRDM). This experimental design enables us to draw some tentative conclusions about the underlying causes of the strong variation in MIC values across media.

Our primary finding is that BHI (which usually contains peptone supplement) and LB (which contains tryptone supplement) suppress polymer activity against *E. coli* as compared with EZRDM (which contains only small molecules). By adding 1X dialyzed tryptone solution to

EZRDM, we were able to recapitulate polymer performance in BHI and LB. To avoid possibly confounding effects of small molecules such as salts, sugar, vitamins, and divalent cations, we used material derived from tryptone powder via dialysis vs water for several days, followed by lyophilization. We therefore attribute the effects of adding tryptone to EZRDM to the polypeptides that are generated via tryptic digestion of casein.

What are these polypeptides? Trypsin cleaves peptide bonds specifically at the C-terminal side of lysine and arginine residues. Complete digestion necessarily produces peptides with only one positive charge (at the C-terminus). Digest products are thus intrinsically biased to be negatively charged or hydrophobic or both. The sequence of bovine casein and the predicted products of its complete digestion by trypsin are shown in **Figure 5.4**. This predicted mixture includes six peptides containing 1–7 residues, which have a net charge of +1 or are neutral; such small peptides are presumably depleted from raw tryptone solution during dialysis. In addition, there are five longer peptides, including three that contain 16–24 residues (net charge ranging from –1 to –6), one with 48 residues (neutral) and one with 56 residues (net charge –3). Highly anionic components include 16-mer FQSEEQQTEDELQDK (net charge -5), and 24-mer ELE…, with net charge -6. The two longest peptides are highly hydrophobic.

Supplementation of EZRDM with 1X tryptone causes a profound diminution in the ability of polymers **A**-**C** to inhibit growth of *E. coli* (**Figure 5.2**). We propose that all three polymers bind to the polyanionic peptides generated via tryptic digestion of casein. The resulting polymer-anionic peptide complexes presumably bind less strongly to the anionic lipopolysaccharide (LPS) layer found on the outer surface of *E. coli* than do uncomplexed polymers. Even for polymer **A**, which displays significant activity in BHI, the MIC decreases fourfold from EZRDM

plus 1X tryptone to EZRDM or from LB to EZRDM, and eightfold from EZRDM to BHI from EZRDM.

This hypothesis is further supported by the MIC pattern of the three polymers in EZRDM supplemented with anion-exchanged tryptone, which is quite similar to the MIC pattern in EZRDM alone (**Figure 5.2**). Addition of the anionic peptide FQSEEQQTEDELQDK, which is predicted to be generated by digestion of beta-casein with trypsin, increased the MICs of the three polymers by a factor of four to eight (**Figure 5.2**). Addition of this peptide did not, however, match the full tryptone-induced increases in MICs for polymers **B** and **C**. This finding with a specific peptide supports our hypothesis regarding the MIC-suppressing effects of polyanionic components on a polymer's antibacterial activity. However, this observation also suggests that the interactions between constituents of the polyanion mixture in tryptone and a heterogeneous cationic polymer sample may be difficult to understand in detail.

There is precedent for our observation that the antibacterial effect of highly cationic polymers can be sensitive to the growth medium. The cationic homopolymer ε-polylysine is used as a food preservative based on its antibacterial effects [14]. The reported MIC for ε-polylysine against *E. coli* decreases from 50 μg/mL [15] to 1 μg/mL [16] (50-fold) when the growth medium is changed from nutrient buffer (which includes peptone) to Davis medium (which is a chemically defined medium containing "casamino acids", a mixture of *monomeric* α-amino acids). Since the ingredients of Davis medium do not include a *peptide*-rich component generated via enzymatic degradation of proteins, such as peptone or tryptone, the pronounced effect of medium on the antibacterial activity of ε-polylysine is consistent with our conclusions about the antibacterial activity of cationic nylon-3 polymers. Our results may also be relevant to studies

using cationic peptides to enhance the permeability of the outer membrane to hydrophobic drugs [17].

Implications for the design of antimicrobial polymers

The three polymers evaluated here were selected based on a previous study of structure-function relationships within the nylon-3 family [7f]. That study measured MIC (in BHI medium) and minimum hemolytic concentration (MHC) values for polymers that varied in the nature of the hydrophobic and cationic subunits, the ratio of hydrophobic to cationic subunits, the N-terminal group, and the mean chain length. The composition embodied in polymer **A**, at ~25-mer average chain length, exhibited the best performance overall. This nylon-3 polymer displayed moderate MIC values against both Gram negative and Gram positive bacteria along with a high MHC value. Analogous polymer **B**, which lacks the hydrophobic unit at the N-terminus, was far less active than **A** against *E. coli*. Homopolymer **C** also was far less active than **A** against *E. coli*, which indicated that hydrophobic CH subunits are critical for conferring antibacterial activity on polymer **A**. The trends previously observed among nylon-3 polymers **A**-**C** are consistent with conclusions drawn from studies of natural AMPs and analogous synthetic peptides, which suggest that optimizing antibacterial activity while simultaneously minimizing eukaryotic cell toxicity (e.g., hemolytic activity) requires the presence of both hydrophobic and cationic subunits, with a proper balance between net charge and net lipophilicity [18].

The previous nylon-3 studies were conducted in BHI medium. The present results show that the impact of introducing hydrophobic subunits or cationic N-terminal groups can be dramatically altered by changing the medium. We observe that all three nylon-3 polymers are more active against *E. coli* (lower MIC values) in EZRDM than in BHI medium. Most striking

is the observation that cationic homopolymer **C** is highly active in EZRDM, while this polymer has very little activity against *E. coli* in BHI medium.

Our study raises the general question of which media are most appropriate for evaluating the activity of new antimicrobial candidates. The ε-polylysine precedent [14] and the sensitivity to medium we document for highly cationic polymers suggest that investigations in chemically defined media have substantial merit for such evaluations. In addition, many pathogenic bacteria are more virulent in minimal growth conditions than in rich growth conditions [19], a trend that argues for using a chemically defined *minimal* medium to evaluate the antimicrobial activities of new polymers.

The natural cationic AMPs LL-37 and Cecropin A are remarkably impervious to the medium effects that we find to be so strong for the highly cationic polymers (**Figure 5.3**). AMPs may have evolved so as to maintain their efficacy in a variety of environments. The sequences of LL-37 and Cecropin A (**Figure 5.5**) are perhaps instructive. The positive charge density is smaller, on a per-subunit basis, in the natural AMPs than in nylon-3 polymers **A-C** because the peptides contain residues that are neither positively charged nor hydrophobic. The lower positive charge density and the inclusion of some negatively charged residues may diminish binding of the natural AMPs to polyanionic species in BHI and in tryptone-supplemented EZRDM. This speculation suggests that it may prove fruitful to study random polymers comprising three or even four components, with proportions of cationic, anionic, and hydrophobic monomers chosen to mimic those found in natural AMPs. Unlike the nylon-3 polymers, which gained activity when moved from BHI to EZRDM, Magainin 2 showed low activity (MIC = 40 μM) in BHI and no activity (MIC > 100 μM) in EZRDM (**Figure 5.3**). Magainin 2, with 23 residues and a net

charge of +3 at neutral pH, may not be sufficiently cationic to bind effectively to the LPS layer of Gram negative species.

It is possible that AMPs and highly positive nylon-3 polymers attack bacterial cells by different mechanisms, and that the mechanism of action varies among the nylon-3 polymers. Many AMPs fold into amphipathic helices and may form membrane pores of reasonably well defined structure. Defined conformations are not available to the sequence-random copolymers or the purely cationic polymers studied here. It is not clear how a highly cationic polymer such as **C** could cause membrane disruption, which evidently underlies the antibacterial effects of peptides such as LL-37 and Cecropin A [8]. The observation that diverse nylon-3 polymers display strong growth-inhibitory activity toward *E. coli* in EZRDM will enable detailed investigations of the mechanism(s) of action via optical imaging methods.

ACKNOWLEDGMENTS

Research reported in this publication was supported by the National Institute of General Medical Sciences of the National Institutes of Health. The content is solely the responsibility of the authors and does not necessarily represent the official views of the National Institutes of Health.

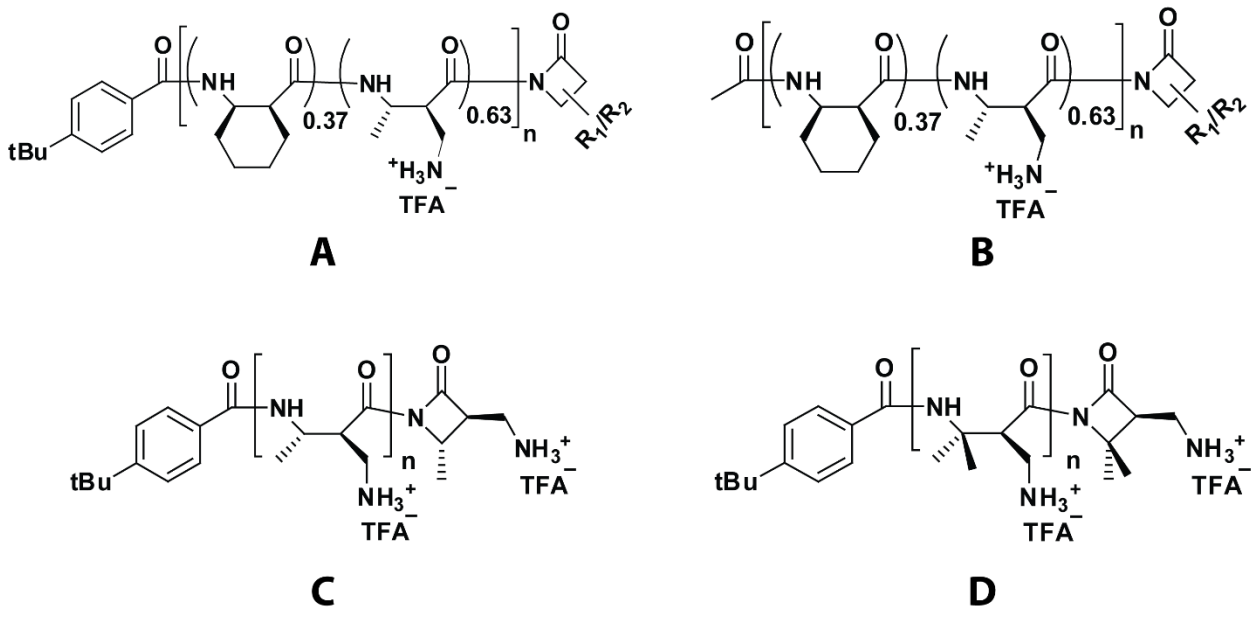

Figure 5.1 Structure of the random, heterochiral nylon-3 polymers **A**, **B**, and **C** used in this study.

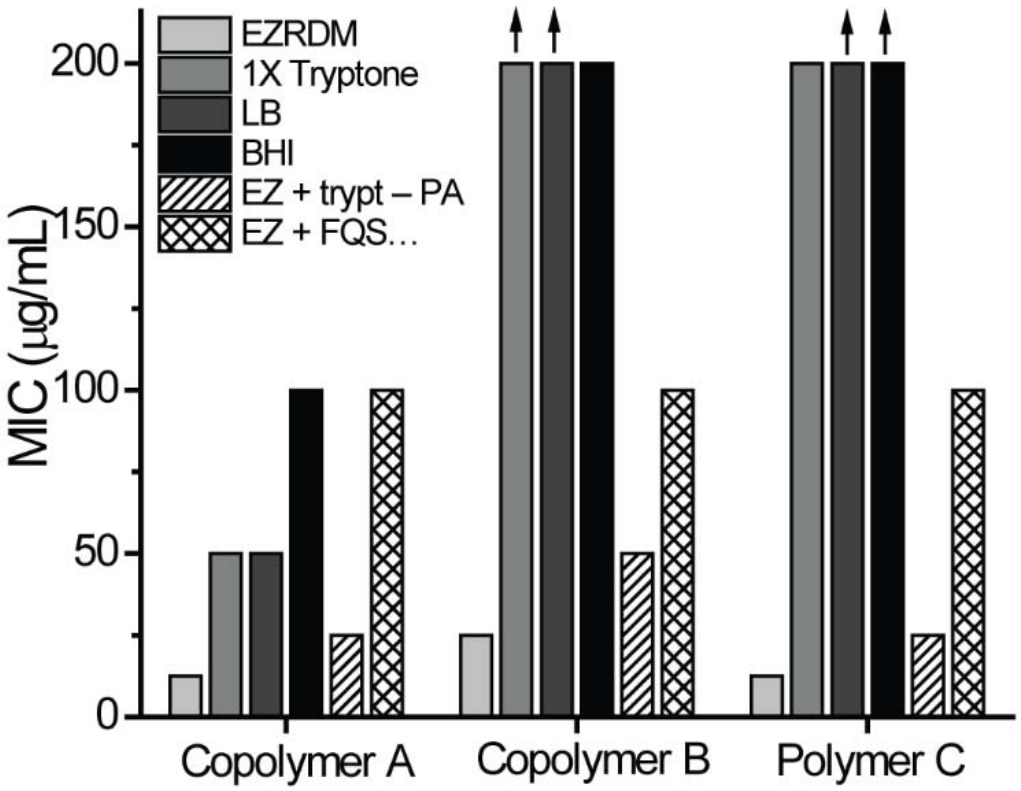

Figure 5.2 Minimum inhibitory concentrations (MICs) of nylon-3 polymers **A**, **B**, and **C** (**Figure 5.1**) against *E. coli* for different media. Vertical arrows mark bars that are lower limits only. EZRDM, LB, and BHI as described in main text. The designation "EZ + trypt" refers to EZRDM supplemented with 10 g/L of dialyzed tryptone powder (1X tryptone). "EZ + trypt – PA" refers to EZRDM supplemented with anion-exchanged tryptone at the equivalent of 10 g/L. "EZ + FQS…" refers to EZRDM supplemented with 400 μM of the single anionic peptide FQSEEQQTEDELQDK (net –5 charge).

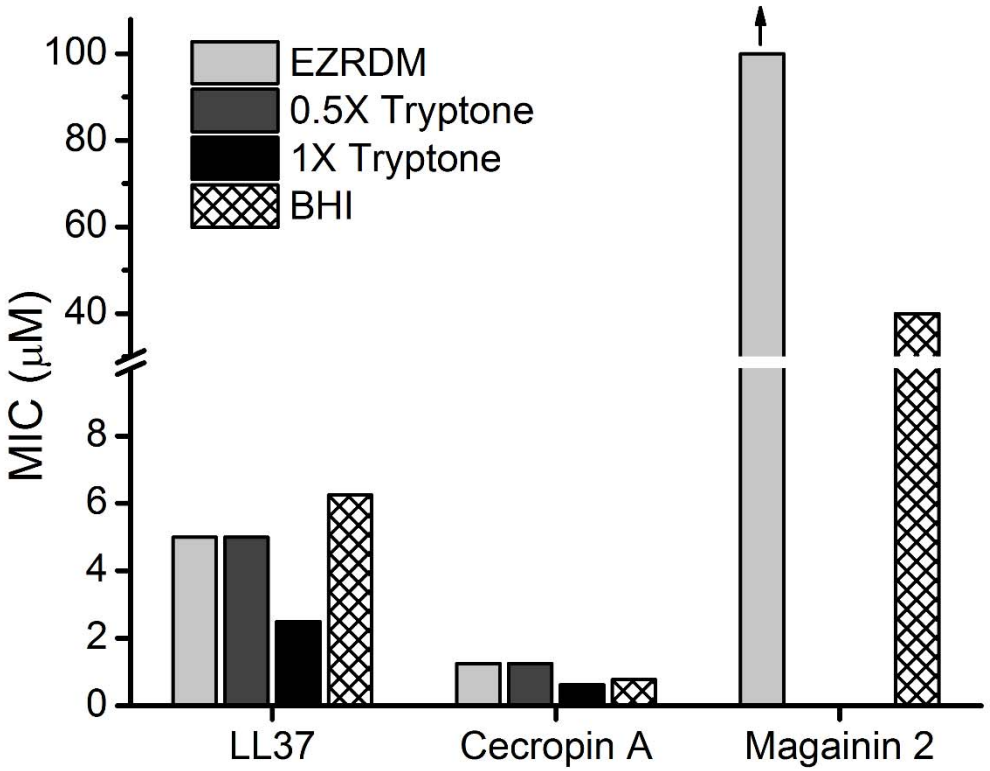

Figure 5.3 Minimum inhibitory concentrations (MICs) of three natural antimicrobial peptides, LL-37, Cecropin A, and Magainin 2, in different media. EZRDM and BHI as described in text. See **Figure 5.5** for sequences of the antimicrobial peptides. Note break in vertical scale for Magainin 2. The designations "EZ + 0.5X tryptone" and "EZ + 1X tryptone" refer to EZRDM supplemented with 5 g/L, and 10 g/L of dialyzed tryptone powder, respectively. Vertical arrow marks a bar that is a lower limit only.

Sequence of Bovine Beta-Casein

MKVLILACLV ALALARELEE LNVPGEIVES LSSSEESITR INKKIEKFQS EEQQQTEDEL

QDKIHPFAQT QSLVYPFPGP IPNSLPQNIP PLTQTPVVVP PFLQPEVMGV SKVKEAMAPK

HKEMPFPKYP VEPFTESQSL TLTDVENLHL PLPLLQSWMH QPHQPLPPTV MFPPQSVLSL

SQSKVLPVPQ KAVPYPQRDM PIQAFLLYQE PVLGPVRGPF PIIV

Hypothetical Digestion of Bovine Beta-Casein with Trypsin

Sequence	Charge
K	+1
R	+1
VK	+1
HK	+1
INK	+1
IEK	0
E**AMA**PK	0
GP**F**P**II**V	0
E**M**P**F**PK	0
VLP**V**PQK	+1
AVP**Y**PQR	+1
FQSEEQQQTEDE**L**QDK	-5
D**M**PIQ**AFLLY**QEP**VL**GP**V**R	-1
E**L**EE**L**N**V**PGE**IV**ES**L**SSSEES**I**TR	-6
IHP**FA**QTQS**LVY**P**F**PGP**I**PNS**L**PQN**I**PP**L**TQTP**VVV**PP**FL**QPE**VM**G**V**SK	0
YP**V**EP**F**TESQS**L**T**L**TD**V**EN**L**H**L**P**L**P**LL**QS**WM**HQPHQP**L**PPT**VMF**PPQS**VL**S**L**SQSK	-3

Figure 5.4 Sequence of bovine beta-casein and of the predicted components of complete digestion of bovine β-casein with trypsin. Red, blue, and bold-black letters denote anionic, cationic, and hydrophobic residues, respectively. Net charges as shown.

Figure 5.5 Sequences of the natural AMPs LL-37, Cecropin A, and Magainin 2. Red, blue, and bold-black letters denote anionic, cationic, and hydrophobic residues, respectively.

Appendix

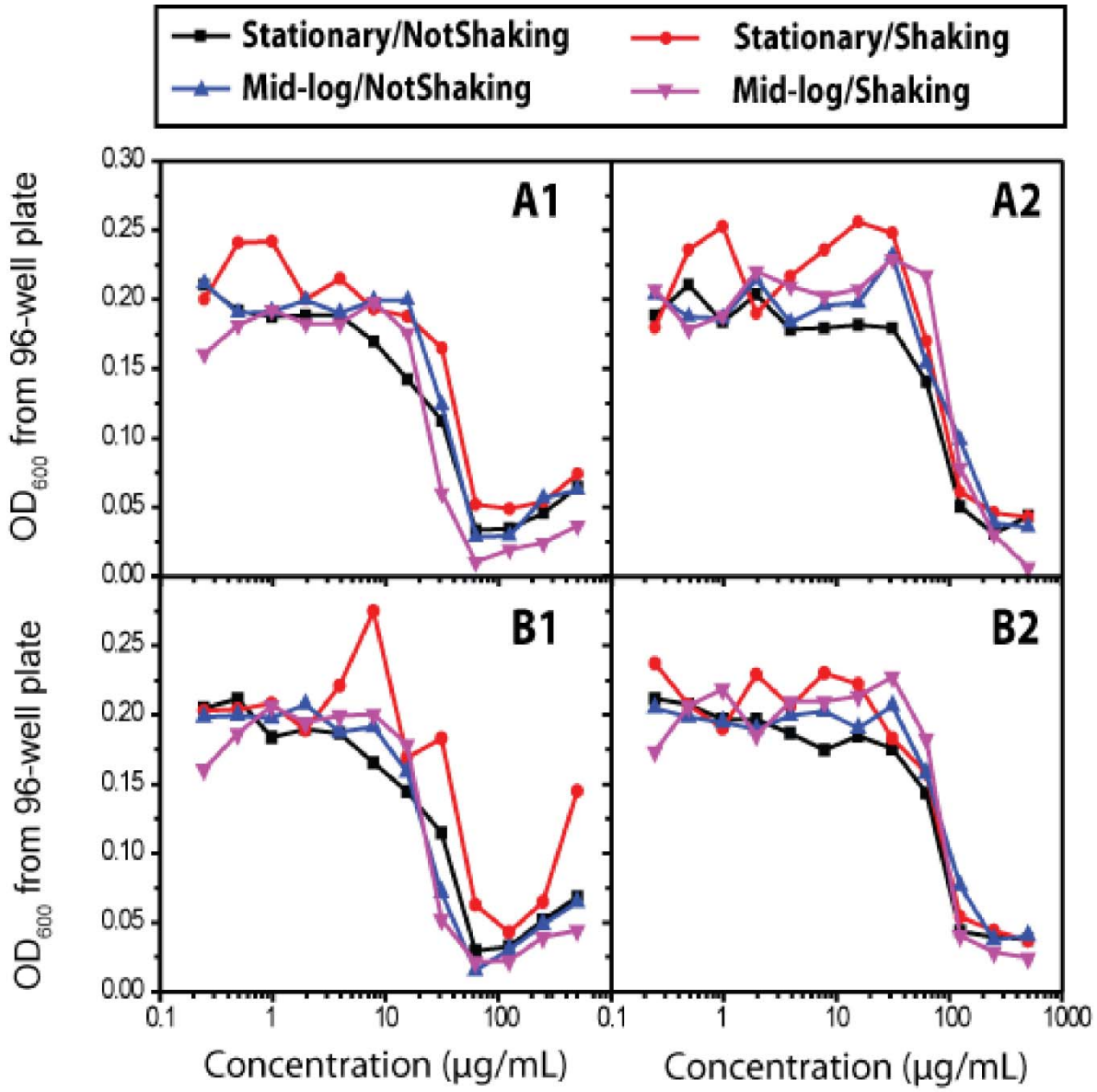

Appendix 5A. Optical density (O.D.) vs concentrations of two different batches of polymers in BHI medium.

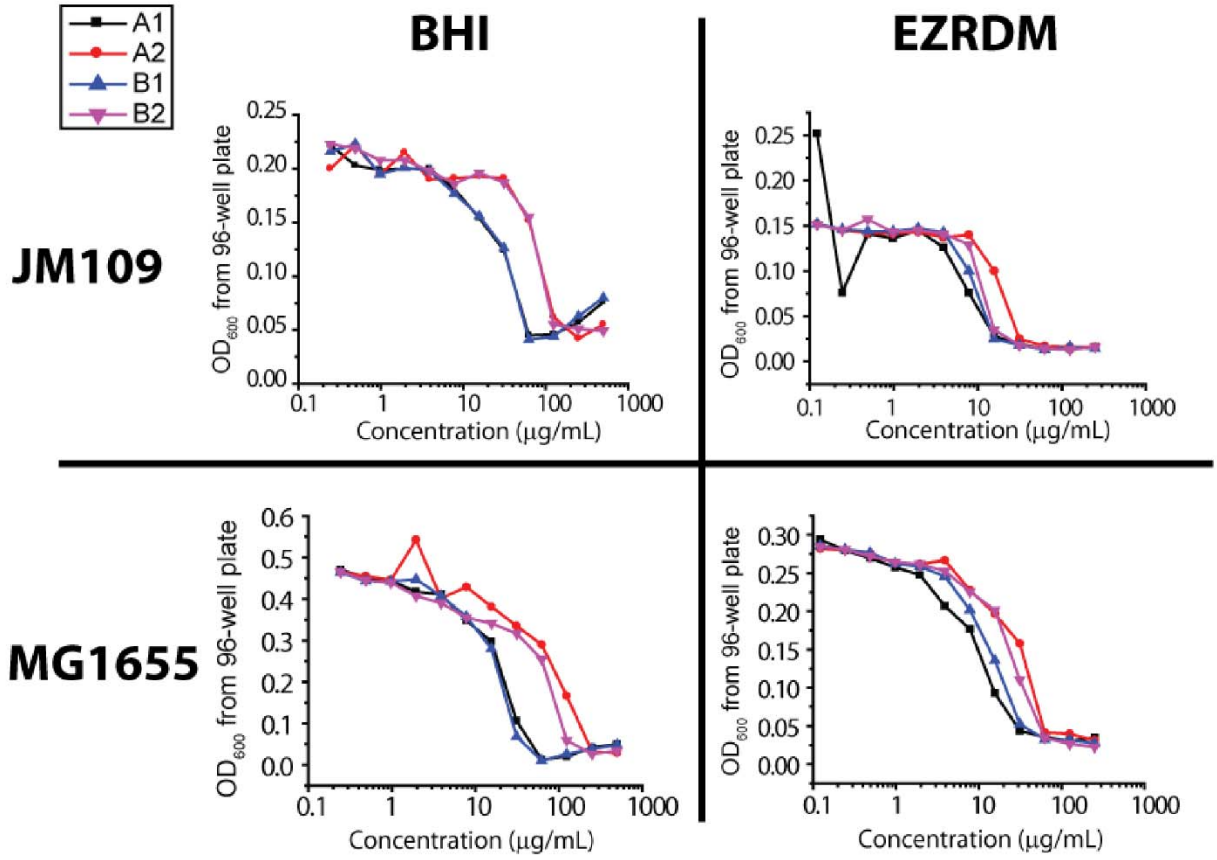

Appendix 5B. Optical density (O.D.) vs concentration compared for two different media and two different *E. coli* strains.

A.

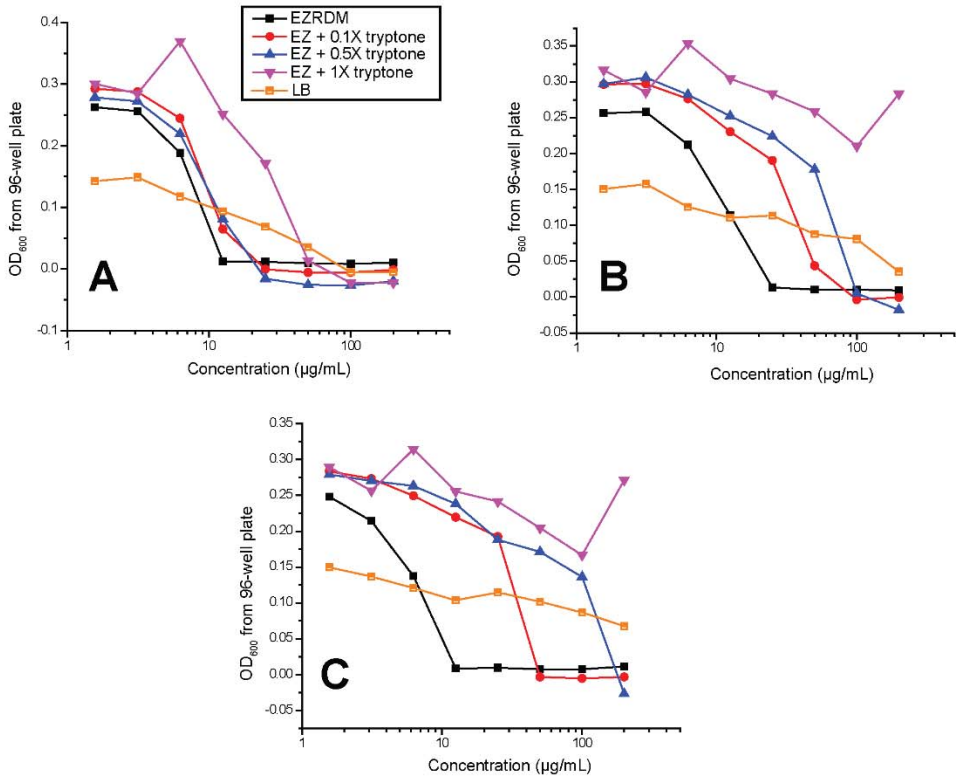

B.

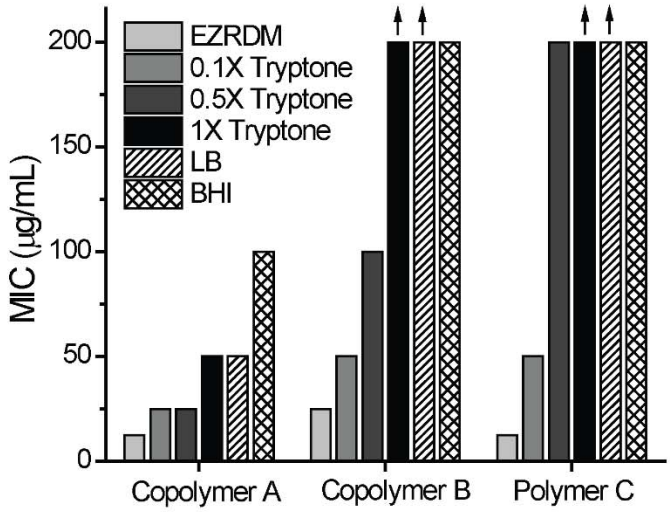

Appendix 5C. Optical density (O.D.) vs concentration of polymers **A**, **B**, and **C**, and **D** in different media.

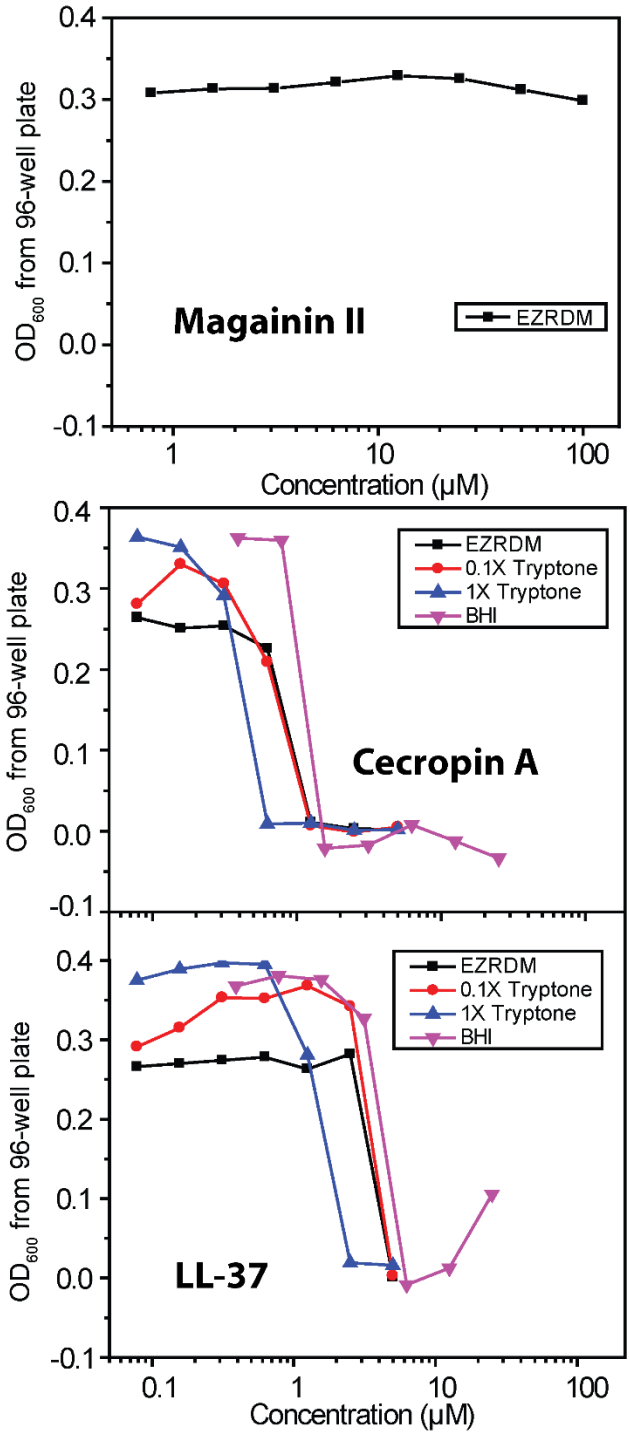

Appendix 5D. Optical density (O.D.) vs concentration of natural antimicrobial peptides Magainin 2, Cecropin A, and LL-37 for different media.

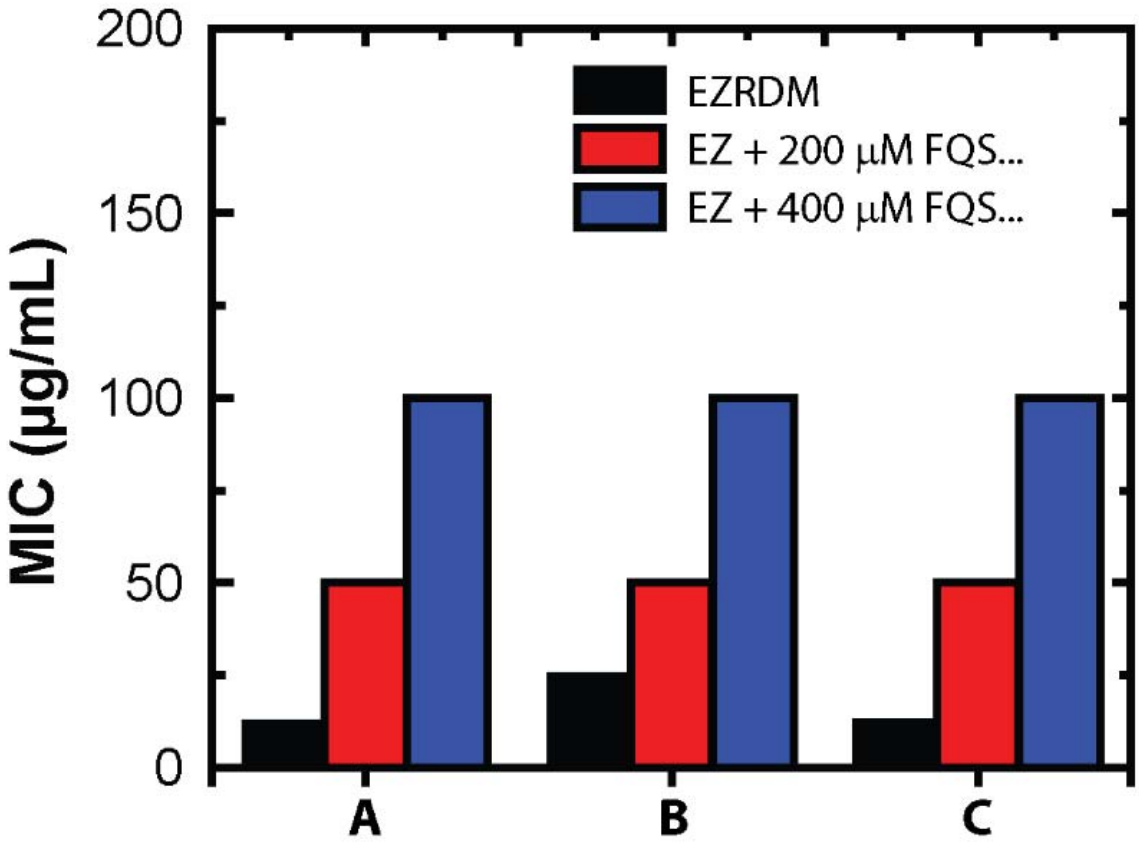

Appendix 5E. Minimum inhibitory concentrations (MICs) of nylon-3 polymers **A**, **B**, and **C** in EZRDM supplemented with 200 µM and 400 µM of the anionic peptide FQSEEQQTEDELQDK.

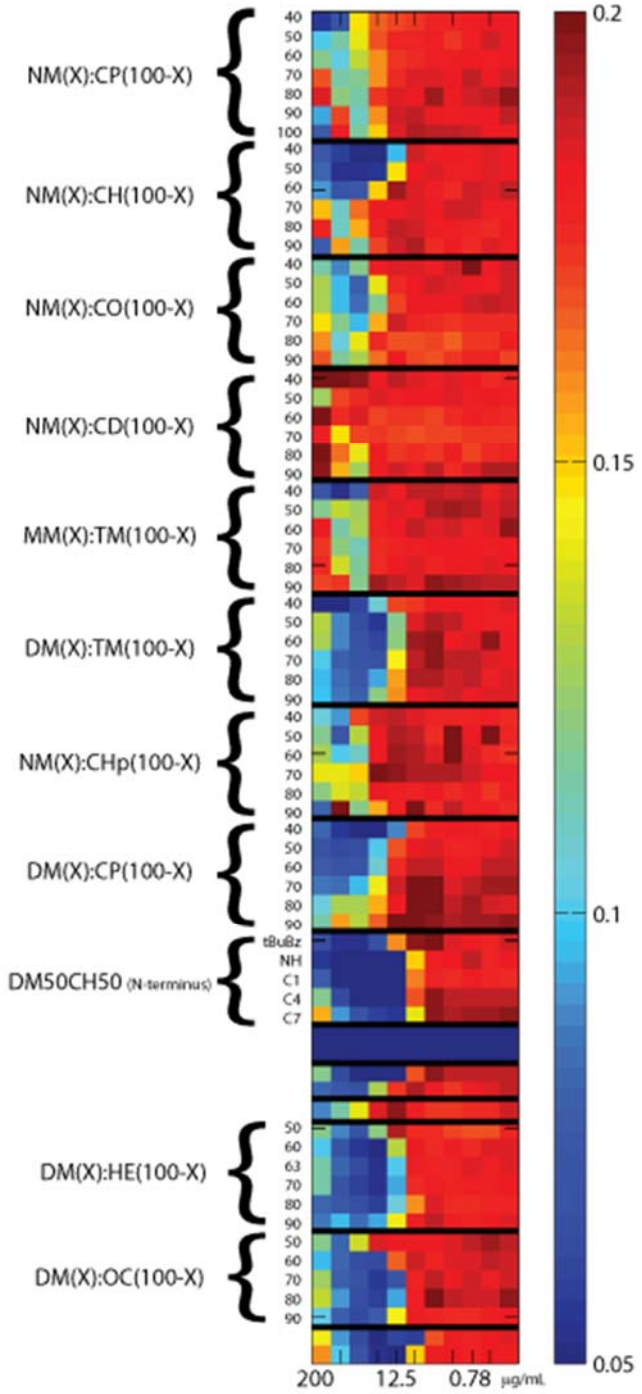

Appendix 5F. Minimum inhibitory concentrations (MICs) of series nylon-3 polymers in BHI.

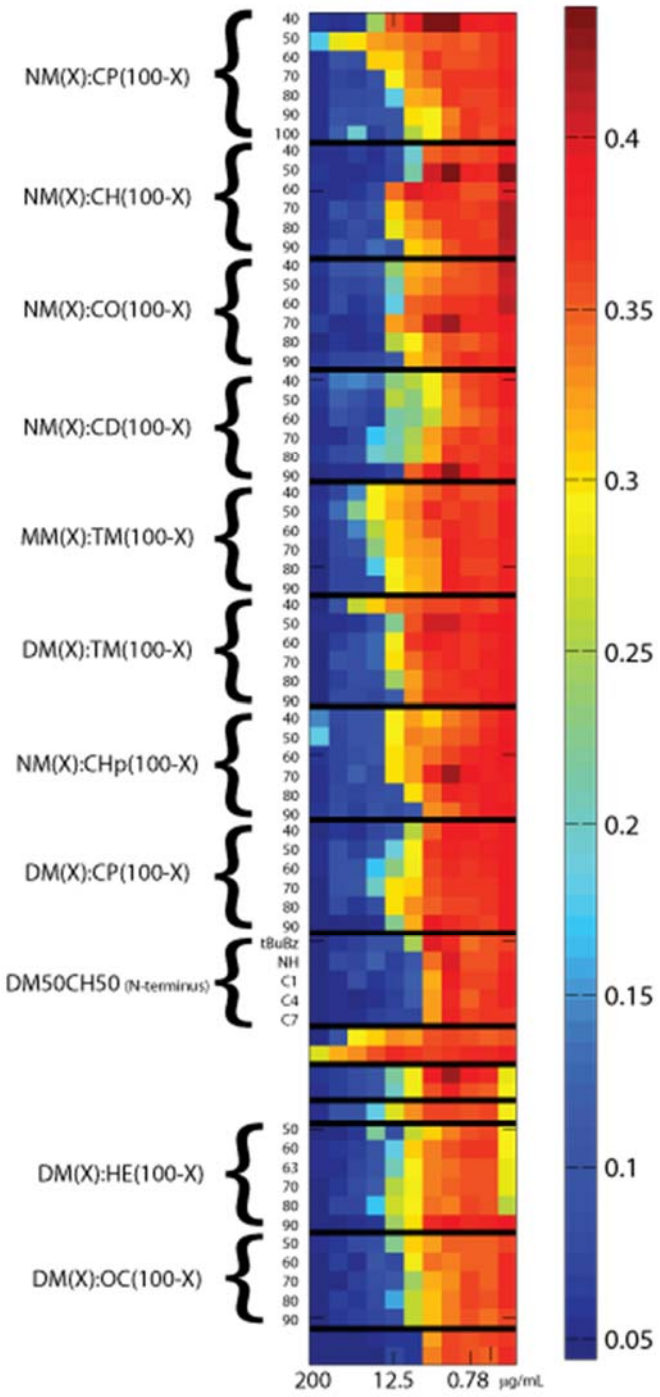

Appendix 5G.. Minimum inhibitory concentrations (MICs) of series nylon-3 polymers in EZRDM.

REFERENCES

1. (a) Hancock, R. E. W.; Sahl, H.-G., Antimicrobial and host-defense peptides as new anti-infective therapeutic strategies. *Nat Biotech* **2006,** *24* (12), 1551-1557; (b) Coates, A.; Hu, Y. M.; Bax, R.; Page, C., The future challenges facing the development of new antimicrobial drugs. *Nat. Rev. Drug Discov.* **2002,** *1* (11), 895-910.

2. (a) Brogden, K. A., Antimicrobial peptides: pore formers or metabolic inhibitors in bacteria? *Nat Rev Micro* **2005,** *3* (3), 238-250; (b) Yeaman, M. R.; Yount, N. Y., Mechanisms of antimicrobial peptide action and resistance. *Pharmacol. Rev.* **2003,** *55* (1), 27-55; (c) Zasloff, M., Antimicrobial peptides of multicellular organisms. *Nature* **2002,** *415* (6870), 389-395.

3. Zhao, X.; Wu, H.; Lu, H.; Li, G.; Huang, Q., LAMP: A Database Linking Antimicrobial Peptides. *Plos One* **2013,** *8* (6).

4. (a) Spindler, E. C.; Hale, J. D. F.; Giddings, T. H., Jr.; Hancock, R. E. W.; Gill, R. T., Deciphering the Mode of Action of the Synthetic Antimicrobial Peptide Bac8c. *Antimicrobial Agents and Chemotherapy* **2011,** *55* (4), 1706-1716; (b) Munk, J. K.; Uggerhoj, L. E.; Poulsen, T. J.; Frimodt-Moller, N.; Wimmer, R.; Nyberg, N. T.; Hansen, P. R., Synthetic analogs of anoplin show improved antimicrobial activities. *Journal of peptide science : an official publication of the European Peptide Society* **2013,** *19* (11), 669-75.

5. (a) Goodson, B.; Ehrhardt, A.; Ng, S.; Nuss, J.; Johnson, K.; Giedlin, M.; Yamamoto, R.; Moos, W. H.; Krebber, A.; Ladner, M.; Giacona, M. B.; Vitt, C.; Winter, J., Characterization of novel antimicrobial peptoids. *Antimicrobial Agents and Chemotherapy* **1999,** *43* (6), 1429-1434; (b) Patch, J. A.; Barron, A. E., Helical peptoid mimics of magainin-2 amide. *Journal of the American Chemical Society* **2003,** *125* (40), 12092-12093; (c) Chongsiriwatana, N. P.; Patch, J. A.; Czyzewski, A. M.; Dohm, M. T.; Ivankin, A.; Gidalevitz, D.; Zuckermann, R. N.; Barron, A.

E., Peptoids that mimic the structure, function, and mechanism of helical antimicrobial peptides. *Proceedings of the National Academy of Sciences of the United States of America* **2008,** *105* (8), 2794-2799.

6. (a) Porter, E. A.; Wang, X.; Lee, H. S.; Weisblum, B.; Gellman, S. H., Non-haemolytic beta-amino-acid oligomers. *Nature* **2000,** *404* (6778), 565; (b) Godballe, T.; Nilsson, L. L.; Petersen, P. D.; Jenssen, H., Antimicrobial beta-Peptides and alpha-Peptoids. *Chemical Biology & Drug Design* **2011,** *77* (2), 107-116.

7. (a) Tiller, J. C.; Liao, C. J.; Lewis, K.; Klibanov, A. M., Designing surfaces that kill bacteria on contact. *Proceedings of the National Academy of Sciences of the United States of America* **2001,** *98* (11), 5981-5985; (b) Lewis, K.; Klibanov, A. M., Surpassing nature: rational design of sterile-surface materials. *Trends in Biotechnology* **2005,** *23* (7), 343-348; (c) Sellenet, P. H.; Allison, B.; Applegate, B. M.; Youngblood, J. P., Synergistic activity of hydrophilic modification in antibiotic polymers. *Biomacromolecules* **2007,** *8* (1), 19-23; (d) Allison, B. C.; Applegate, B. M.; Youngblood, J. P., Hemocompatibility of hydrophilic antimicrobial copolymers of alkylated 4-vinylpyridine. *Biomacromolecules* **2007,** *8* (10), 2995-2999; (e) Sambhy, V.; Peterson, B. R.; Sen, A., Antibacterial and hemolytic activities of pyridinium polymers as a function of the spatial relationship between the positive charge and the pendant alkyl tail. *Angew. Chem.-Int. Edit.* **2008,** *47* (7), 1250-1254; (f) Mowery, B. P.; Lindner, A. H.; Weisblum, B.; Stahl, S. S.; Gellman, S. H., Structure-activity Relationships among Random Nylon-3 Copolymers That Mimic Antibacterial Host-Defense Peptides. *Journal of the American Chemical Society* **2009,** *131* (28); (g) Chakraborty, S.; Liu, R.; Lemke, J. J.; Hayouka, Z.; Welch, R. A.; Weisblum, B.; Masters, K. S.; Gellman, S. H., Effects of Cyclic vs Acyclic Hydrophobic Subunits on the Chemical Structure and Biological Properties of Nylon-3 Copolymers. *Acs*

Macro Letters **2013,** *2* (8), 753-756; (h) Takahashi, H.; Palermo, E. F.; Yasuhara, K.; Caputo, G. A.; Kuroda, K., Molecular design, structures, and activity of antimicrobial peptide-mimetic polymers. *Macromolecular bioscience* **2013,** *13* (10), 1285-99; (i) Kuroda, K.; Caputo, G. A., Antimicrobial polymers as synthetic mimics of host-defense peptides. *Wiley interdisciplinary reviews. Nanomedicine and nanobiotechnology* **2013,** *5* (1), 49-66.

8. (a) Sochacki, K. A.; Barns, K. J.; Bucki, R.; Weisshaar, J. C., Real-time attack on single Escherichia coli cells by the human antimicrobial peptide LL-37. *Proceedings of the National Academy of Sciences of the United States of America* **2011,** *108* (16), E77-E81; (b) Barns, K. J.; Weisshaar, J. C., Real-time attack of LL-37 on single Bacillus subtilis cells. *Biochimica Et Biophysica Acta-Biomembranes* **2013,** *1828* (6), 1511-1520; (c) Rangarajan, N.; Bakshi, S.; Weisshaar, J. C., Localized permeabilization of E. coli membranes by the antimicrobial peptide Cecropin A. *Biochemistry* **2013,** *52* (38), 6584-94.

9. Bakshi, S.; Bratton, B. P.; Weisshaar, J. C., Subdiffraction-Limit Study of Kaede Diffusion and Spatial Distribution in Live Escherichia coli. *Biophysical Journal* **2011,** *101* (10).

10. Sugimura, K.; Nishihara, T., PURIFICATION, CHARACTERIZATION, AND PRIMARY STRUCTURE OF ESCHERICHIA-COLI PROTEASE-VII WITH SPECIFICITY FOR PAIRED BASIC RESIDUES - IDENTITY OF PROTEASE-VII AND OMPT. *Journal of Bacteriology* **1988,** *170* (12), 5625-5632.

11. Bryan, L. E., *Antimicrobial drug resistance*. Academic Press: Orlando, 1984; p xviii, 576 p.

12. Lewenza, S., Extracellular DNA-induced antimicrobial peptide resistance mechanisms in Pseudomonas aeruginosa. *Frontiers in microbiology* **2013,** *4*, 21-21.

13. (a) Wesolowski, D.; Alonso, D.; Altman, S., Combined effect of a peptide-morpholino oligonucleotide conjugate and a cell-penetrating peptide as an antibiotic. *Proceedings of the National Academy of Sciences of the United States of America* **2013,** *110* (21), 8686-8689; (b) Schwab, U.; Gilligan, P.; Jaynes, J.; Henke, D., In vitro activities of designed antimicrobial peptides against multidrug-resistant cystic fibrosis pathogens. *Antimicrobial Agents and Chemotherapy* **1999,** *43* (6), 1435-1440.

14. Hiraki, J.; Ichikawa, T.; Ninomiya, S.; Seki, H.; Uohama, K.; Kimura, S.; Yanagimoto, Y.; Barnett, J. W., Use of ADME studies to confirm the safety of epsilon-polylysine as a preservative in food. *Regulatory Toxicology and Pharmacology* **2003,** *37* (2), 328-340.

15. Yoshida, T.; Nagasawa, T., epsilon-Poly-L-lysine: microbial production, biodegradation and application potential. *Applied Microbiology and Biotechnology* **2003,** *62* (1), 21-26.

16. Shima, S.; Matsuoka, H.; Iwamoto, T.; Sakai, H., ANTIMICROBIAL ACTION OF EPSILON-POLY-L-LYSINE. *Journal of Antibiotics* **1984,** *37* (11), 1449-1455.

17. Vaara, M., AGENTS THAT INCREASE THE PERMEABILITY OF THE OUTER-MEMBRANE. *Microbiol. Rev.* **1992,** *56* (3), 395-411.

18. Wimley, W. C., Describing the mechanism of antimicrobial peptide action with the interfacial activity model. *ACS Chem Biol* **2010,** *5* (10), 905-17.

19. (a) Yoon, H.; McDermott, J. E.; Porwollik, S.; McClelland, M.; Heffron, F., Coordinated Regulation of Virulence during Systemic Infection of Salmonella enterica Serovar Typhimurium. *Plos Pathogens* **2009,** *5* (2); (b) Kim, K. S.; Rao, N. N.; Fraley, C. D.; Kornberg, A., Inorganic polyphosphate is essential for long-term survival and virulence factors in Shigella and Salmonella spp. *Proceedings of the National Academy of Sciences of the United States of America* **2002,** *99* (11), 7675-7680.

Chapter 6

Direct Observation of the Antimicrobial Effects of a Highly Cationic, Random Nylon-3 Copolymer on Live *E. coli*

Submitted as:

Choi H., Chakraborty S., Liu R., Gellman S.H., Weisshaar J.C. "Direct Observation of the Antimicrobial Effects of a Highly Cationic, Random Nylon-3 Copolymer on Live *E. coli*.".

* Nylon-3 copolymers are synthesized by Saswata Chakraborty and Runhui Liu.

Abstract

Synthetic random copolymers based on the nylon-3 (β-peptide) backbone show promise as antimicrobial agents that can be produced inexpensively and are resistant to proteolysis. We present a time-resolved observational study of the attack of a particular copolymer **MM_{63}:CHx_{37}** on single, live *E. coli* cells. The composition and chain length of **MM_{63}:CHx_{37}** (63% cationic subunits, 37% hydrophobic subunits, 35-unit average length) was optimized to enhance antibacterial activity while minimizing hemolysis of red blood cells. For *E. coli* cells that export GFP to the periplasm, we obtain alternating phase contrast and green fluorescence images with 12 s time resolution over 60 min following initiation of copolymer flow. Within seconds, cells shrink and exhibit the same plasmolysis spaces that follow an abrupt external osmotic upshift. The osmoprotection machinery attempts to regain cytoplasmic water, but recovery is interrupted by permeabilization of the cytoplasmic membrane (CM) to GFP. Remarkably, the highly cationic copolymer has evidently translocated across the outer membrane (OM) very rapidly without permeabilizing it to GFP. The CM permeabilization event is spatially localized. Cells whose CM has been permeabilized never recover growth. The minimum inhibitory concentration (MIC) for cells lacking the osmolyte importer ProP is fourfold smaller than for normal cells, suggesting that osmoprotection is an important survival strategy. In addition, at the time of CM permeabilization we observe evidence of oxidative stress. The MIC in anaerobic conditions is at least eight-fold larger than in aerobic conditions. Once the copolymer reaches the periplasm, multiple growth-halting mechanisms proceed in parallel.

Introduction

There is a profound and widely recognized need for new molecular strategies to combat pathogenic bacteria.[1,2] Such strategies include drugs for systemic use in patients (delivered either orally or by injection), agents that act at interfaces between the human body and the external world, and materials that can disinfect environmental surfaces (e.g., in hospitals). Humans and other multicellular organisms have evolved distinctive defense mechanisms at interfaces with the external world, such as skin and the GI tract. In particular, a wide range of small and medium-sized polypeptides can exert broad-spectrum antibacterial activity via multiple mechanisms.[3-6] One common mechanistic theme among these antimicrobial peptides (AMPs) involves disruption of bacterial membranes, a mode of action that seems to make it difficult for microbes to evolve resistance. Membrane-active AMPs are generally selective for bacterial cell membranes relative to host cell membranes, based on charge differences at the cell surfaces. The peptides usually bear net positive charge, and the outer surfaces of bacterial cells have a substantial negative charge density, while the outer surfaces of eukaryotic cells tend more toward electroneutrality.

In earlier work, we tested the unorthodox hypothesis that the biological activity profile of AMPs may not depend on a defined subunit sequence. We have identified multiple examples of sequence-random nylon-3 copolymers (β-peptide backbone) that mimic AMPs in inhibiting bacterial growth while displaying little propensity to lyse human red blood cells ("hemolysis").[7-12] Because sequence-random copolymers are much easier to produce than are sequence-specific peptides or other oligomers, it is conceivable that nylon-3 materials could be developed for clinical applications involving interfaces between the human body and the environment.

In parallel, we have developed unique, single-cell fluorescence imaging assays that monitor in real time key mechanistic events during the attack of AMPs on live *E. coli* and *B. subtilis*.[13-18]

These events include the translocation of an AMP across the outer membrane (OM), permeabilization of the cytoplasmic membrane (CM), the onset of osmotic and oxidative stress, and the halting of growth. Here we apply those mechanistic assays to the attack of a promising nylon-3 copolymer **MM_{63}:CHx_{37}** (**Figure 6.1**) on live *E. coli*. In earlier work, it displayed high antimicrobial activity against a panel of bacterial species and also low hemolytic activity against red blood cells.[10] **MM_{63}:CHx_{37}** is copolymerized from monomethyl beta lactam (**MMβ**) and cyclohexyl beta lactam (**CHxβ**) monomers, mixed in molar ratio of 63:37. Within the polymeric product, the subunit **MM** has a free amine group at its α-carbon and carries a positive charge at physiological pH. On the other hand, the subunit **CHx** contains a hydrophobic cyclohexyl group. Recent studies on the polymer showed bacterial membrane disruption upon the polymer treatment,[11,19] but the mechanistic details of how the polymer acts on live cells have not been characterized.

Remarkably, at a concentration of 1.2X the minimum inhibitory concentration (MIC), the highly cationic copolymer translocates across the *E. coli* OM within seconds, inducing hyperosmotic shock to the cell and abruptly halting growth. Subsequent permeabilization of the CM is concurrent with the apparent onset of oxidative stress. While we have observed analogous symptoms during the attack of natural and synthetic AMPs on *E. coli*,[13,15,17,18] the facility with which the nylon-3 copolymer crosses the outer membrane without permeabilizing it to GFP is unique in our experience. Unlike the previously studied natural AMPs LL-37 and Cecropin A, the copolymer never permeabilizes the outer membrane (OM) to GFP over the 50-min observation period. Once the copolymer reaches the periplasm at sufficiently high concentration, multiple growth-halting effects evidently occur in parallel, as described in detail below.

Experimental Section

Bacterial Strains, Growth Conditions, and Materials

The nylon-3 copolymer used in this study (**Figure 6.1**) is designated **MM_{63}:CHx_{37}**. It comprises a random sequence of 37% hydrophobic subunits (cyclohexyl group connecting C_α and C_β, **CHx**) and 63% hydrophilic subunits (methyl group at C_β and protonated methylamino group at C_α, **MM**). Copolymers were synthesized as before from racemic β-lactams, making each polymer heterochiral. Polymer samples had average chain length of 35 subunits. Polydispersity index (PDI) values ranged from 1.02–1.15.

Four *E. coli* strains were used (**Table 6.1**). The background strain of *E. coli* (wild type, denoted strain "WT") is MG1655 in all cases. The doubling time of MG1655 in EZRDM at 30°C was 50 min. For experiments on cells that export GFP to the periplasm (strain "WT-ppGFP"), TorA-GFP was expressed from the plasmid pJW1 as previously described.[20] The plasmid carries the gene for GFP with the twin-arginine-translocase (TAT) signal peptide appended to its N-terminus. TAT recognizes the signal peptide and exports the properly folded GFP to the periplasm, where it can freely diffuse. This strain had a doubling time of 51 min. To construct a deletion mutant strain lacking the osmoprotectant importer ProP (strain "Δ*proP*"), we obtained strain JW4072 from the KEIO collection.[21] We transduced the kanamycin resistance gene in JW4072 that is in place of *pro*P into our background strain MG1655 via P1 transduction. The doubling time of this strain was 50 min. To visualize the permeabilization of membranes in Δ*proP*, we transformed pJW1 into Δ*proP* and expressed periplasmic GFP using the same protocol (strain "Δ*proP*-ppGFP"). The doubling time of Δ*proP*-ppGFP was again 50 min.

Bulk cultures were grown in EZ rich, defined medium (EZRDM),[22] which contains a MOPS-buffered solution supplemented with metal ions (M2130; Teknova), glucose (2 mg/mL), amino

acids and vitamins (M2104; Teknova), nitrogenous bases (M2103; Teknova), 1.32 mM K_2HPO_4, and 76 mM NaCl. Cultures were grown from glycerol frozen stock to stationary phase overnight at 30°C. Subcultures were grown to exponential phase (OD = 0.2–0.6 at 600 nm) before sampling for the microscopy experiments at 30°C, unless otherwise specified.

Minimum Inhibitory Concentration (MIC) assay

The MIC for **MM_{63}:CHx_{37}** against the strains WT and Δ*proP* was determined using a broth microdilution method as previously described.[23] Two-fold serial dilutions of **MM_{63}:CHx_{37}** in EZRDM were performed in separate rows of a polystyrene 96-well plate with each well containing an inoculum of the *E. coli* strain. The inoculum was a 1:20 dilution from a stationary culture grown at 30°C. The plate was incubated at 30°C for 6 hr for aerobic MIC measurements. The MIC values were taken as the lowest concentration for which no growth was discernible (<0.05 OD) after 6 hr. The aerobic MIC value against WT cells was 25 μg/mL. The molecular weight of an "average" copolymer (35 subunits long, 37% **CHx**, 63% **MM** sidechains) would be ~6.5 kDa. Thus an MIC of 25 μg/mL corresponds to a molar concentration of about 4 μM. We repeated the same MIC assay on the Δ*proP* strain and obtained the value 6.25 μg/mL, four times smaller than the MIC of the WT strain. In anaerobic conditions,[13] the MIC value for the WT strain was >200 μg/mL, at least 8 times higher than in aerobic conditions.

Microfluidics Chamber for Time-Lapse Measurement

Imaging of individual cells was carried out at 30°C in a simple microfluidics chamber consisting of a single rectilinear channel of uniform height of 50 μm and width of 6 mm, with a channel length of 11 mm.[13] The total chamber volume is ~10 μL. The negative of the cell design was patterned onto a silicon wafer via photolithography and the wafer was silanized. Sylgard 184

silicone elastomer mixture (Dow Corning) was poured onto the patterned silicon wafer and baked for 30 min in a 110°C oven after removing air in a vacuum desiccator. The cured polydimethylsiloxane (PDMS) slab was removed and holes were punched for entry and exit hypodermic needles. The patterned PDMS slab was fused to a dried, acetone-cleaned, 22-mm × 40-mm glass coverslip pre-cleaned by plasma oxidation. Soon after the bonding of the two pieces, 0.01% poly-*L*-lysine (molecular weight >150,000 Da) was injected into the chamber for 30 min and then rinsed thoroughly with Millipore water. For imaging experiments, the chamber was maintained at 30°C with a TC-344B dual automatic temperature controller through the CC-28 cable assembly attached to RH-2 heater blocks (Warner Instruments).

Microscopy

Single-cell imaging was performed on a Nikon Eclipse Ti inverted microscope with a 100X, 1.45 N.A. phase contrast objective (Nikon), using epi illumination. An optically pumped semiconductor laser (Coherent) at 488 nm was expanded to illuminate the field of view uniformly. The laser intensity at the sample was ~5 W/cm^2. Fluorescence images were obtained with an EMCCD camera, either Andor iXon 897 or Andor iXon 887. The pixel size corresponds to 160 ± 10 nm at the sample. GFP fluorescence was imaged using the emission filter ET525/50M (Chroma).

The sequence of membrane permeabilization events caused by the copolymer can be monitored by changes in the intensity and spatial distribution of periplasmic GFP over time.[13,17,18] For the microscopy experiments on WT-ppGFP cells, we used 30 μg/mL of **MM_{63}:CHx_{37}** (1.2X WT MIC). A value slightly larger than the MIC was used to account for possible errors in the MIC assay. WT-ppGFP cells were injected into the microfluidics chamber. The base of the chamber was coated with poly-L-lysine to immobilize the cells. The immobilized

cells were then observed in continuously refreshed, aerated medium for 5 min to ensure that the cells are growing properly prior to the injection of **MM_{63}:CHx_{37}**. On excitation at 488 nm, the resulting image of the cells exhibits a halo of green fluorescence, indicating a predominantly periplasmic spatial distribution of GFP (**Figure 6.2A**).

The fluorescence images are interleaved with phase contrast images every 6 s (total imaging cycle time of 12 s). The phase contrast images are used to measure cell length vs time to a precision of ±50 nm. Cell length is affected both by genuine growth and by osmotic effects, as described below. The method of cell length measurement was described previously.[13]

To test for oxidative stress, we added copolymer plus the permeable, oxidation-sensitive dye CellROX Green.[13] Reduced CellROX (as added) is a membrane permeable profluorophore with weak fluorescence. *In vitro*, oxidation of CellROX by the powerful oxidants superoxide (O_2^-) or hydroxyl radical (•OH) in the presence of ds-DNA induces strong CellROX fluorescence (excited at 488 nm and detected at 525 ± 25 nm). The weaker oxidant H_2O_2 does not induce CellROX fluorescence. The affinity of CellROX for DNA prevents the dye from escaping after permeabilization of the bacterial membranes, enabling us to detect oxidative damage inside of single cells. Additional details are provided in our recent study of CM15.[13]

Results

Effects of nylon-3 copolymer on WT-ppGFP cells

At t = 0, we initiated flow of 30 μg/mL of copolymer **MM_{63}:CHx_{37}** (1.2X the WT MIC) into the microfluidics chamber and observed changes in the WT-ppGFP cell length and in the GFP intensity and spatial distribution as a function of time. More than 70 cells were observed over 8 different experimental preparations, with good reproducibility of symptoms vs time. Within 1-2 imaging cycles (12-24 s) after injection, all the cells abruptly begin to shrink in length (**Figure.**

6.2 and **Appendix 6B**; Movie S1). Over the next 1-2 min, additional, less rapid shrinkage occurs until the total cell length has decreased by (9 ± 3)% of the original length. As the shrinkage proceeds, periplasmic GFP intensity gradually accumulates at the two cell poles (**Figure 6.2A**). Evidently the cytoplasm has lost water and transferred part of it to the expanded periplasmic endcaps. We denote the cell shrinkage and "periplasmic bubble" formation events as Phase 1 of the cellular response to the copolymer.

The overall cell shrinkage and the change in the spatial distribution of periplasmic GFP at the end of Phase 1 are highly reminiscent of the effects induced by an abrupt external osmotic upshift.[20,24,25] The periplasmic bubbles are known as plasmolysis spaces. We ascribe the copolymer-induced shrinkage of the cytoplasm to rapid translocation of the highly positively charged copolymer and its many counterions across the OM and into the periplasm. This increases the periplasmic osmolality and draws water from the cytoplasm.

For 80% of the cells, we observed partial recovery of cell length after the shrinkage event (**Figure 6.2C**). We denote this as Phase 2 of the response. As the cells regain length, their periplasmic bubbles shrink measurably. This recovery of length and decrease in bubble volume continues until the moment of permeabilization of the cytoplasmic membrane to GFP. About 20% of the WT-ppGFP cells did not exhibit a discernible Phase 2; imaged with 12-s resolution, they went directly from Phase 1 to Phase 3 (examples in Appendix 6B). CM permeabilization occurred unusually quickly for these cells. We hypothesize that the partial length recovery in Phase 2 is due to the natural osmoprotection response of the cell.[26] In the earliest response, the cell actively imports K^+ and glutamate (Glu^-) in an attempt to retain cytoplasmic water. Later, the cell uses ProP to import neutral osmoprotectants and exports the excess K^+, enabling restoration of growth.

For >85% of the cells, cytoplasmic membrane permeabilization occurred within the 60-min observation time. This is observed as an abrupt transfer of GFP from the periplasm into the cytoplasm (**Figure 6.2A**, **B**). The GFP spatial distribution changes dramatically in just 1-2 imaging cycles (12-24 s). At the same time, we observe a decrease in total GFP fluorescence intensity by 15% (**Figure 6.2C**). This is likely due to the higher pH of the cytoplasm and the known pH sensitivity of GFP fluorescence;[27] see below for further evidence. For a copolymer concentration of 1.2X MIC, after permeabilization of the CM the cell length typically stabilizes at a value ~5% smaller than the original length at $t = 0$. No subsequent cell growth is observed over the 60-min observation period. We define the period after CM permeabilization as Phase 3.

The time at which CM permeabilization occurs varies widely from cell to cell, typically lying in the range $t = 1–20$ min after copolymer injection (Appendix 6B). Complete loss of the GFP signal, which would indicate permeabilization of the OM to GFP, never occurs within the 1-hr observation period. We infer that **MM_{63}:CHx_{37}** can accumulate inside the periplasm without permeabilizing the outer membrane to GFP-size species. The subsequent permeabilization of the CM to GFP should release small molecules (including ATP) to the surround and destroy the proton-motive force. Evidently this halts the osmotic recovery response and ends Phase 2.

Remarkably, a few (<5%) of the cells exhibit several cycles of Phase 1 and Phase 2 prior to CM permeabilization (Appendix 6C and Movie S2). These cells shrink, then recover in length, then shrink and recover again. The periplasmic bubbles form, then deflate, then form and deflate again. The cycles continue until the CM becomes permeabilized. We do not understand this behavior.

Active respiration required for partial length recovery

At 30 μg/mL of **MM_{63}:CHx_{37}** (1.2X WT MIC), during Phase 2 the cells lengthen for a variable amount of time until CM permeabilization occurs. If this partial recovery of cell length is related to active osmoregulation, we reasoned that it should depend on respiration, which maintains the proton-motive force (pmf) and enables biosynthesis of ATP. This in turn allows the cell to import ions (K^+ and Glu^-) and osmoprotectants (Pro and glycine betaine, if present in the medium) into the cytoplasm against the chemical gradient.[28-31]

To test this hypothesis, we pre-treated WT-ppGFP cells with both carbonyl cyanide *m*-chlorophenyl hydrazone (CCCP) at 200 μM and α-deoxyglucose at 1 mM for 10 min prior to the onset of the flow of copolymer. CCCP dissipates the pmf by transporting protons from the periplasm to the cytoplasm.[32] The α-deoxyglucose is imported and blocks normal glycolysis, preventing production of ATP by glycolysis itself.[33] After pre-treatment but prior to injection of 30 μg/mL of **MM_{63}:CHx_{37}**, we observed no growth of the cells, consistent with the halting of active respiration. Then we flowed the copolymer solution over the pretreated cells. Much like the respiring cells (**Figure 6.3A**), the non-respiring cells shrank in length by ~10% and formed periplasmic bubbles (**Figure 6.3B**). Evidently the initial shrinkage (Phase 1) does not require ATP or the pmf, although the shrinkage occurred more slowly in general. Unlike the respiring cells, for the non-respiring cells we observed no recovery of the cell length after the shrinkage; Phase 2 was absent. This is consistent with the osmotic hypothesis. Cell shrinkage does not require active respiration, but the partial recovery of cell length does.

For the non-respiring cells, CM permeabilization again occurred after a variable time lag for >85% of the cells, indicating that active respiration is not required for the CM permeabilization step. In addition, for the non-respiring cells the total GFP fluorescence intensity remained

constant even after GFP had entered the cytoplasm (**Figure 6.3B**). This supports the suggestion that the sudden ~15% decrease in GFP intensity observed in respiring cells is due to equilibration of the pH of the cytoplasm with that of the periplasm.

Import of osmoprotectants required for growth recovery at sub-MIC dosage

Our hypothesis is that entry of the copolymer and its counterions into the periplasm mimics an external osmotic upshift. This should trigger the natural cellular osmoprotection mechanisms, including initial import of K^+ and Glu^- and subsequent import of neutral osmoprotectants such as Pro and glycine betaine (if available) by ProP.[26] If so, then deletion of the gene *proP* should diminish the cell's ability to respond to copolymer attack and recover growth. The channel ProU also uptakes osmoprotectants, but its expression level is low in our medium.[26] Accordingly, we measured the MIC of the Δ*proP* strain after 6 hr of incubation with the copolymer. The result is 6.3 μg/mL (Appendix 6A), a factor of 4 lower than the MIC of wild-type MG1655. This is consistent with the idea that ProP is assisting growth and survival at copolymer concentrations between 6.3 μg/mL and the WT MIC of 25 μg/mL.

Next we performed single-cell, time-lapse microscopy imaging of the WT-ppGFP and the Δ*proP*-ppGFP strain at 15 μg/mL of copolymer. This concentration is well below the MIC of the WT strain (25 μg/mL), but above the MIC of the Δ*proP* strain (6.3 μg/mL). An implicit assumption in the comparison is that the outer membrane composition and structure is unchanged in Δ*proP*, so that the copolymer translocates across the outer membrane with similar efficiency in WT and Δ*proP* strains. Measurement of the relative cell length vs time without injection of the copolymer shows that the Δ*proP* and wild-type MG1655 strains both grow at the same rate.

At $t = 0$, we initiated flow of 15 μg/mL copolymer over WT cells (example in Movie S3). To enable facile comparison among cells of different initial length, in **Figure 6.4A** we plot relative cell length vs time for 20 WT cells, calculated by dividing the cell length at times $t > -5$ min by the length at $t = -5$ min. Immediately after injection, the cells abruptly shrink in length by (5 ± 1)% (**Figure 6.4A**). When tested with WT-ppGFP, we observed periplasmic bubbles that form when the shrinkage occurred. Recall that under 30 μg/mL of **MM_{63}:CHx_{37}**, cells shrank by 10% on average. Evidently the degree of cell shrinkage in Phase 1 increases with the bulk concentration of the copolymer, as seems reasonable for an osmotic effect. However, at 15 μg/mL of copolymer, the majority of the WT cells (>85%) recovered growth a few minutes after the shrinkage event (**Figure 6.4A**). This is evidently real growth, not just an osmotic recovery, because the cell length at $t = 20$ min typically exceeds that at $t = 0$ and is continuing upward. For WT-ppGFP, as the recovering cells lengthen the GFP distribution returns to the normal periplasmic distribution. For all cells that recovered, no CM permeabilization step was observed over the 30 min observation period. In contrast, permeabilization of the CM to GFP (movement of GFP into the cytoplasm) was always observed for the smaller fraction of cells (~15%) that did not recover growth after the initial cell shrinkage. In WT-ppGFP cells at sub-MIC copolymer concentration, the initial osmotic effect is evidently reversible unless CM permeabilization occurs.

We carried out analogous imaging studies after treatment of the Δ*proP* strain with 15 μg/mL of **MM_{63}:CHx_{37}** at $t = 0$ (**Figure 6.4B**). This is more than twice the 6-hr MIC for the Δ*proP* mutant strain. Immediately after the injection, we observed shrinkage of the relative cell length (Phase 1). When tested with Δ*proP*-ppGFP, periplasmic bubbles of GFP at the endcaps formed. The degree of shrinkage (7 ± 2)% is slightly higher than that of WT cells, (5 ± 1)%, suggesting

that the absence of ProP enables the copolymer to induce a larger net osmotic effect. At 15 μg/mL of copolymer, the percentage of the cells that undergo CM permeabilization is similar for the WT-ppGFP strain (14%, $n = 42$) and the Δ*proP*-ppGFP strain (13%, $n = 78$), indicating that the presence or absence of ProP does not influence CM permeabilization. However, unlike wild-type MG1655, a large majority of Δ*proP* cells (~90%) did not return to normal growth over the 30-min observation period.

These data support the hypothesis that in WT cells treated with 15 μg/mL of copolymer, the import of osmoprotectants by ProP enables most cells to recover from the initial osmotic effects. For the Δ*proP* mutant strain, the same osmotic effects are evidently sufficient to halt growth, even when CM permeabilization does not occur.

Cytoplasmic membrane permeabilization localized to one pole

In previous studies with the natural AMPs LL-37[18] and Cecropin A,[17] we observed localized CM permeabilization near the endcaps or the septation site of *E. coli*. We tested whether WT-ppGFP cells under copolymer treatment also exhibit localized CM permeabilization. To enable easy visualization of the diffusive motion of periplasmic GFP at a 10 Hz frame rate, we pre-treated the cells with 60 μg/mL of cephalexin for 30 min. Cephalexin prevents septation, causing the cells to filament without hampering their overall growth. The increased cell length allows accurate monitoring of the changes in GFP spatial distribution after the copolymer treatment.

We initiated flow of the copolymer at 30 μg/mL (1.2X WT-MIC) and observed changes in the GFP spatial distribution, imaging at 10 Hz (0.1 s per camera frame, see Movie S4). As for untreated cells, GFP first accumulates at both poles (periplasmic bubbles). After a lag time of several minutes, GFP abruptly begins to enter the cytoplasm *at one endcap* (**Figure 6.5**). This is

clearly shown by the GFP axial intensity profile vs time. For the typical cell shown, essentially complete drainage of GFP from the endcap near the permeabilization site occurred in ~2 s. Drainage of GFP from the second endcap occurred much more slowly, over ~60 s. Evidently the second endcap drains by diffusion of the GFP along the thin, annular length of the periplasm to the first endcap, the site of permeabilization of the CM. The data thus strongly suggest that the CM permeabilization by the copolymer is localized at one pole. Intriguingly, this also indicates that once permeabilization has occurred near one CM endcap, the other endcap remains intact during the complete redistribution of the GFP signal into the cytoplasm.

Oxidative stress induced when copolymer permeabilizes cytoplasmic membrane

In the previous studies with CM15 and LL-37,[13] formation of reactive oxygen species (ROS) was observed at the time of permeabilization of the cytoplasmic membrane. For CM15, the MIC was 20-fold higher under anaerobic conditions, indicating that ROS formation is an important cause of growth inhibition under aerobic conditions. This may eventually prove to be a fairly general growth-halting mechanism for AMPs in aerobic conditions, but more work is needed. We naturally wondered if nylon-3 copolymers that mimic AMP behavior might also inhibit growth via formation of reactive oxygen species.

To test this hypothesis, we measured the MIC under aerobic and anaerobic conditions (**Table 6.1**). The MIC under anaerobic conditions is at least 8-fold higher. Evidently growth inhibition is oxygen dependent. To further test for ROS formation, we applied the CellROX Green assay to WT cells treated with the copolymer, as described earlier for the AMP CM15.[13] *In vitro*, CellROX Green is selectively oxidized to a fluorescent form CellROX* by reaction with superoxide (O_2^-) or hydroxyl radical (•OH) in the presence of ds-DNA, but not with hydrogen peroxide (H_2O_2). CellROX* fluoresces upon binding to DNA.

At $t = 0$ we initiated flow of aerated EZRDM containing 30 μg/mL of copolymer **MM_{63}:CHx_{37} (**1.2X the WT MIC) plus 2.5 μM of CellROX green across plated WT cells. The subsequent changes in cell length vs time are similar to those without CellROX Green, typically exhibiting three phases (example in **Figure 6.6**). During Phase 1 (cell shrinkage), the CellROX* fluorescence intensity rises slightly (Movie S5). During Phase 2 (osmotic response and partial recovery of the turgor pressure), the CellROX* intensity plateaus. During Phase 3 (after CM permeabilization), much stronger CellROX* intensity rises gradually over a period of 5–10 min. Lacking the periplasmic GFP image, we cannot accurately determine when the cytoplasmic membrane is permeabilized. Based on experiments like that of **Figure 6.2**, we expect that the CM is permeabilized when the cell length recovery ends. If so, then the strong CellROX* signal begins to rise when CM permeabilization occurs, long after the cell shrinkage event. This is similar to the observations for CM15 on *E. coli*.[13]

As a control, we also carried out the CellROX Green assay at 15 μg/mL of **MM_{63}:CHx_{37}** (0.6X the WT MIC, example in **Figure 6.6B**). As in **Figure 6.4**, the cell length shrinks immediately upon injection of the copolymer, and growth resumes after the turgor pressure recovery. The CellROX* intensity again increases slightly during Phase 1 and then plateaus. However, there is no subsequent large increase in CellROX* intensity over the next 20 min. At 1.2X MIC, the mean of the peak CellROX* intensity was 200 ± 50 in arbitrary units (n = 20). At 0.6X MIC, the mean was four times smaller: 50 ± 20 (n = 17). Error estimates are ± one standard deviation of the mean in both cases.

Evidently strong CellROX* fluorescence occurs only for copolymer concentrations sufficiently high to induce CM permeabilization. Combined with the 8-fold increase in MIC

under anaerobic conditions, this strongly suggests that oxidative stress induced by the copolymer is a significant component of the growth-halting mechanism.

Discussion

We have used single-cell, time-lapse microscopy to investigate the mechanisms of the attack of the random copolymer **MM_{63}:CHx_{37}** on live *E. coli* cells. When cells are treated with copolymer at 1.2X the WT MIC, the response of most WT-ppGFP cells comprises three phases. These are depicted schematically in Fig. 7. During Phase 1, we observe cell shrinkage and GFP accumulation at both endcap regions of the periplasm ("periplasmic bubble" formation). In Phase 2, cells recover part of the original length and the periplasmic bubbles shrink. In Phase 3, the cytoplasmic membrane is permeabilized to GFP, which moves inward from the periplasm to the cytoplasm. The recovery in cell length abruptly halts. The gradual onset of strong CellROX* fluorescence begins at the moment of CM permeabilization (**Figure 6.6**), suggesting that the copolymer has induced significant oxidative stress.

The spatial redistribution of periplasmic GFP during Phase 1 is highly reminiscent of the effects of an abrupt external osmotic upshift with an osmolyte that does not permeate the CM, such as NaCl. The periplasmic bubbles are known as plasmolysis spaces.[20] In normal growth conditions, the turgor pressure arises from the larger osmolality of the cytoplasm compared with the periplasm. The excess internal osmotic pressure is balanced by the elastic restoring force of the stretched peptidoglycan layer. External hyperosmotic shock increases the osmolality of the periplasm, causing net transfer of water from cytoplasm to periplasm and the external medium and partial loss of turgor.[20,34] The cytoplasmic membrane accommodates the reduced cytoplasmic volume by collapsing its endcaps, approximately conserving the surface area of the CM. This opens gaps between the CM and OM at the endcaps. The expansion and redistribution

of the periplasmic volume causes freely diffusing molecules like GFP to collect in the endcaps, where most of the periplasmic volume now resides. The result is the observed cell shrinkage and periplasmic GFP bubbles in the endcaps.

We ascribe the copolymer-induced cell shrinkage and periplasmic bubble formation to rapid passage of the highly positively charged copolymer and its counterions across the OM and into the periplasm, mimicking an external osmotic upshift. The driving force is presumably the copolymer concentration gradient across the OM. We can compare the periplasmic GFP images induced by 1.2X WT MIC of the copolymer with those induced by external NaCl in our earlier study of plasmolysis effects.[20] By this measure, the hyperosmotic shock from the copolymer is roughly equivalent to that arising from a moderate external NaCl upshift of ~500 Osm. The Shaevitz lab quantified changes in the *E. coli* cytoplasmic volume, length, and width after external hyperosmostic upshift using a variety of osmolytes.[24] The fractional degree of shrinkage increased with bulk concentration of osmolytes. Similarly, the degree of shrinkage induced by the nylon-3 copolymer increases with bulk concentration of the polymer.

In earlier work, we observed abrupt shrinkage of *E. coli* cell length and partial length recovery after addition of the natural AMPs LL-37 [18] and Cecropin A [17] and of the synthetic AMP CM15.[13] However, the shrinkage typically began 1-2 min after addition of the antimicrobial agent and was not accompanied by formation of plasmolysis spaces. The osmotic effects of the copolymer are evidently much stronger and occur much more rapidly, on a timescale of ~10 s. Evidently at least some components of the random copolymer mixture can penetrate the OM and enter the periplasm readily without permeabilizing the OM to GFP, which is retained in the periplasm. This is remarkable behavior for such a highly cationic species (63% cationic subunits). We speculate that the necessarily unfolded random copolymers may be

threading their way through OM channels, such as TolC or OmpF. These channels are sufficiently large to accommodate an unfolded β-peptide chain. As precedent, we cite the clear structural evidence that the initial stage of attack of various colicins on *E. coli* involves insertion of an unfolded N-terminal region through these same outer membrane channels. Experiments on reconstituted channels[35,36] could test this speculation.

Phase 2 is characterized by partial recovery of the original GFP periplasmic spatial distribution and of the cell length. Evidently the cell is regaining some of the turgor pressure lost during the initial hyperosmotic shock. This phase requires active respiration, as non-respiring cells did not recover in length (**Figure 6.3**). The first response of *E. coli* to hyperosmotic shock is the active import of K^+.[37] This response begins on a sub-minute timescale, so we hypothesize that the partial recovery of turgor pressure is driven primarily by K^+ import. The lack of recovery in non-respiring cells is consistent with this hypothesis, because K^+ import relies on the pmf and ATP.[28-31]As shown by Huang and co-workers,[25] cell wall synthesis and accumulation of peptidoglycan may well continue during hyperosmotic shock. We suggest that "storage" of excess cell wall during Phase 1 may enable the observed abrupt, partial length recovery as the turgor pressure is partially restored and the cell "re-inflates" (Figs. 2 and 3).

The hypothesis that K^+ accumulation underlies the initial length recovery is indirectly supported by the behavior of the mutant Δ*proP* strain. At 0.6X WT MIC, which is more than twice the MIC of the Δ*proP* strain, both WT and Δ*proP* partially recover length at a similar rate for a few minutes after the shrinkage (**Figure 6.4**). Both strains have functional potassium transporters, and the cytoplasmic membrane remains intact throughout. However, only the WT strain subsequently recovers proper growth, achieving lengths greater than that at $t = 0$. The Δ*proP* strain recovers part of its original length but does not achieve normal growth. We

conjecture that the inability to replace K^+ by neutral osmoprotectants prevents a return to normal growth. The resulting "K^+ poisoning" may well prevent proper function of essential biological processes involving protein-nucleic binding, including transcription and translation.[38,39]

Two other osmoprotectant importers, ProU and BetT, are known in addition to ProP.[37] However, these are only expressed significantly in cells adapted for growth in medium of high osmolality, not in our growth conditions. There would not be sufficient time to change the transcription profile before the purported K^+ poisoning event shuts down transcription. As further evidence, when Δ*proP* cells were rinsed in fresh growth medium after treatment with 0.6 WT MIC of copolymer, normal growth did not resume. Evidently these cells have no way of resolving the accumulation of excess K^+.

The onset of Phase 3 is signaled by abrupt permeabilization of the cytoplasmic membrane to periplasmic GFP. The frequency of occurrence of CM permeabilization depends on the bulk concentration of the polymer. At 0.6X WT MIC, we observe CM permeabilization in only 14% of the WT cells, while at 1.2X WT MIC we observe CM permeabilization in >85% of the WT cells. Moreover, this process does not require active respiration or osmoprotectant accumulation by ProP.

The behavior of cephalexin-treated cells shows that the permeabilization event is localized near one cell pole (**Figure 6.5**). The reason is unclear. The cytoplasmic endcaps are known to concentrate anionic lipids, including cardiolipin (CL) and phosphatidylglycerol (PG).[40] The highly cationic copolymer might well interact particularly strongly with these lipids. Why does permeabilization to GFP occur only at one endcap? Substantial turgor pressure still remains just before the CM permeabilization event. One possibility is that this residual turgor pressure assists

the initial permeabilization event. Once GFP-sized species can equilibrate their concentrations across the CM, this residual turgor will diminish further.

For WT cells, permeabilization of the CM to GFP seems to mark the point of no return to normal cell growth. Once CM permeabilization has occurred, we never observe subsequent growth recovery. This is also the moment of onset of strong oxidative stress, as evidenced by the strong concomitant increase in CellROX* fluorescence (**Figure 6.6**). In addition, the MIC increases at least 8-fold in anaerobic conditions. Oxidative damage is evidently a key component of the bacteriostatic potency of the copolymer.

Conclusion

The new data reveal multiple growth-halting effects after addition of the nylon-3 random copolymer **MM_{63}:CHx_{37}** to *E. coli*. On a timescale of seconds, the copolymer readily traverses the OM without permeabilizing it to periplasmic GFP. The evidence from the Δ*proP* mutant strain suggests that the periplasmic osmotic upshift due to the copolymer and its counterions in and of itself would be sufficient to abruptly halt growth were it not for the natural osmotic recovery mechanisms. Cells never return to normal growth after CM permeabilization occurs. This may be due to loss of the pmf, to loss of ATP and other key small molecules to the surround, to the onset of oxidative damage, or to some combination of these effects. It is also important to remember that our observations do not rule out copolymer disruption of other, more specific biochemical processes, such as cell wall biosynthesis or transcription or translation.[5]

The multi-pronged nature of the attack of the nylon-3 copolymer on *E. coli* is reminiscent of the effects of natural and synthetic antimicrobial peptides.[1,41] What distinguishes the copolymer from the AMPs we have studied thus far is its ability to traverse the OM so rapidly, within

seconds of injection. The resulting influx of copolymer and its counterions causes an unusually large and abrupt hyperosmotic upshift within the periplasm. Future work will attempt to understand what specific polymeric properties underlie this ability to translocate across the outer membrane of Gram negative species. That is the key initial step towards effective bacteriostatic action.

References

(1) Hancock, R. E., and Sahl, H. G. (2013) New strategies and compounds for anti-infective treatment, *Curr Opin Microbiol 16*, 519-521.

(2) Afacan, N. J., Yeung, A. T., Pena, O. M., and Hancock, R. E. (2012) Therapeutic potential of host defense peptides in antibiotic-resistant infections, *Curr pharmaceut design 18*, 807-819.

(3) Zasloff, M. (2002) Antimicrobial peptides of multicellular organisms, *Nature 415*, 389-395.

(4) Gallo, R. L., and Hooper, L. V. (2012) Epithelial antimicrobial defence of the skin and intestine, *Nat Rev Immunology 12*, 503-516.

(5) Guilhelmelli, F., Vilela, N., Albuquerque, P., Derengowski Lda, S., Silva-Pereira, I., and Kyaw, C. M. (2013) Antibiotic development challenges: the various mechanisms of action of antimicrobial peptides and of bacterial resistance, *Front Microbiol 4*, 353.

(6) Brogden, K. A. (2005) Antimicrobial peptides: pore formers or metabolic inhibitors in bacteria?, *Nat Rev Micro 3*, 238-250.

(7) Liu, R., Chen, X., Chakraborty, S., Lemke, J. J., Hayouka, Z., Chow, C., Welch, R. A., Weisblum, B., Masters, K. S., and Gellman, S. H. (2014) Tuning the Biological Activity Profile of Antibacterial Polymers via Subunit Substitution Pattern, *JACS 136*, 4410-4418.

(8) Chakraborty, S., Liu, R., Hayouka, Z., Chen, X., Ehrhardt, J., Lu, Q., Burke, E., Yan, Y., Weisblum, B., Wong, G. C. L., Masters, K. S., and Gellman, S. H. (2014) Ternary Nylon-3 Copolymers as Host-Defense Peptide Mimics: Beyond Hydrophobic and Cationic Subunits, *JACS 136*, 14530-14535.

(9) Chakraborty, S., Liu, R., Lemke, J. J., Hayouka, Z., Welch, R. A., Weisblum, B., Masters, K. S., and Gellman, S. H. (2013) Effects of Cyclic vs Acyclic Hydrophobic Subunits on the Chemical Structure and Biological Properties of Nylon-3 Copolymers, *ACS Macro Lett 2*, 753-756.

(10) Mowery, B. P., Lindner, A. H., Weisblum, B., Stahl, S. S., and Gellman, S. H. (2009) Structure-activity Relationships among Random Nylon-3 Copolymers That Mimic Antibacterial Host-Defense Peptides, *JACS 131*, 9735-9745.

(11) Epand, R. F., Mowery, B. P., Lee, S. E., Stahl, S. S., Lehrer, R. I., Gellman, S. H., and Epand, R. M. (2008) Dual Mechanism of Bacterial Lethality for a Cationic Sequence-Random Copolymer that Mimics Host-Defense Antimicrobial Peptides, *J Mol Biol 379*, 38-50.

(12) Mowery, B. P., Lee, S. E., Kissounko, D. A., Epand, R. F., Epand, R. M., Weisblum, B., Stahl, S. S., and Gellman, S. H. (2007) Mimicry of antimicrobial host-defense peptides by random copolymers, *JACS 129*, 15474-15475.

(13) Choi, H., Yang, Z., and Weisshaar, J. C. (2015) Single-cell, real-time detection of oxidative stress induced in *Escherichia coli* by the antimicrobial peptide CM15, *PNAS U.S.A. 112*, E303-E310.

(14) Bakshi, S., Choi, H., Rangarajan, N., Barns, K. J., Bratton, B. P., and Weisshaar, J. C. (2014) Nonperturbative Imaging of Nucleoid Morphology in Live Bacterial Cells during an Antimicrobial Peptide Attack, *Appl Env Microbiol 80*, 4977-4986.

(15) Bakshi, S., Choi, H., Mondal, J., and Weisshaar, J. C. (2014) Time-dependent effects of transcription- and translation-halting drugs on the spatial distributions of the *Escherichia coli* chromosome and ribosomes, *Mol Microbiol 94*, 871-887.

(16) Barns, K. J., and Weisshaar, J. C. (2013) Real-time attack of LL-37 on single Bacillus subtilis cells, *Biochim Biophys Acta-Biomembr 1828*, 1511-1520.

(17) Rangarajan, N., Bakshi, S., and Weisshaar, J. C. (2013) Localized permeabilization of E. coli membranes by the antimicrobial peptide Cecropin A, *Biochem 52*, 6584-6594.

(18) Sochacki, K. A., Barns, K. J., Bucki, R., and Weisshaar, J. C. (2011) Real-time attack on single *Escherichia coli* cells by the human antimicrobial peptide LL-37, *PNAS U.S.A. 108*, E77-E81.

(19) Lee, M. W., Chakraborty, S., Schmidt, N. W., Murgai, R., Gellman, S. H., and Wong, G. C. L. (2014) Two interdependent mechanisms of antimicrobial activity allow for efficient killing in nylon-3-based polymeric mimics of innate immunity peptides, *Biochim Biophys Acta-Biomembr 1838*, 2269-2279.

(20) Sochacki, K. A., Shkel, I. A., Record, M. T., and Weisshaar, J. C. (2011) Protein Diffusion in the Periplasm of *E. coli* under Osmotic Stress, *Biophys J 100*, 22-31.

(21) Baba, T., Ara, T., Hasegawa, M., Takai, Y., Okumura, Y., Baba, M., Datsenko, K. A., Tomita, M., Wanner, B. L., and Mori, H. (2006) Construction of *Escherichia coli* K-12 in-frame, single-gene knockout mutants: the Keio collection, *Mol Sys Biol 2*, 2006:0008.

(22) Neidhardt, F. C., Bloch, P. L., and Smith, D. F. (1974) Culture medium for enterobacteria, *J Bacteriol 119*, 736-747.

(23) Choi, H., Chakraborty, S., Liu, R., Gellman, S. H., and Weisshaar, J. C. (2014) Medium Effects on Minimum Inhibitory Concentrations of Nylon-3 Polymers against *E. coli*, *PLoS One 9*, e104500.

(24) Pilizota, T., and Shaevitz, J. W. (2013) Plasmolysis and Cell Shape Depend on Solute Outer-Membrane Permeability during Hyperosmotic Shock in *E. coli*, *Biophys J 104*, 2733-2742.

(25) Rojas, E., Theriot, J. A., and Huang, K. (2014) The response of bacterial growth rate to osmotic shock, *PNAS U.S.A. 111*, 7807-7812.

(26) MacMillan, S. V., Alexander, D. A., Culham, D. E., Kunte, H. J., Marshall, E. V., Rochon, D., and Wood, J. M. (1999) The ion coupling and organic substrate specificities of osmoregulatory transporter ProP in *Escherichia coli*, *Biochim Biophys Acta-Biomembr 1420*, 30-44.

(27) Wilks, J. C., and Slonczewski, J. L. (2007) pH of the cytoplasm and periplasm of *Escherichia coli*: Rapid measurement by green fluorescent protein fluorimetry, *J Bacteriol 189*, 5601-5607.

(28) Trchounian, A., and Kobayashi, H. (1999) Kup is the major K+ uptake system in *Escherichia coli* upon hyper-osmotic stress at a low pH, *FEBS Lett 447*, 144-148.

(29) Rhoads, D. B., and Epstein, W. (1977) Energy coupling to net K^+ transport in *Escherichia coli* K-12, *J Biol Chem 252*, 1394-1401.

(30) Siebers, A., and Altendorf, K. (1989) Characterization of the phosphorylated intermediate of the K^+-translocating KDP-ATPase from *Escherichia coli*, *J Biol Chem 264*, 5831-5838.

(31) Buurman, E. T., Kim, K. T., and Epstein, W. (1995) Genetic evidence for two sequentially occupied K^+ binding sites in the KDP transport ATPase, *J Biol Chem 270*, 6678-6685.

(32) Chimerel, C., Field, C. M., Pinero-Fernandez, S., Keyser, U. F., and Summers, D. K. (2012) Indole prevents *Escherichia coli* cell division by modulating membrane potential, *Biochim Biophys Acta-Biomembr 1818*, 1590-1594.

(33) Weber, S. C., Spakowitz, A. J., and Theriot, J. A. (2012) Nonthermal ATP-dependent fluctuations contribute to the in vivo motion of chromosomal loci, *PNAS U.S.A. 109*, 7338-7343.

(34) Record, M. T., Courtenay, E. S., Cayley, D. S., and Guttman, H. J. (1998) Responses of *E. coli* to osmotic stress: Large changes in amounts of cytoplasmic solutes and water, *Trends Biochem Sci 23*, 143-148.

(35) Spector, J., Zakharov, S., Lill, Y., Sharma, O., Cramer, W. A., and Ritchie, K. (2010) Mobility of BtuB and OmpF in the *Escherichia coli* outer membrane: implications for dynamic formation of a translocon complex, *Biophys J 99*, 3880-3886.

(36) Housden, N. G., Hopper, J. T. S., Lukoyanova, N., Rodriguez-Larrea, D., Wojdyla, J. A., Klein, A., Kaminska, R., Bayley, H., Saibil, H. R., Robinson, C. V., and Kleanthous, C. (2013) Intrinsically Disordered Protein Threads Through the Bacterial Outer-Membrane Porin OmpF, *Science 340*, 1570-1574.

(37) Wood, J. M. (2015) Bacterial responses to osmotic challenges, *J Gen Physiol 145*, 381-388.

(38) Richey, B., Cayley, D. S., Mossing, M. C., Kolka, C., Anderson, C. F., Farrar, T. C., and Record, M. T. (1987) Variability of the Intracellular Ionic Environment of *Escherichia coli* -

Differences between In vitro and In vivo Effects of Ion Concentrations on Protein-DNA Interactions and Gene Expression, *J Biol Chem 262*, 7157-7164.

(39) Record, M. T., Jr., Anderson, C. F., Mills, P., Mossing, M., and Roe, J. H. (1985) Ions as regulators of protein-nucleic acid interactions in vitro and in vivo, *Adv Biophys 20*, 109-135.

(40) Oliver, P. M., Crooks, J. A., Leidl, M., Yoon, E. J., Saghatelian, A., and Weibel, D. B. (2014) Localization of Anionic Phospholipids in *Escherichia coli* Cells, *J Bacteriol 196*, 3386-3398.

(41) Hancock, R. E. W., and Sahl, H.-G. (2006) Antimicrobial and host-defense peptides as new anti-infective therapeutic strategies, *Nat Biotech 24*, 1551-1557.

Table 6.1. *E. coli* strains, doubling times, and MIC values for copolymer **MM_{63}:CHx_{37}.**

***E. coli* strain** [a]	**Doubling time at 30°C (min)** [b]	**MIC (μg/mL)** [c]
MG1655 (WT)	50	25 (+ O_2), >200 (– O_2)
WT-ppGFP	51	--
Δ*proP*	50	6.25 (+ O_2)
Δ*proP*-ppGFP	49.5	--

[a] See text for detailed description of strains.

[b] In bulk cultures grown in EZRDM.

[c] Minimum inhibitory concentration for 6-hr incubation period. (+ O_2) denotes growth in aerobic conditions; (– O_2) denotes growth in anaerobic conditions.

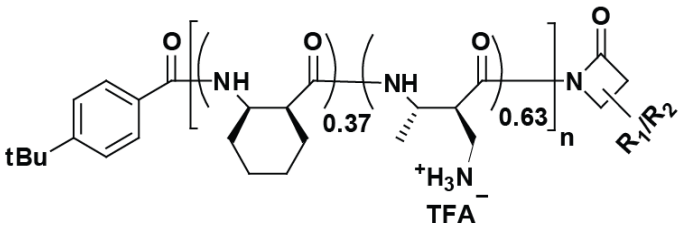

Figure 6.1. Structure of the nylon-3 copolymer **MM$_{63}$**:**CHx$_{37}$**, with the monomer molar ratio of 63:37 (cationic subunits : hydrophobic subunits). Mean chain length was 35 subunits.

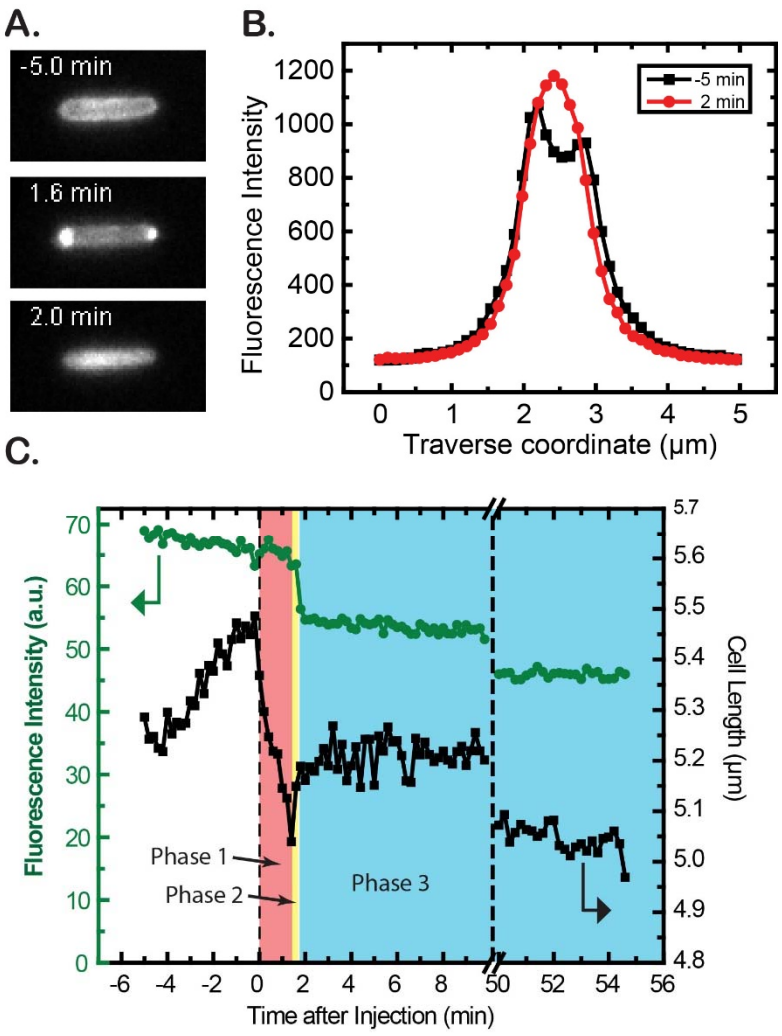

Figure 6.2 The strain WT-ppGFP was treated with 30 μg/mL of copolymer **MM_{63}:CHx_{37}** (1.2X the WT MIC) at time $t = 0$. A) GFP fluorescence images for a typical cell at $t = -5.0$ min, 1.6 min, and 2.0 min. B) The intensity profile projected onto the short axis of the cell at $t = -5.0$ min and +2.0 min. The periplasmic profile has become cytoplasmic. C) Cell length and total GFP fluorescence intensity vs time for the same cell shown in A. Length shrinks abruptly during the first 12-24 s after injection (Phase 1, salmon color); recovers partially at $t = 1.7$ min (Phase 2, yellow color); and then stabilizes after permeabilization of the cytoplasmic membrane at $t = 1.9$ min (Phase 3, blue color). See Movie S1.

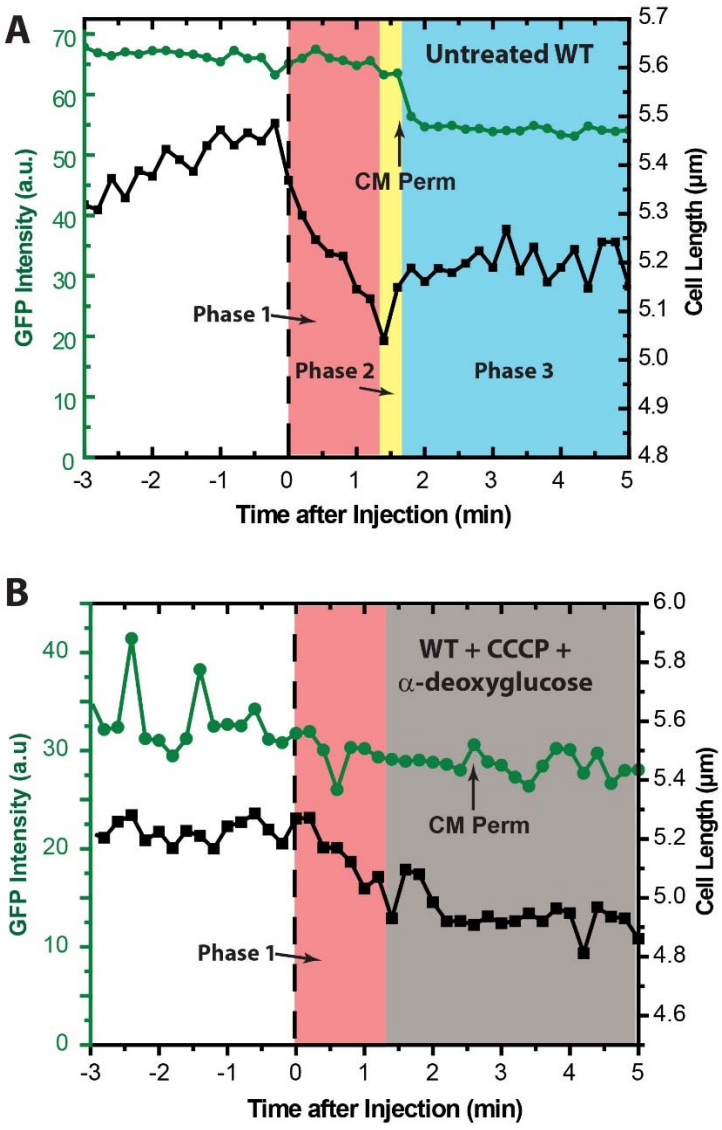

Figure 6.3 Relative cell length vs time under **MM_{63}:CHx_3** treatment at 30 µg/mL on WT MG1655 expressing periplasmic GFP without (left) and with (right) pretreated with CCCP (200 µM) and α-deoxyglucose (1 mM). The normally growing cells (right) exhibit Ph1 (Phase 1, red), Ph2 (Phase 2, yellow), and Ph3 (Phase 3, blue). The CCCP/ α-deoxyglucose treated cells exhibited Ph1, and Ph3'. The time at which cytoplasmic membrane (CM) permeabilization occurred is labeled with an arrow.

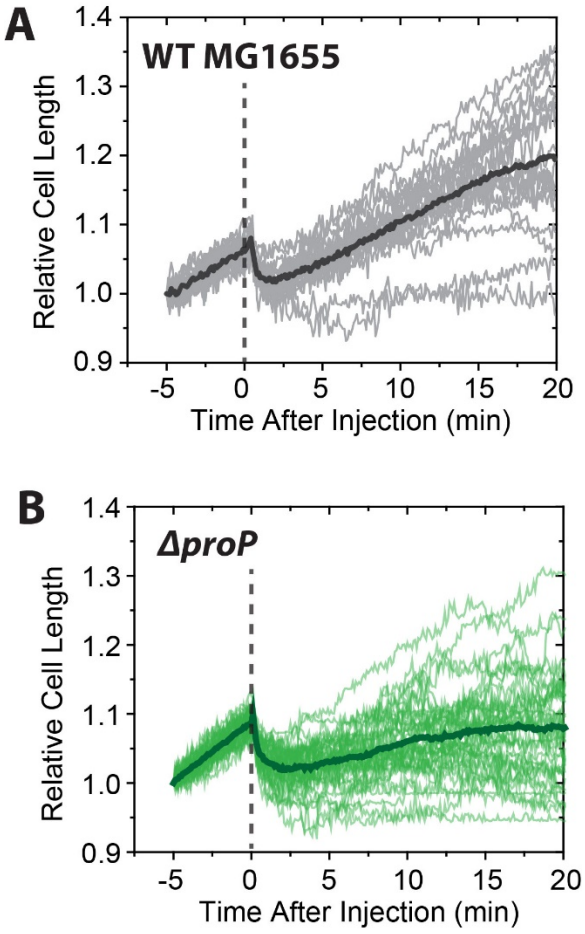

Figure 6.4 Relative cell length vs time under **MM_{63}:CHx_3** treatment at 15 µg/mL on WT MG1655 (gray, *n* = 20) and *ΔproP* (green, *n* = 41). The dotted line indicates the time of injection.

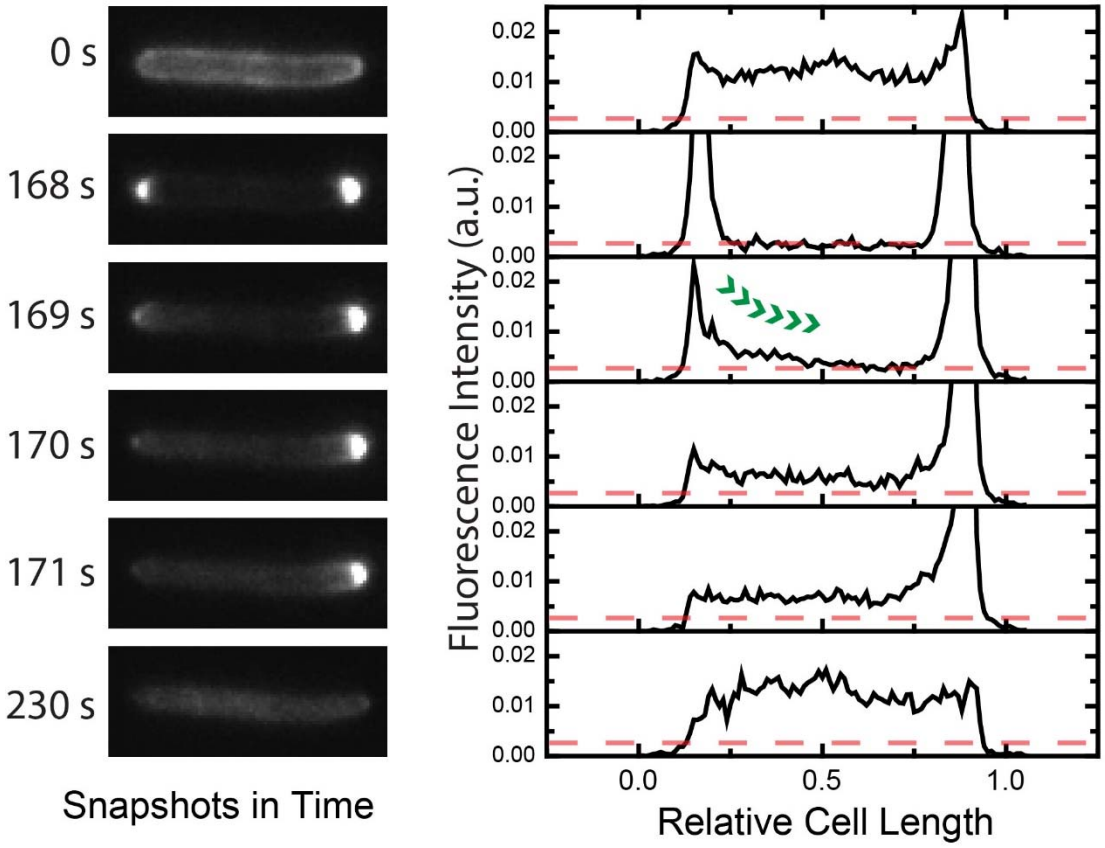

Figure 6.5 MG1655 expressing periplasmic GFP was treated with cephalexin at 60 μg/mL prior to the exposure to **MM_{63}:CHx_{37}.** The injection of the polymer solution occurred at 120 sec. The axial fluorescence intensity was normalized by the total fluorescence intensity. The red dotted line indicates the basal level of fluorescence in the cylindrical region of the cell when the plasmolysis occurred. See Movie S4.

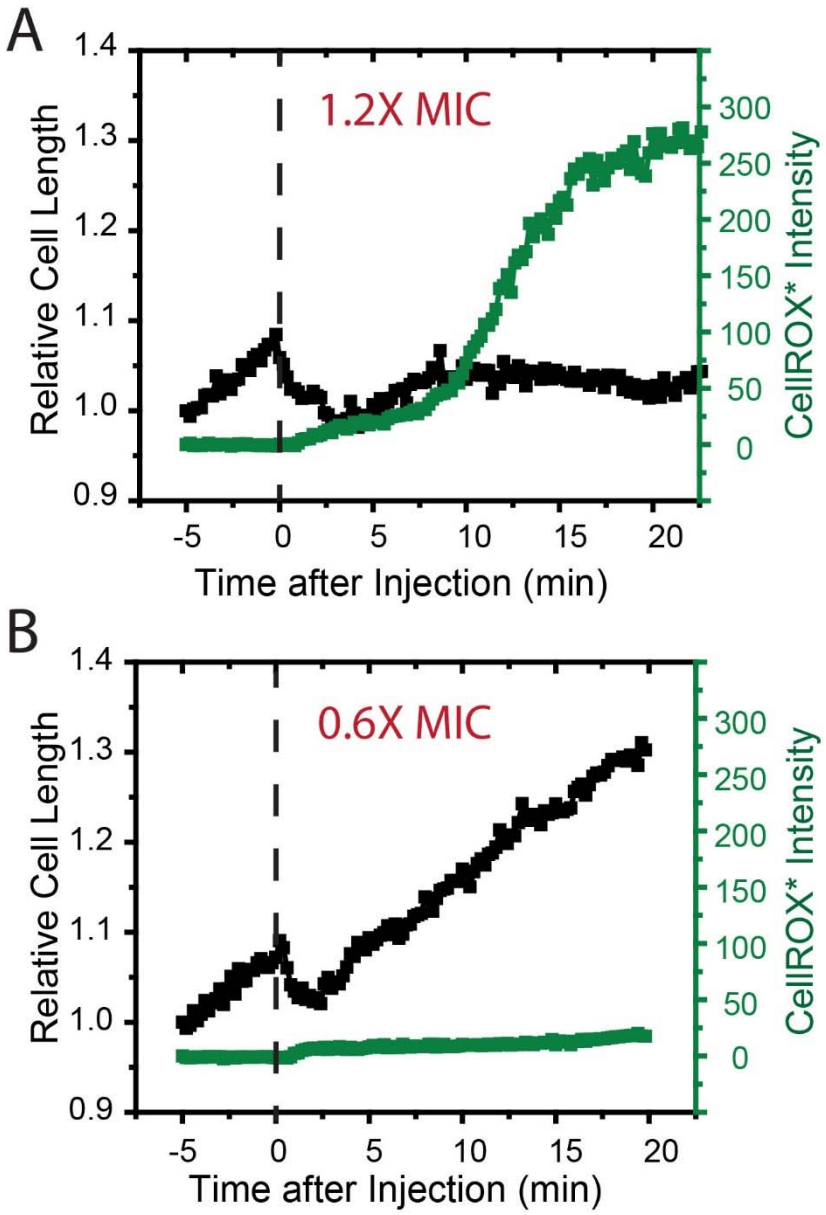

Figure 6.6 Typical single-cell measurements of CellROX* fluorescence intensity (green) and cell length (black) following addition of **MM_{63}:CHx_{37}** to WT-ppGFP cells at $t = 0$. (**A**) 1.2X MIC and (**B**) 0.6X MIC. In panel A, CM permeabilization likely occurs at $t \sim 7$ min, when length recovery ends. In panel B, CM permeabilization never occurs and cells recover growth. See Movie S5.

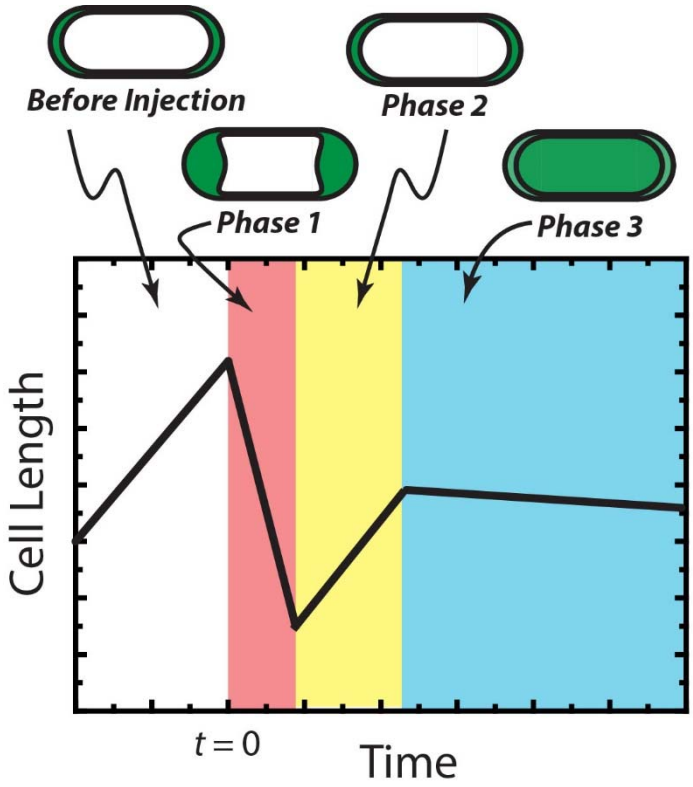

Figure 6.7 Schematic of the observed sequence of events after addition of **MM_{63}:CHx_{37}** to WT-ppGFP cells at 1.2X MIC. *Phase 1*: periplasmic "bubbles" and cell shrinkage; halting of cell growth. *Phase 2*: partial osmotic recovery. *Phase 3*: Permeabilization of cytoplasmic membrane. Duration of the three phases varies widely from cell to cell. See text for more details.

Appendix

Additional Details of Methods

Bacterial Strains, Growth Conditions, and Materials

Four *E. coli* strains were used (**Table 6.1**). The background strain of *E. coli* (wild type, denoted strain "WT") is MG1655 in all cases. The doubling time of MG1655 in EZRDM at 30°C was

50 min. For experiments on cells that export GFP to the periplasm (strain "WT-ppGFP"), TorA-GFP was expressed from the plasmid pJW1 as previously described.[1] The plasmid carries the gene for GFP with the twin-arginine-translocase (TAT) signal peptide appended to its N-terminus. TAT recognizes the signal peptide and exports the properly folded GFP to the periplasm, where it can freely diffuse. This strain had a doubling time of 51 min. To construct a deletion mutant strain lacking the osmoprotectant importer ProP (strain "Δ*proP*"), we obtained strain JW4072 from the KEIO collection.[2] We transduced the kanamycin resistance gene in JW4072 that is in place of *pro*P into our background strain MG1655 via P1 transduction. The doubling time of this strain was 50 min. To visualize the permeabilization of membranes in Δ*proP*, we transformed pJW1 into Δ*proP* and expressed periplasmic GFP using the same protocol (strain "Δ*proP*-ppGFP"). The doubling time of Δ*proP*-ppGFP was again 50 min.

Bulk cultures were grown in EZ rich, defined medium (EZRDM),[3] which contains a MOPS-buffered solution supplemented with metal ions (M2130; Teknova), glucose (2 mg/mL), amino acids and vitamins (M2104; Teknova), nitrogenous bases (M2103; Teknova), 1.32 mM K_2HPO_4, and 76 mM NaCl. Cultures were grown from glycerol frozen stock to stationary phase overnight at 30°C. Subcultures were grown to exponential phase (OD = 0.2–0.6 at 600 nm) before sampling for the microscopy experiments at 30°C, unless otherwise specified.

Minimum Inhibitory Concentration (MIC) assay

The MIC for **MM$_{63}$:CHx$_{37}$** against the strains WT and Δ*proP* was determined using a broth microdilution method as previously described.[4] Two-fold serial dilutions of **MM$_{63}$:CHx$_{37}$** in EZRDM were performed in separate rows of a polystyrene 96-well plate with each well containing an inoculum of the *E. coli* strain. The inoculum was a 1:20 dilution from a stationary culture grown at 30°C. The plate was incubated at 30°C for 6 hr for aerobic MIC measurements. The MIC values were taken as the lowest concentration for which no growth was discernible (<0.05 OD) after 6 hr. The aerobic MIC value against WT cells was 25 μg/mL. The molecular weight of an "average" copolymer (35 subunits long, 37% **CHx**, 63% **MM** sidechains) would be ~6.5 kDa. Thus an MIC of 25 μg/mL corresponds to a molar concentration of about 4 μM. We repeated the same MIC assay on the Δ*proP* strain and obtained the value 6.25 μg/mL, four times smaller than the MIC of the WT strain. In anaerobic conditions,[5] the MIC value for the WT strain was >200 μg/mL, at least 8 times higher than in aerobic conditions.

Microfluidics Chamber for Time-Lapse Measurement

Imaging of individual cells was carried out at 30°C in a simple microfluidics chamber consisting of a single rectilinear channel of uniform height of 50 μm and width of 6 mm, with a channel length of 11 mm.[5] The total chamber volume is ~10 μL. The negative of the cell design was patterned onto a silicon wafer via photolithography and the wafer was silanized. Sylgard 184 silicone elastomer mixture (Dow Corning) was poured onto the patterned silicon wafer and baked for 30 min in a 110°C oven after removing air in a vacuum desiccator. The cured polydimethylsiloxane (PDMS) slab was removed and holes were punched for entry and exit hypodermic needles. The patterned PDMS slab was fused to a dried, acetone-cleaned,

22-mm × 40-mm glass coverslip pre-cleaned by plasma oxidation. Soon after the bonding of the two pieces, 0.01% poly-*L*-lysine (molecular weight >150,000 Da) was injected into the chamber for 30 min and then rinsed thoroughly with Millipore water. For imaging experiments, the chamber was maintained at 30°C with a TC-344B dual automatic temperature controller through the CC-28 cable assembly attached to RH-2 heater blocks (Warner Instruments).

Microscopy

Single-cell imaging was performed on a Nikon Eclipse Ti inverted microscope with a 100X, 1.45 N.A. phase contrast objective (Nikon), using epi illumination. An optically pumped semiconductor laser (Coherent) at 488 nm was expanded to illuminate the field of view uniformly. The laser intensity at the sample was ~5 W/cm^2. Fluorescence images were obtained with an EMCCD camera, either Andor iXon 897 or Andor iXon 887. The pixel size corresponds to 160 ± 10 nm at the sample. GFP fluorescence was imaged using the emission filter ET525/50M (Chroma).

The sequence of membrane permeabilization events caused by the copolymer can be monitored by changes in the intensity and spatial distribution of periplasmic GFP over time.[5-7] For the microscopy experiments on WT-ppGFP cells, we used 30 μg/mL of **MM_{63}:CHx_{37}** (1.2X WT MIC). A value slightly larger than the MIC was used to account for possible errors in the MIC assay. WT-ppGFP cells were injected into the microfluidics chamber. The base of the chamber was coated with poly-L-lysine to immobilize the cells. The immobilized cells were then observed in continuously refreshed, aerated medium for 5 min to ensure that the cells are growing properly prior to the injection of **MM_{63}:CHx_{37}**. On excitation at 488 nm, the resulting image of the cells exhibits a halo of green fluorescence, indicating a predominantly periplasmic spatial distribution of GFP (**Figure 6.2A**).

The fluorescence images are interleaved with phase contrast images every 6 s (total imaging cycle time of 12 s). The phase contrast images are used to measure cell length vs time to a precision of ±50 nm. Cell length is affected both by genuine growth and by osmotic effects, as described below. The method of cell length measurement was described previously.[5]

To test for oxidative stress, we added copolymer plus the permeable, oxidation-sensitive dye CellROX Green.[5] Reduced CellROX (as added) is a membrane permeable profluorophore with weak fluorescence. *In vitro*, oxidation of CellROX by the powerful oxidants superoxide (O_2^-) or hydroxyl radical (•OH) in the presence of ds-DNA induces strong CellROX fluorescence (excited at 488 nm and detected at 525 ± 25 nm). The weaker oxidant H_2O_2 does not induce CellROX fluorescence. The affinity of CellROX for DNA prevents the dye from escaping after permeabilization of the bacterial membranes, enabling us to detect oxidative damage inside of single cells. Additional details are provided in our recent study of CM15.[5]

Cytoplasmic Membrane Permeabilization Localized to One Pole

In previous studies with the natural AMPs LL-37[6] and Cecropin A,[7] we observed localized CM permeabilization near the endcaps or the septation site of *E. coli*. We tested whether WT-ppGFP cells under copolymer treatment also exhibit localized CM permeabilization. To enable easy visualization of the diffusive motion of periplasmic GFP at a 10 Hz frame rate, we pre-treated the cells with 60 μg/mL of cephalexin for 30 min. Cephalexin prevents septation, causing the cells to filament without hampering their overall growth. The increased cell length allows accurate monitoring of the changes in GFP spatial distribution after the copolymer treatment.

We initiated flow of the copolymer at 30 μg/mL (1.2X WT-MIC) and observed changes in the GFP spatial distribution, imaging at 10 Hz (0.1 s per camera frame, see Movie S4). As for

untreated cells, GFP first accumulates at both poles (periplasmic bubbles). After a lag time of several minutes, GFP abruptly begins to enter the cytoplasm *at one endcap* (**Figure 6.3**). This is clearly shown by the GFP axial intensity profile vs time. For the typical cell shown, essentially complete drainage of GFP from the endcap near the permeabilization site occurred in ~2 s. Drainage of GFP from the second endcap occurred much more slowly, over ~60 s. Evidently the second endcap drains by diffusion of the GFP along the thin, annular length of the periplasm to the first endcap, the site of permeabilization of the CM. The data thus strongly suggest that the CM permeabilization by the copolymer is localized at one pole. Intriguingly, this also indicates that once permeabilization has occurred near one CM endcap, the other endcap remains intact during the complete redistribution of the GFP signal into the cytoplasm.

Active Respiration Required for Partial Length Recovery

At 30 μg/mL of **MM_{63}:CHx_{37}** (1.2X WT MIC), during Phase 2 the cells lengthen for a variable amount of time until CM permeabilization occurs. If this partial recovery of cell length is related to active osmoregulation, we reasoned that it should depend on respiration, which maintains the proton-motive force (pmf) and enables biosynthesis of ATP. This in turn allows the cell to import ions (K^+ and Glu^-) and osmoprotectants (Pro and glycine betaine, if present in the medium) into the cytoplasm against the chemical gradient.[8-11]

To test this hypothesis, we pre-treated WT-ppGFP cells with both carbonyl cyanide *m*-chlorophenyl hydrazone (CCCP) at 200 μM and α-deoxyglucose at 1 mM for 10 min prior to the onset of the flow of copolymer. CCCP dissipates the pmf by transporting protons from the periplasm to the cytoplasm.[12] The α-deoxyglucose is imported and blocks normal glycolysis, preventing production of ATP by glycolysis itself.[13] After pre-treatment but prior to injection of 30 μg/mL of **MM_{63}:CHx_{37}**, we observed no growth of the cells, consistent with the halting of

active respiration. Then we flowed the copolymer solution over the pretreated cells. Much like the respiring cells (**Figure 6.4A**), the non-respiring cells shrank in length by ~10% and formed periplasmic bubbles (**Figure 6.4B**). Evidently the initial shrinkage (Phase 1) does not require ATP or the pmf, although the shrinkage occurred more slowly in general. Unlike the respiring cells, for the non-respiring cells we observed no recovery of the cell length after the shrinkage; Phase 2 was absent. This is consistent with the osmotic hypothesis. Cell shrinkage does not require active respiration, but the partial recovery of cell length does.

For the non-respiring cells, CM permeabilization again occurred after a variable time lag for >85% of the cells, indicating that active respiration is not required for the CM permeabilization step. In addition, for the non-respiring cells the total GFP fluorescence intensity remained constant even after GFP had entered the cytoplasm (**Figure 6.4B**). This supports the suggestion that the sudden ~15% decrease in GFP intensity observed in respiring cells is due to equilibration of the pH of the cytoplasm with that of the periplasm.

Additional Supporting Figures

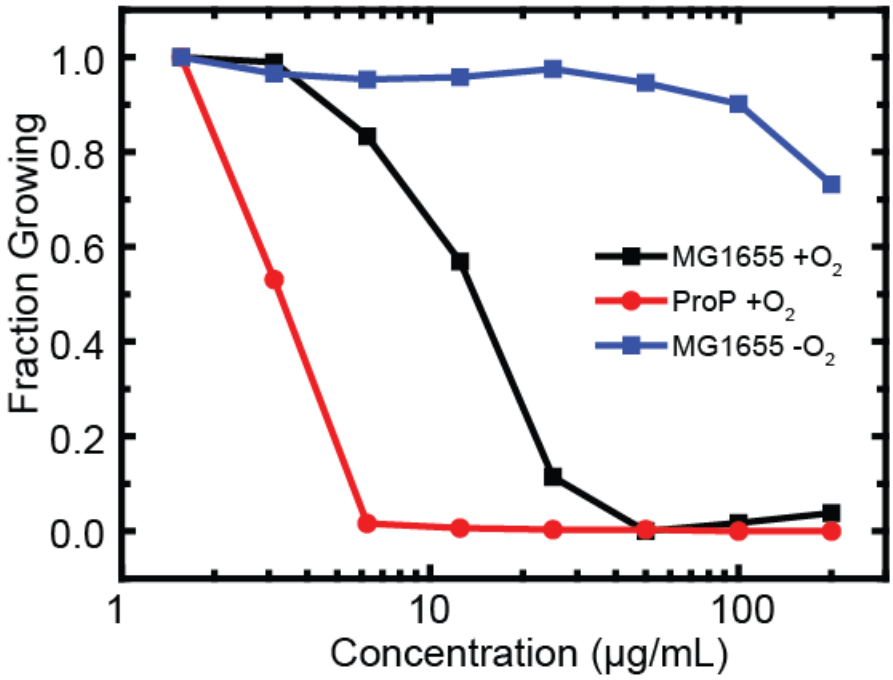

Appendix 6A. Bulk minimum inhibitory concentration (MIC) assay was performed for **MM_{63}:CHx_{37}** on "wild type" *E. coli* MG1655 in aerobic (black) and anaerobic (blue) conditions and on the Δ*proP* strain in aerobic condition (red) in EZRDM at 30ºC. Cell growth was measured by optical density (OD) at 595 nm in each well at the 6-hr time point. The data are plotted as *Fraction Growing* = (OD – minOD)/(maxOD – minOD) to enable direct comparison between strains.

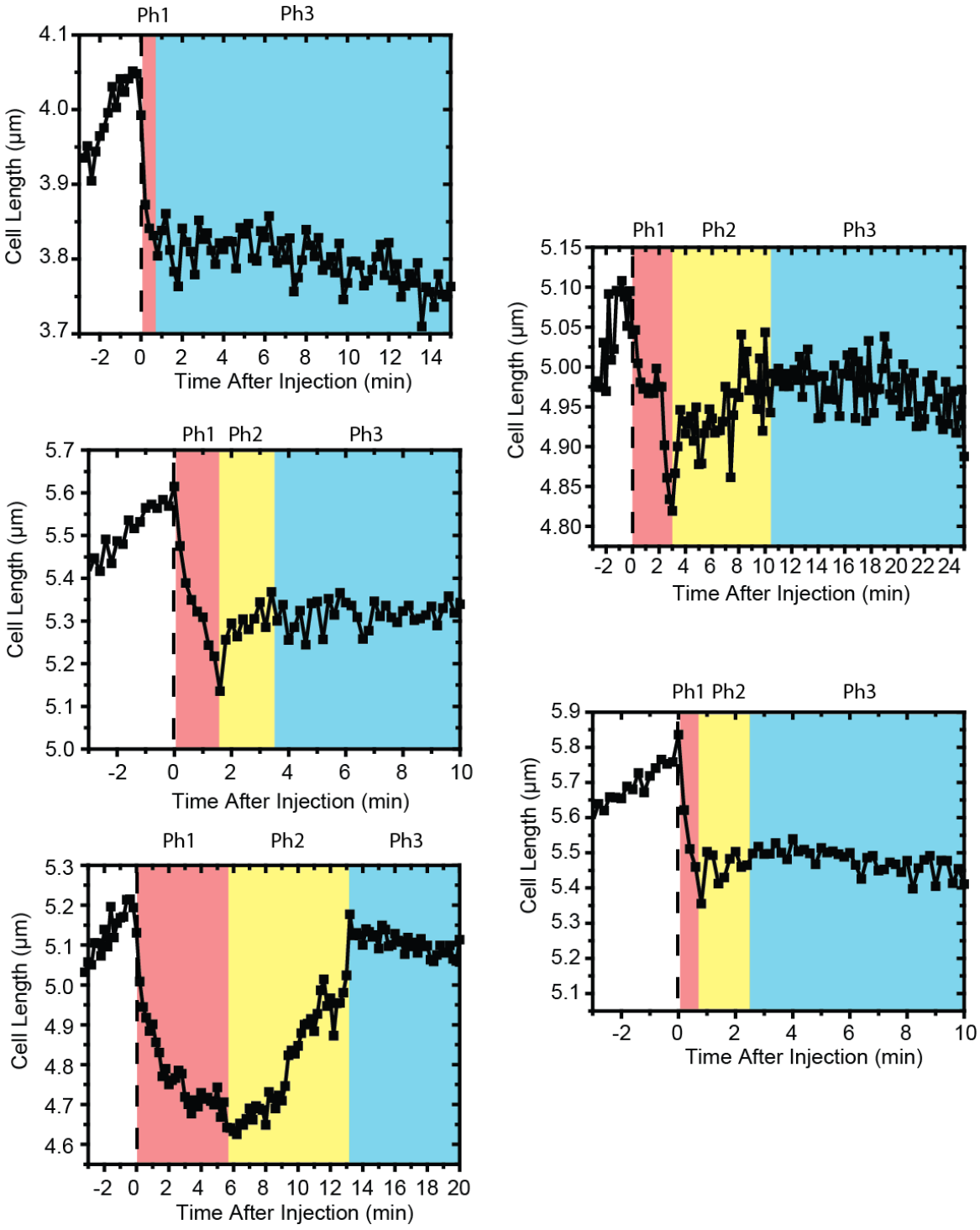

Appendix 6B. Additional examples of cell length vs time traces for five cells treated with 30 µg/mL of **MM_{63}:CHx_{37}** at $t = 0$. Shrinkage (Phase 1, red), length recovery (Phase 2, yellow), and CM permeabilization (Phase 3, blue) are marked.

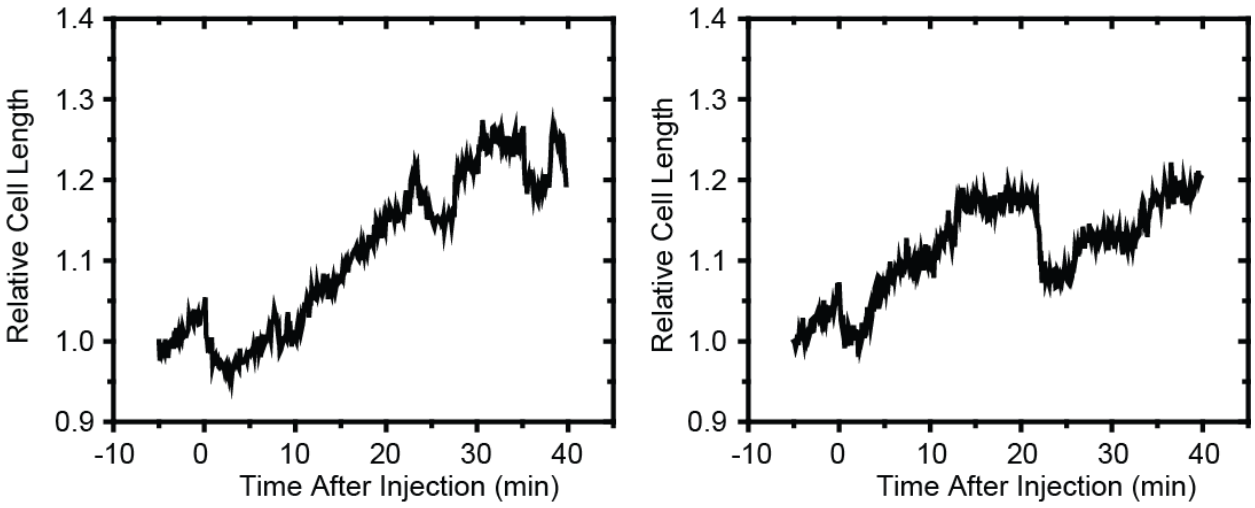

Appendix 6C. Examples of cells under 30 μg/mL of **MM_{63}:CHx_{37}** that exhibit multiple cycles of shrinkage and periplasmic bubble formation followed by partial recovery. See Movie S2 for an example.

References for Appendix

(1) Sochacki, K. A., Shkel, I. A., Record, M. T., and Weisshaar, J. C. (2011) Protein Diffusion in the Periplasm of E-coli under Osmotic Stress, *Biophys. J. 100*, 22-31.

(2) Baba, T., Ara, T., Hasegawa, M., Takai, Y., Okumura, Y., Baba, M., Datsenko, K. A., Tomita, M., Wanner, B. L., and Mori, H. (2006) Construction of *Escherichia coli* K-12 in-frame, single-gene knockout mutants: the Keio collection, *Molecular Systems Biology 2*, 2006:0008.

(3) Neidhardt, F. C., Bloch, P. L., and Smith, D. F. (1974) Culture medium for enterobacteria, *J Bacteriol 119*, 736-747.

(4) Choi, H., Chakraborty, S., Liu, R., Gellman, S. H., and Weisshaar, J. C. (2014) Medium Effects on Minimum Inhibitory Concentrations of Nylon-3 Polymers against *E. coli*, *PLoS One 9*.

(5) Choi, H., Yang, Z., and Weisshaar, J. C. (2015) Single-cell, real-time detection of oxidative stress induced in *Escherichia coli* by the antimicrobial peptide CM15, *PNAS USA 112*, E303-E310.

(6) Sochacki, K. A., Barns, K. J., Bucki, R., and Weisshaar, J. C. (2011) Real-time attack on single *Escherichia coli* cells by the human antimicrobial peptide LL-37, *PNAS USA108*, E77-E81.

(7) Rangarajan, N., Bakshi, S., and Weisshaar, J. C. (2013) Localized permeabilization of *E. coli* membranes by the antimicrobial peptide Cecropin A, *Biochemistry 52*, 6584-6594.

(8) Trchounian, A., and Kobayashi, H. (1999) Kup is the major K^+ uptake system in *Escherichia coli* upon hyper-osmotic stress at a low pH, *FEBS Lett. 447*, 144-148.

(9) Rhoads, D. B., and Epstein, W. (1977) Energy coupling to net K^+ transport in *Escherichia coli* K-12, *J Biol Chem 252*, 1394-1401.

(10) Siebers, A., and Altendorf, K. (1989) Characterization of the phosphorylated intermediate of the K^+-translocating KDP-ATPase from *Escherichia coli J Biol Chem 264*, 5831-5838.

(11) Buurman, E. T., Kim, K. T., and Epstein, W. (1995) Genetic evidence for two sequentially occupied K^+ binding sites in the KDP transport ATPase, *J Biol Chem 270*, 6678-6685.

(12) Chimerel, C., Field, C. M., Pinero-Fernandez, S., Keyser, U. F., and Summers, D. K. (2012) Indole prevents *Escherichia coli* cell division by modulating membrane potential, *Biochim. Biophys. Acta-Biomembr. 1818*, 1590-1594.

(13) Weber, S. C., Spakowitz, A. J., and Theriot, J. A. (2012) Nonthermal ATP-dependent fluctuations contribute to the *in vivo* motion of chromosomal loci, *PNAS USA 109*, 7338-7343.

Chapter 7

Future Aspects of Antimicrobial Peptides

My thesis serves as endeavor to observe multifaceted mechanisms of antimicrobial peptide (AMP) action on live *E. coli* cells in real time through quantitative fluorescence microscopy. We discovered that many antimicrobial peptides induces formation of reactive oxygen species (ROS) upon the accumulation in the periplasm. Development of fluorescent, real-time ROS assay allows visualization of such events at the single-cell level. This method was also applied to synthetic nylon-3 copolymers. Although the time-dependent generation of ROS was clearly observed through these assays, there are several important questions remaining to be answered.

How do AMPs induce formation of ROS?

Chapter 3, 4, and 6 showed that many antimicrobial peptides and even nylon-3 copolymers cause ROS formation. This event seems to correlate with the accumulation of highly cationic peptides in the periplasm, potentially interrupting proper function of certain integral membrane or membrane-associated proteins. However, we still do not know the molecular mechanisms by which AMPs induce ROS in aerobically growing *E. coli* cells.

We have initially investigated this by generating inverted membrane vesicles. These vesicles are generated by extruding *E. coli* cells through a French press. The high pressure inverts the inner membrane, allowing access to the cytoplasmic side of membrane proteins, such as NDH complexes.[1] Then, we can artificially drive the electron transport chain (ETC) by externally supplying NADH to these vesicles. We added CellROX green along with lambda DNA to probe for ROS generation, much as we did *in vivo*.[2]

The results in **Figure 7.1** clearly show that an active ETC is important for generation of ROS *in vitro.* When we blocked the ETC with rotenone (an NDH-1 complex inhibitor),[3] the inverted membrane vesicles exhibited less ROS formation upon CM15 addition in comparison to an unblocked ETC. This demonstrates that events upstream of the NADH oxidation site are

important for generation of ROS by CM15. Cyanide and azide addition to inverted membrane vesicles inhibits only cytochrome oxidase-*bo*$_3$ complex.[4] The results from cyanide and azide pretreatment showed diminished CellROX* intensity, suggesting that cytochrome oxidase-*bo*$_3$ complex is important for generation of ROS. The addition of superoxide dismutase (SOD) reduced the CellROX* signal. This further supports that the signal from CellROX* is due to superoxide.

Although these preliminary data support the hypothesis that the cytochrome *bo*3 complex is the major source of ROS in aerobically grown *E. coli* under CM15 treatment, the detailed mechanism by which peptides induce formation of ROS remained unanswered. Molecular simulation and fast dynamic studies on reconstituted *bo3* protein will give a better picture molecular mechanisms by which AMPs enhance ROS formation from this complex.

How do AMPs translocate the OM without permeabilization?

Here, I have demonstrated that CM15 and nylon-3 copolymer accumulate in the cytoplasm of *E. coli* and cause cytoplasmic membrane (CM) permeabilization. How does the CM permeabilization occur without OM permeabilization? There are currently two hypotheses.

One is translocation through the outer membrane by formation of transient pores. This model suggests that antimicrobial peptides cross lipid bilayers by transiently forming a pore (**Figure 7.2**). This pore is formed when several antimicrobial peptides arrange themselves perpendicular to the lipid bilayer surface. Because this structure may be unstable, the pore rapidly closes when the peptides reverts their arrangement to parallel to the bilayer surface. When this occurs, peptides can flip into the other leaflet, allowing translocation without permanent permeabilization (**Figure 7.2**). This is a likely model for how Melittin translocates the OM, as seen by the recovery of the outer membrane. This model has been suggested in *in vitro*

studies of unilamellar vesicles treated with buforin-2.[5] This could be investigated by the fluorocillin, which is a small beta-lactam with profluorogenic fluorescein. We could express the periplasmic beta-lactamage that cleaves the beta-lactam ring which in turn produces fluorescein that can be monitored through emission upon excitation of 488 nm. This could test for small transient pore formed prior to more permanent permeabilization.

Another hypothesis is that antimicrobial peptides translocate through outer membrane porins, such as OmpC or OmpF. These porins have been shown to allow passive translocation of hydrophilic molecules with molecular weight of ~600 Da through the channel. However, recent studies with colicin suggests that the OmpF can be used to transport large unfolded domains of proteins. A small portion of colicin (~3.5 kDa) can feed its way through the porin.[6] Hence, it is probable that short, unfolded antimicrobial peptides can feed through the porin channels in the same way.

In preliminary studies from our group, we observed cytoplasmic membrane permeabilization as an initial sequence of permeabilization from cells treated with antimicrobial peptides with shorter length. We are currently investigating this in collaboration with Gellman lab to study the effects of short, medium, and long artificial antimicrobial peptides on the sequence of membrane permeabilization on live *E. coli* cells. The peptides are synthesized by the addition of 50:50 mixture of lysine (K) and phenylalanine (F) through the conventional solid-phase synthesis method. This results in sequence random peptides with defined length. The peptides showed antimicrobial activities against *E. coli* cells. Our preliminary results with 15-mer and 30-mer at same molar concentration of showed that length plays a key role in determination of sequence of permeabilization. To further test whether it requires outer membrane porins, we could either overexpress or delete OmpF/OmpC and observe the behavior

of those cells under 15-mer and 30-mer through single-cell real-time microscopy using the periplasmic GFP and SYTOX orange.

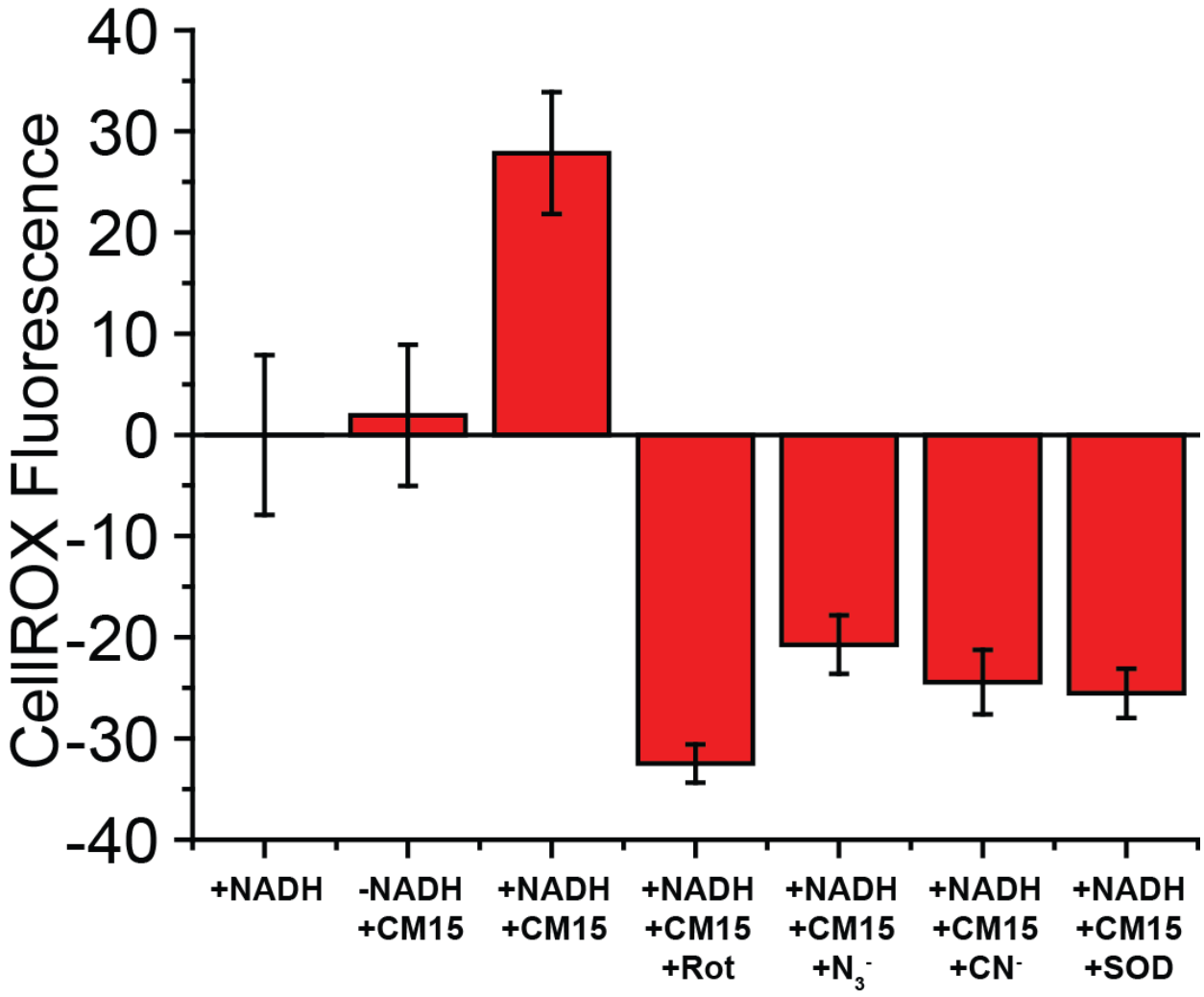

Figure 7.1 CellROX fluorescence *in vitro* on inverted membrane vesicles. 10 μg/mL of lambda DNA and 2.5 μM CellROX was added to all the solutions for all the conditions. We zeroed the signal based on the normal respiration of 200 μM NADH only. The concentration of CM15 was 10 μM. The concentration of roTransietntenone, N_3^-, and CN^- was 50 μM, 15 mM, and 3 mM, respectively. The metabolic inhibitors were added prior to addition of both NADH and CM15 to ensure the blockage of ETC prior to CM15 attack. The concentration of SOD was 1 unit. SOD was pre-incubated with the vesicles prior to CM15 addition.

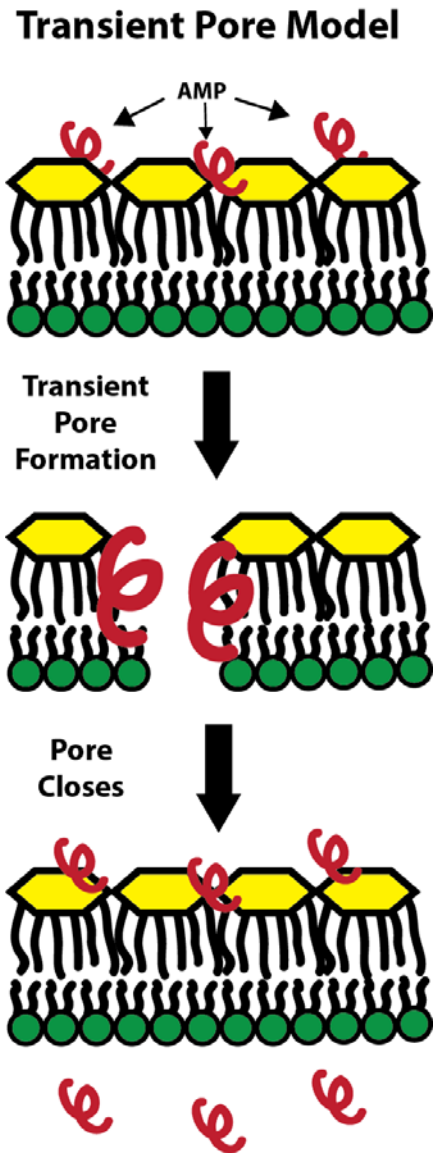

Figure 7.2. Transient pore model. Several antimicrobial peptides are inserted perpendicular to the bilayer surface, forming a passive pore. The pore closes when antimicrobial peptide return to sit laterally onto the bilayer surface, but presumably can go both side of the membrane. This allows the accumulation of antimicrobial peptides in the periplasm without permanent outer membrane permeabilization.

References

1. Seaver, L. C.; Imlay, J. A., Are respiratory enzymes the primary sources of intracellular hydrogen peroxide? *Journal of Biological Chemistry* **2004,** *279* (47), 48742-48750.

2. Choi, H.; Yang, Z.; Weisshaar, J. C., Single-cell, real-time detection of oxidative stress induced in Escherichia coli by the antimicrobial peptide CM15. *Proceedings of the National Academy of Sciences of the United States of America* **2015,** *112* (3), E303-E310.

3. Ueno, H.; Miyoshi, H.; Inoue, M.; Niidome, Y.; Iwamura, H., Structural factors of rotenone required for inhibition of various NADH-ubiquinone oxidoreductases. *Biochim Biophys Acta* **1996,** *1276* (3), 195-202.

4. Borisov, V. B.; MVerkhovsky, M. I., Oxygen as Acceptor. *EcoSalPlus* **2009**.

5. Kobayashi, S.; Chikushi, A.; Tougu, S.; Imura, Y.; Nishida, M.; Yano, Y.; Matsuzaki, K., Membrane translocation mechanism of the antimicrobial peptide buforin 2. *Biochemistry* **2004,** *43* (49), 15610-6.

6. Housden, N. G.; Hopper, J. T. S.; Lukoyanova, N.; Rodriguez-Larrea, D.; Wojdyla, J. A.; Klein, A.; Kaminska, R.; Bayley, H.; Saibil, H. R.; Robinson, C. V.; Kleanthous, C., Intrinsically Disordered Protein Threads Through the Bacterial Outer-Membrane Porin OmpF. *Science* **2013,** *340* (6140), 1570-1574.